

THE GLOBAL IMPACT OF SATELLITE-DERIVED
POLAR WINDS ON MODEL FORECASTS

by

David A. Santek

A dissertation submitted in partial fulfillment of
the requirements for the degree of

Doctor of Philosophy
(Atmospheric and Oceanic Sciences)

at the
University of Wisconsin-Madison

2007

Table of Contents

Table of Contents	i
Table of Figures.....	iii
Table of Tables.....	viii
Acknowledgements	x
Abstract	xi
1. Introduction	1
2. Satellite-derived winds algorithm.....	6
2.1 Geostationary satellite winds algorithm	6
2.2 Polar satellite winds algorithm	17
2.2.1 MODIS Data	19
2.2.2 Changes to winds algorithm	20
2.2.3 Polar orbit issues.....	22
2.2.4 Processing the MODIS passes.....	25
2.2.5 Parallax	26
2.2.6 Atmospheric considerations	29
2.2.7 Validation of MODIS polar winds	32
3. Use of polar winds in global models	36
3.1 Early experiments	36
3.2 Data assimilation issues	38
3.2.1 Filtering the MODIS winds	39
3.2.2 Measuring the impact on forecasts	40
3.3 Operational use of MODIS winds	47
4. Model experiments.....	48
4.1 MODIS winds assimilated in the GFS	49
4.2 Additional model experiments.....	50
4.3 MODIS winds dataset.....	51
Possible mechanisms that propagate polar AMV information into lower latitudes	54
4.4 Data Assimilation	54
4.4.1 Dynamic bias correction	54
4.4.2 Spectral assimilation	55

4.4.3	Gravity waves.....	56
4.5	Dynamics.....	56
4.5.1	Rossby wave	57
4.5.2	Ageostrophic wind	58
5.	Analysis	60
5.1	Analysis impact: Assimilation effects.....	61
5.2	Forecast impact: Wavelength	63
5.3	Analysis impact: Geographic.....	65
5.4	Analysis and forecast: Thickness difference	69
5.4.1	Case 1: 06 September 2004	72
5.4.2	Case 2: 07 September 2004	77
5.4.3	Case 3: 11 September 2004	81
5.4.4	Case 4: 12 September 2004	88
5.4.5	Case 5: 17 September 2004	90
5.4.6	MODIS winds impact on the NOGAPS analyses and forecasts	97
5.4.7	AMSU radiances impact on GFS analyses.....	98
5.5	Analysis and forecast: Ageostrophic wind	99
5.6	Forecast impact: Phase shift in waves.....	107
5.7	Forecast impact: Tropical cyclone positions.....	111
6.	Conclusions	113
7.	Future Work	115
8.	References	117
9.	Appendix A: Parallax Correction	123
10.	Appendix B: Polar Winds Impact Reported at IWW.....	128
11.	Appendix C: Derive Ageostrophic Wind Relation to Vorticity Advection.....	129
12.	Appendix D: Impact of MODIS winds in the NOGAPS	132
13.	Appendix E: Impact of AMSU Radiances in the GFS	138

Table of Figures

Figure 1: WMO rawinsondes in the polar regions. Arctic (top). Antarctic (bottom).	3
Figure 2: The relationship between the brightness temperature for the 6.7 μm and the 11 μm channels for varying cloud fraction. The top figure is for a surface temperature of 267 K. The bottom figure is for a surface temperature of 228 K with an inversion near the surface of 16° C, representing a polar atmosphere. (Courtesy of Jeff Key)	11
Figure 3: Coverage from three successive passes, 100 minutes apart, are depicted as red, green, and blue. The gray area is the region where the three passes overlap and winds are derived (shown as wind barbs).....	21
Figure 4: Satellite overpass frequency dependency on latitude. a) Top figure is for one satellite, Terra. b) Bottom figure for two satellites, Terra and Aqua.....	24
Figure 5: Off-nadir viewing of a cloud from a satellite.	27
Figure 6: Error in cloud position due to parallax, relative to the cloud height.....	28
Figure 7: Error in wind speed (m s^{-1}) due to parallax shift. The parallelogram approximates the overlap region in three orbits as seen in Figure 3.	29
Figure 8: Standard atmosphere profile showing the persistent low-level inversion in the Arctic region (courtesy of Jeff Key).....	31
Figure 9: Average Total Precipitable Water over Arctic region in June from NCEP (courtesy of Jeff Key).....	31
Figure 10: Anomaly correlation for 500 hPa geopotential, each experiment verified against its own analysis. Forecast scores are the correlation between the forecast geopotential height anomalies, with and without the MODIS winds, and their own analyses. (Courtesy of ECMWF)	42
Figure 11: Meridional cross-section from the equator to the pole (from Palmén and Newton, 1969).....	42
Figure 12: The ribbons depict trajectories originating in Siberia that arrive in the western US in about 48 hours, descending from about 8-9 km to the surface. The left panel shows the vertical descent; the right panel is a view from the top to show the horizontal displacement. These are extracted from forecast fields of u,v,w from the GFS model initialized at 17 September 2004 at 0000 GMT.....	43

Figure 13: 60-hour ACC for the northern hemisphere 500 hPa geopotential heights from the Deutscher Wetterdienst (DWD) global model. Time period is from 12 June to 9 July 2003 (from Cress 2004).	44
Figure 14: GFS 120-hour ACC for the northern hemisphere 500 hPa geopotential heights from 11 August to 22 September 2004.	45
Figure 15: Accumulated snowfall forecasts (mm water equivalent) over Alaska for 20 March 2001. Inclusion of MODIS winds in the analysis produced a more accurate forecast. Top is the snowfall from the 5-day Control forecast (no MODIS winds); middle is the snowfall from the 5-day forecast that included the MODIS winds in the analysis; bottom is the snowfall from a 12-hr forecast for verification (“truth”). (Courtesy of ECMWF)	46
Figure 16: MODIS wind coverage for the 0000 GMT assimilation cycle on 06 September 2004. There are about 21,300 winds at this time: +/- 3 hours from model run time, arriving by 6 hours after the synoptic time.	52
Figure 17: Wind speed difference between the model run with and without the MODIS winds at 800 hPa. This is 6 hours into the experiment. The yellow is close to zero difference; the brown to black is up to a +7 m/s difference; the green to blue is from -1 to -6 m/s difference. This is an analysis grid, not a forecast.	62
Figure 18: Wind speed difference between the model run with and without the MODIS winds at 800 hPa. This is 6 days into the experiment. Same color scheme as Figure 17. This is an analysis grid, not a forecast.	63
Figure 19: Difference in ACC between the MODIS winds and control model run at 500 hPa for the 120-hour forecast in the northern hemisphere for the entire experiment: 11 August to 22 September 2004. The colors represent ranges of wavenumbers: blue 1-3, cyan 4-9, yellow 10-20, red 1-20.	64
Figure 20: The difference in the analysis height field between the MODIS run and the control for 11 September 2004 for a latitude circle at 50°N. The blue line is the mean adjusted difference, in geopotential meters. The red line represents the signal from the three highest frequencies from the power spectrum (see Figure 21).	66
Figure 21: The power spectrum of the height field analysis difference in longitude space (from Figure 20). The frequency is relative to a 360 degree cycle. The highest amplitude frequencies are labeled in wavelength (255°, 170°, 127.5°) in the graph.	68

- Figure 22: Thickness difference, with and without MODIS winds for the GFS analysis on 06 September 2004 at 0000 GMT. The color range from blue to red denotes a range of -30 to +30 gpm difference. Near zero difference is in green. The 30 m s^{-1} wind speed, representing the jet stream, is in transparent white..... 74
- Figure 23: Thickness difference, with and without MODIS winds for the GFS 72-hour forecast from 06 September 2004 at 0000 GMT model run. Same color scheme as Figure 22... 75
- Figure 24: Thickness difference, with and without MODIS winds for the GFS 120-hour forecast from 06 September 2004 at 0000 GMT model run. Same color scheme as Figure 22... 76
- Figure 25: Thickness difference, with and without MODIS winds for the GFS analysis on 07 September 2004 at 0000 GMT model run. Same color scheme as Figure 22..... 79
- Figure 26: Thickness difference, with and without MODIS winds for the GFS 120-hour forecast from 07 September 2004 at 0000 GMT model run. Same color scheme as Figure 22... 80
- Figure 27: GFS analysis differences of the 1000-500 hPa field, with and without the MODIS winds for 11 September 2004. Same contours and color scheme as Figure 22..... 83
- Figure 28: 72-hour GFS forecast differences of the 1000-500 hPa field, with and without the MODIS winds. Valid 0000 GMT on 14 September 2004. Same contours and color scheme as Figure 22..... 84
- Figure 29: 120-hour GFS forecast differences of the 1000-500 hPa field, with and without the MODIS winds. Valid 0000 GMT on 16 September 2004. Same contours and color scheme as Figure 22..... 85
- Figure 30: Hurricane Ivan over the southeast US for the 96-hour forecast from 0000 GMT on 11 September 2004. Solid red contours are the 500 hPa heights with MODIS winds; dashed red are 1000 hPa heights. Solid blue are 500 hPa heights of the control; dashed blue are 1000 hPa heights. Actual position at the forecast time of hurricane Ivan is shown with the hurricane symbol..... 86
- Figure 31: Hurricane Ivan over the southeast US for the 120-hour forecast from 0000 GMT on 11 September 2004. Solid red contours are the 500 hPa heights with MODIS winds; dashed red are 1000 hPa heights. Solid blue are 500 hPa heights of the control; dashed blue are 1000 hPa heights. Actual position at the forecast time of hurricane Ivan is shown with the hurricane symbol..... 87
- Figure 32: Thickness difference, with and without MODIS winds for the GFS analysis on 12 September 2004 at 0000 GMT model run. Same color scheme as Figure 22..... 89

- Figure 33: Thickness difference, with and without MODIS winds for the GFS 120-hour forecast from the 12 September 2004 0000 GMT model run. Same color scheme as Figure 22. 89
- Figure 34: Thickness difference, with and without MODIS winds for the GFS analysis on 17 September 2004 at 0000 GMT model run. Same color scheme as Figure 22..... 92
- Figure 35: Thickness difference, with and without MODIS winds for the GFS 120-hour forecast from the 17 September 2004 0000 GMT model run. Same color scheme as Figure 22. 93
- Figure 36: Thickness difference, with and without MODIS winds for the GFS verifying analysis on 22 September 2004 at 0000 GMT. Same color scheme as Figure 22..... 93
- Figure 37: Hurricane Karl over the Atlantic Ocean in the 96-hour forecast from 0000 GMT 17 September 2004. Solid red contours are the 500 hPa heights with MODIS winds; dashed red are 1000 hPa heights. Solid blue are 500 hPa heights of the control; dashed blue are 1000 hPa heights. Actual position at the forecast time of hurricane Karl is shown with the hurricane symbol. 94
- Figure 38: Hurricane Karl over the Atlantic Ocean in the 96-hour forecast from 0000 GMT 17 September 2004. Solid red contours are the 500 hPa heights with MODIS winds; dashed red are 1000 hPa heights. Solid blue are 500 hPa heights of the control; dashed blue are 1000 hPa heights. Actual position at the forecast time of hurricane Karl is shown with the hurricane symbol. 95
- Figure 39: Normalized speed difference (red contours) with 500 hPa heights for the GFS 120-hour forecast from the 17 September 2004 0000 GMT control model run. Positive red contours: control winds are faster by a factor of 1.5, 2, and 3 (contours 0.33, 0.50, 0.67). Negative red contours: control winds are slower by a factor of 1.5, 2, and 3 (contours -0.50, -1, -2)..... 96
- Figure 40: Ageostrophic wind, blue vectors, for the analysis on 17 September 2004 at 0000 GMT over the North Pacific Ocean. Dashed red contours are speed of the ageostrophic wind. Solid black contours are 500 hPa heights of the MODIS run. 100
- Figure 41: Geostrophic wind field differences for the analysis on 11 September 2004 over the North Pacific Ocean. Wind vector differences are shown as blue arrows. Dashed red contours are speed in m s^{-1} . Solid black contours are 500 hPa heights of the MODIS run..... 102
- Figure 42: Ageostrophic wind field differences for the analysis on 11 September 2004 over the North Pacific Ocean. Wind vector differences are shown as blue arrows. Dashed red

contours are speed in m s^{-1} . Solid black contours are 500 hPa heights of the MODIS run.....	103
Figure 43: Difference in the divergence of the ageostrophic wind (10^{-5} s^{-1}) at 500 hPa between the MODIS winds and control model runs over the North Pacific Ocean. This is equivalent to the difference in vorticity advection (Eq. 13). The largest differences are circled. This is the analysis at 0000 GMT on 11 September 2004.	104
Figure 44: Difference in the divergence of the ageostrophic wind (10^{-5} s^{-1}) at 500 hPa between the MODIS winds and control model runs over the US and Canada. This is equivalent to the difference in the vorticity advection (Eq. 13). The largest differences are circled. This is the analysis at 0000 GMT on 11 September 2004.	105
Figure 45: The analysis (top) and 72-hour forecast (bottom) showing differences in the 1000-500 hPa thickness, along with the MODIS 500 hPa heights. Same color scheme as Figure 22. The ovals are from Figure 43 and Figure 44. Positions of ovals in the 72-hour forecast represent a subjective positioning using intermediate forecast times to guide.	106
Figure 46: Latitude slice at 50°N of 500 hPa heights for the 120 hour forecast from 17 September 2004 for the control (blue) and the MODIS winds (red).	108
Figure 47: Latitude slice at 35°N of 500 hPa heights for the 120 hour forecast from 17 September 2004 for the control (blue) and the MODIS winds (red).	109
Figure 48: Geometry used in parallax correction. The underlined variables are known quantities. The error due to parallax is $dist$, the arc length of angle a_2	125
Figure 49: NOGAPS analysis from 17 August 2005 1200 GMT. Same color scheme as Figure 22, although the jet streams are not depicted.	134
Figure 50: NOGAPS 120-hour forecast from 17 August 2005 1200 GMT. Same color scheme as Figure 22, although the jet streams are not depicted.	135
Figure 51: NOGAPS analysis from 19 August 2005 1200 GMT. Same color scheme as Figure 22, although the jet streams are not depicted.	136
Figure 52: NOGAPS 120-hour forecast from 19 August 2005 1200 GMT. Same color scheme as Figure 22, although the jet streams are not depicted.	137
Figure 53: 17 Aug 2003 at 0000 GMT analysis from GFS, AMSU assimilated. Same color scheme as Figure 22.	140
Figure 54: 23 Aug 2003 at 0000 GMT analysis from GFS, AMSU assimilated. Same color scheme as Figure 22.	141

Table of Tables

Table 1: Comparison (m s^{-1}) of Terra MODIS satellite winds, at all levels, to rawinsondes. Northern Hemisphere: 27,000 samples (90% WV) 5 March to 3 April 2001.....	33
Table 2: Comparison (m s^{-1}) of GOES-12 WV satellite winds to rawinsondes.....	34
Table 3: Comparison (m s^{-1}) of Terra MODIS WV satellite winds to rawinsondes.....	34
Table 4: Number of MODIS winds from Terra derived in the first experiment: 5 March to 3 April 2001.....	37
Table 5: Operational use of MODIS Polar Winds as of January 2007.....	47
Table 6: Five cases from September 2004. The ACC values are northern hemisphere, 120-hour forecast for all wave numbers.....	50
Table 7: Number of MODIS wind observations that are potentially available for the 0000 GMT cycle for the five case studies.....	53
Table 8: Large difference in analyses for a latitude cross-section of heights. X indicates a large difference with a subscript indicating the type of flow: T – trough, R – ridge, Z – zonal flow.....	66
Table 9: 06 September 2004 ACC values for the Northern Hemisphere, 120-hour forecast by wavenumber range.....	72
Table 10: 07 September 2004 ACC values for the Northern Hemisphere, 120-hour forecast by wavenumber range.....	77
Table 11: 11 September 2004 ACC values for the Northern Hemisphere, 120-hour forecast by wavenumber range.....	81
Table 12: 12 September 2004 ACC values for the Northern Hemisphere, 120-hour forecast by wavenumber range.....	88
Table 13: 17 September 2004 ACC values for the Northern Hemisphere, 120-hour forecast by wavenumber range.....	90
Table 14: Phase shift of 500 hPa heights at 50°N and 35°N for the 120-hour forecast for the five case studies. The shift is measured in degrees of longitude and is converted to kilometers in the table.	110
Table 15: Tropical cyclone track forecast errors in nautical miles for the 2004 hurricane season	111

Table 16: Frequency (in percent) of superior tropical cyclone track performance for the 2004 hurricane season.....	112
Table 17: Tropical cyclone track differences (nmi) between the control and the MODIS winds runs. Positive indicates that the MODIS winds improved the track forecast.	112
Table 18: Comparison between parallax corrected and uncorrected co-located vectors for a three-week period beginning on 23 July 2004. These are Terra-only over the Arctic...	126

Acknowledgements

I would like to thank the many people who helped make this work possible. To my advisor, Steve Ackerman, for taking me on after I was out of school for 20 years. To Paul Menzel for the opportunity to work on the MODIS polar winds project and his insightful ideas; Jeff Key for countless hours of discussion on polar issues. To the committee: Professors Jon Martin, Grant Petty, Michael Morgan, and Frank Scarpace for their suggestions and review of this thesis. Chris Velden for insight into the satellite-derived winds algorithm. Jim Jung and Tom Zapotocny for GFS datasets and discussions about the assimilation and model output. Randy Pauley, Pat Pauley, and Tim Hogan from NRL for discussions and NOGAPS data. Rick Kohrs for visualization ideas. Professor Emeritus Don Johnson for discussions on tropical to polar connections.

Thanks to the many Numerical Weather Prediction centers for their impact studies, comments, and suggestions over the years: Lars Peter Riishojgaard of the GMAO, Niels Bormann and Jean-Noël Thépaut of the ECMWF, Mary Forsythe of the Met Office (UK), and many others.

Also, I'd like to thank my parents and family who encouraged me through this entire process.

The research was supported, in part, by NOAA grant NA07EC0676 and NASA grant NAS531367.

Abstract

The use of Atmospheric Motion Vectors (AMVs) in Numerical Weather Prediction (NWP) models continues to be an important source of information in data sparse regions. These AMVs are derived from a time-sequence of images from geostationary and polar orbiting satellites. NWP centers have documented positive impact on model forecasts not only in regions where the AMVs are measured, but elsewhere as well. One example is the positive impact that the Moderate Resolution Imaging Spectroradiometer (MODIS) polar winds have on forecasts in the middle and subtropical latitudes, especially in 3 to 5 day forecasts and forecast bust situations. The MODIS winds are only derived poleward of 65° latitude. What are possible explanations for this global impact? This study investigates the hypothesis that the assimilation of polar winds modifies the flow in high latitudes near the polar jet stream and that this effect propagates to lower latitudes in extended forecasts.

Using a pre-operational version of the National Centers for Environmental Prediction's (NCEP) Global Forecast System (GFS), a side-by-side experiment was run for a six week period during the late summer of 2004, with and without the MODIS polar winds. Five forecast cases within this period were examined to determine how winds in the polar regions affect the wind and geopotential height fields in the jet stream region, resulting in changes in wave propagation speed.

From the five cases examined, it was determined that the addition of the polar winds modifies the mass balance in synoptic-scale waves near the polar jet streams, more consistently in data void regions. This change in mass balance is evident in differences in the ageostrophic wind, which has an effect on the speed and amplitude of baroclinic waves that extends from the jet stream into lower latitudes in later forecast times. These results reveal

the substantial impact that polar-only observations have on the predictability of global weather systems.

1. Introduction

While the polar regions comprise only one-eighth of the earth's total surface area, the importance of observations in those regions is becoming increasingly more evident. There are many examples on the influence of the polar regions on lower latitude atmospheric conditions on time scales from synoptic to climatic, space scales from meso to global, and extending through the depth of the troposphere. From a climate perspective, the polar regions are a barometer indicating changes through, for example, glacier extent and permafrost temperature (Hinzman et al. 2005). From a global circulation perspective, Gallimore and Johnson (1981) showed that a meridional Hadley-type circulation extends from the tropics to the poles by thermal forcing on isentropic surfaces. Furthermore, Coherent Tropopause Disturbances (CTDs), which are meso-scale vortices on the dynamic tropopause, have been observed moving from the arctic to near tropical latitudes (Pyle et al. 2004). However, Francis (2002) found that the existing upper-air observation network in high latitudes is insufficient for the accurate depiction of the tropospheric wind field.

The influence that the polar regions have on lower latitude circulation systems coupled with an inaccurate knowledge of the polar atmospheric state may result in an erroneous picture of global weather systems and subsequent forecasts. One way to improve on that knowledge is to use the proven remote-sensing technique of tracking clouds and other features from weather satellite images. Until recently, this has only been done routinely with geostationary satellites over the middle- and lower-latitudes. Extending this to high-latitudes using polar orbiting satellites presents new challenges. However, Key et al. (2003) showed that the addition of satellite-derived winds over the polar regions has a positive impact on global forecasts.

The use satellite-derived cloud displacements to infer atmospheric motion has been investigated since the first weather satellites were launched. In the early 1960s, Tetsuya Fujita developed analysis techniques to use cloud pictures from the first Television Infrared Observation Satellite (TIROS), a polar orbiter, for estimating the velocity of tropospheric winds (Menzel 2001). Throughout the 1970s and early 1980s, cloud motion winds were produced from geostationary satellite data using a combination of automated and manual techniques. Cloud-drift winds were used in numerical weather prediction systems as early as the 1980s. Although, it wasn't until 1992 that the National Oceanic and Atmospheric Administration (NOAA) began using an experimental automated winds software package developed at the University of Wisconsin-Madison Space Science and Engineering Center (SSEC) that made it possible to produce full-disk wind sets without manual intervention. Fully automated cloud-drift and water vapor motion vector production from the Geostationary Operational Environmental Satellites (GOES) became operational in 1996, with wind vectors being used routinely in the operational numerical models of the National Centers for Environmental Prediction (NCEP) (Nieman et al. 1997).

Satellite-derived wind fields are most valuable where few observations exist and model analyses are less accurate as a result. Like the oceans at lower latitudes, the polar regions suffer from a lack of observational data. Figure 1 illustrates the sparse observation network in the Arctic and Antarctic. World Meteorological Organization (WMO) stations, which provide regular winds observations from rawinsondes, are scattered across the coastal areas and the interior of Canada, Alaska, Russia, and northern Europe. There is little or no coverage of the interior of Greenland, the interior of Antarctica, the Arctic Ocean, and the oceans surrounding Antarctica.

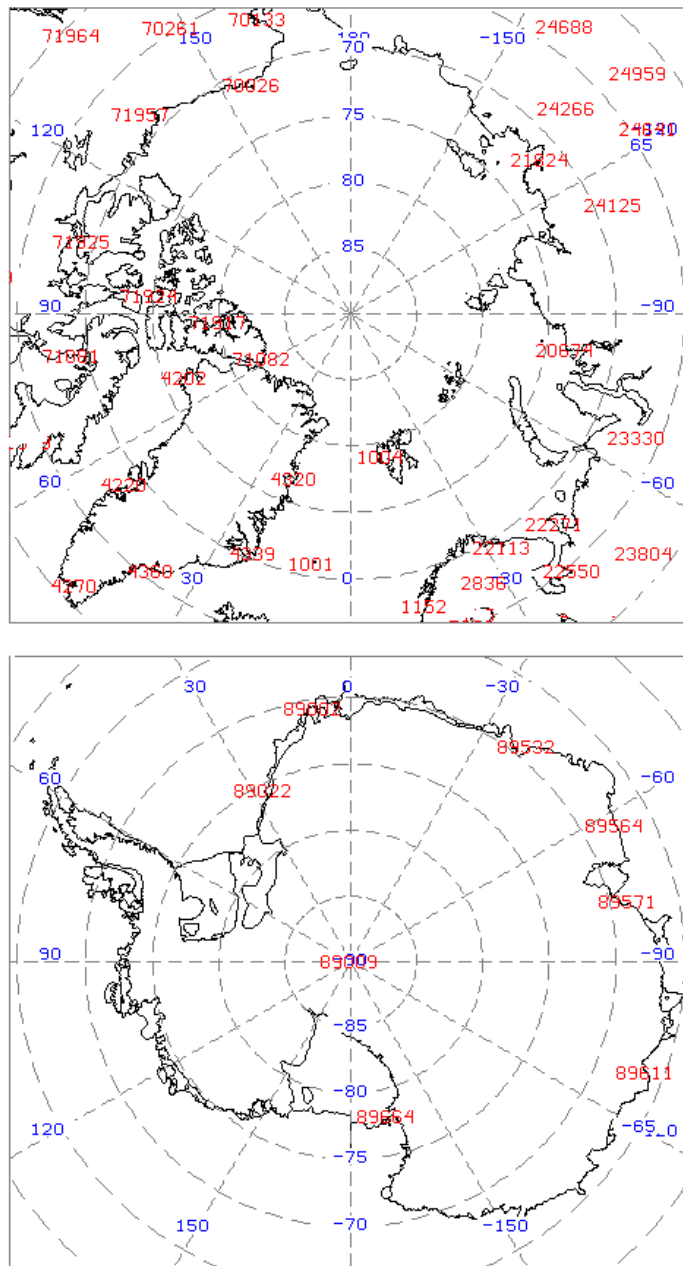


Figure 1: WMO rawinsondes in the polar regions. Arctic (top). Antarctic (bottom).

A study by Francis (2002) gives evidence that the existing observation network is not sufficient for an accurate depiction of high-latitude wind fields. The study examined tropospheric winds in the NCEP/National Center for Atmospheric Research (NCAR) Reanalysis and the European Centre for Medium Range Weather Forecasts (ECMWF)

Reanalysis datasets. Rawinsonde data from two Arctic field experiments, the Coordinated Eastern Arctic Experiment (CEAREX) in 1998 and the Lead Experiment (LeadEX) in 1992, that were not assimilated by the models were used as independent validation and compared to reanalysis products for five tropospheric vertical layers. It was found that both reanalyses exhibit large biases in zonal and meridional wind components, being too westerly and too northerly. It was also found that reanalysis winds were too strong by 25% to 65% relative to the rawinsonde values.

Satellite-derived winds from geostationary satellites have been used operationally in numerical models for more than a decade. Unfortunately, geostationary satellites are of little use at high latitudes due to poor viewing geometry, leading to large uncertainties in the derived wind vectors and the coverage falls well-short of the Arctic and Antarctic regions. Can polar-orbiting satellites be used to obtain wind information at high latitudes? The question has been explored since Fujita's initial experiments with some promising results. The Advanced Very High Resolution Radiometer (AVHRR) was used by Herman (1989, 1993) to estimate cloud-drift winds for a few Arctic scenes. Turner and Warren (1989) obtained useful cloud track wind information from AVHRR Global Area Coverage (GAC) data in the Weddell Sea, Antarctica. The manual intervention required in these case studies did not allow for routine production. It wasn't until the 1990s that software was available to automatically and routinely derive winds from a sequence of satellite images.

Near the turn of this century, the National Aeronautics and Space Administration (NASA) launched two research weather satellites (Terra and Aqua) which provide more spectral channels and higher global resolution than the AVHRR on the NOAA satellites. The infrared and water vapor channels on the Moderate Resolution Imaging Spectroradiometer (MODIS) satellite imagery were chosen to investigate the feasibility of tracking clouds and

clear-sky water vapor features over the polar regions. The first experiment of assimilating satellite-derived winds from MODIS proved successful, with a positive impact in forecasts being reported (Key et al. 2003). A somewhat startling result was that the positive impact was not restricted to the polar regions where the winds were measured, but it extended to lower latitudes.

The question was asked by members of the Numerical Weather Prediction (NWP) community: “Why do MODIS winds measured near the poles have a significant impact on global forecasts?” This study investigates the hypothesis that the assimilation of polar winds modifies the flow in high latitudes near the polar jet stream and that this effect propagates to lower latitudes in extended forecasts.

This hypothesis will be tested by investigating the impact that the MODIS winds have on model analyses and forecasts versus a control run for several cases, and how these differences can be explained in terms of data assimilation and atmospheric dynamics. First, the history of deriving winds from geostationary satellite images will be reviewed, the problems of applying this to the use of polar satellites and atmospheric issues in the polar regions will be examined, and the impact by several NWP centers will be presented.

2. Satellite-derived winds algorithm

The use of satellite-derived Atmospheric Motion Vectors (AMVs) in NWP models continues to be an important source of information in data sparse regions. For the past few decades, the AMVs have been primarily derived from a time-sequence of images from geostationary satellites. More recently, this algorithm has been applied to data from polar orbiting satellites and these AMVs are now routinely input into many operational global models. This section will examine the history of the geostationary satellite winds algorithm, the application to polar satellite data, and the validation of this technique.

2.1 Geostationary satellite winds algorithm

Geostationary remote sensing started in late 1966 with the first Applications Technology Satellite (ATS-1). The ATS-1 spin-scan cloud camera, developed by Professor Verner Suomi of the University of Wisconsin-Madison, produced full-disk images of the earth and its cloud cover every 20 minutes. Suomi noted that now “the clouds move—not the satellite.” Within the first month of the availability of ATS-1 imagery, Fujita and Bohan produced a movie showing views of mesoscale cloud patterns in motion. This illustrated for the first time the value of animated satellite imagery to infer atmospheric motion. Throughout the late 1960s, Fujita pioneered techniques to track cloud features on a variety of spatial scales and conducted experiments to validate these motions (Menzel 2001). In the early 1970s, SSEC refined the techniques of creating movie loops of satellite images and the production of satellite-derived winds with the development of the Man computer Data Access System (McIDAS) (Suomi et al. 1983).

A fundamental question arose: How representative are cloud motions to atmospheric motion? In the late 1960s, Fujita used ground-based cameras to validate and confirm that cloud motions indeed represented atmospheric motion (Menzel 2001). Hasler et al. (1977) reported on experiments conducted in the 1970s using aircraft to measure the wind at cloud levels. He found that oceanic trade cumulus clouds moved within 1.3 m s^{-1} of the ambient wind at the cloud base level. Cirrus clouds moved within 1.6 m s^{-1} of the mean wind in the cloud layer. These results substantiate Fujita's findings.

There are several techniques for determining the satellite-derived wind altitude. A comparison by Nieman et al. (1993) showed that different algorithms are better in specific cloud situations. In opaque clouds the infrared window works well. However, for semi-transparent or small clouds the infrared window tends to assign the height too low, due to radiance contributions from below the cloud level. The CO_2 technique does well in this situation because the semi-transparency can be accounted for by using the ratio of radiances from different spectral channels. Even though the MODIS instrument contains CO_2 channels, this technique has not been implemented at this time. For these cases the H_2O -intercept method is used, which is a good alternative method to the CO_2 technique (Nieman et al. 1993).

The current height assignment techniques assign a single level to the tracer. However, statistical comparisons of geostationary satellite-derived winds to radiosondes show that these satellite winds represent layers rather than specific levels (Rao et al. 2002). Clear-sky water-vapor winds represent the deepest layers compared to cloudy water-vapor winds or infrared-tracked clouds. Since there are so few deep clouds in the polar regions, upper-level wind information is mostly from tracking clear-sky water vapor features. Although there is much less moisture in the atmosphere in high latitudes, compared to middle- and

low-latitudes, the moisture is confined to a smaller vertical depth due to a lower tropopause. This may result in the clear-sky water-vapor polar winds representing a thinner layer than similarly-derived geostationary winds.

The following is an overview of the software used at the Cooperative Institute for Meteorological Satellite Studies (CIMSS) for deriving cloud motions from satellite images (Olander et al. 2000; Olander 2001).

The satellite winds derivation algorithm has been under development at CIMSS and NOAA/National Environmental Satellite, Data and Information Service (NESDIS) for more than 20 years. Initial efforts required human interaction to target and track cloud features in satellite imagery displayed with the McIDAS. These methods were very labor-intensive and extremely subjective, thus preventing the algorithm from being used operationally, although it proved useful for experiments, for example during the First GARP (Global Atmospheric Research Project) Global Experiment (FGGE) in 1979 (Lazzara et al. 1999).

Since the late 1980s, automated tracking (Merrill 1989; Merrill et al. 1991) and quality control techniques (Hayden and Pursor 1988; Holmlund, 1998) were developed and advanced to the level where significant impact within global forecast models has been achieved (Velden et al. 1992; Soden et al. 2001; Velden et al. 2005). Winds derived from this algorithm are now being utilized quantitatively in various forms within many global models worldwide. Wind data are currently produced operationally at NOAA/NESDIS and routinely at CIMSS for use in various global and regional scale models.

There are four major components to the winds algorithm (Olander 2001): target selection, target height assignment, wind tracking, and auto-editing (which includes quality control). This is a research software package that undergoes continual changes and

improvements. These components are presented in detail below, although it is restricted to only those features used with the polar-orbiting MODIS data.

The input data files are three time-ordered satellite images in a McIDAS-compatible format and forecast model output. Three images are used because consistency between vectors derived from each pair provides a measure of quality in the winds. The model output is used to determine target heights and a first guess for target tracking. The 6-, 9- or 12-hour forecasts are linearly interpolated to the middle-image time. From the middle image of the triplet, potential targets are determined by locating rectangular regions where the bi-directional gradient in brightness temperature exceeds a user-specified threshold, which is spectral band dependent. These regions are typically a cloud edge, a cloud feature, or water vapor gradients.

Once a target has been identified, four height assignment techniques are applied using single channels and combinations of channels. These different algorithms are known as the: Infrared Window Channel (IRW), Water Vapor Histogram (WVH), Cloud Base (CB), and H₂O-Intercept (H₂O) methods. All of these techniques depend on numerical model forecasts of temperature and moisture to convert satellite brightness temperatures into pressure heights.

The IRW and WVH methods use an average of the coldest pixels to determine the height from a vertical profile of temperature. This technique works well with opaque clouds, although opaque (or thick) clouds do not tend to move at the level of the assigned height. The movement of semi-transparent or small clouds gives a better representation of atmospheric motion, but the height assignment is compromised due to unknown cloud emissivity and cloud fraction.

The H₂O method is based on the relationship that radiances from two different spectral bands are linearly related for different cloud amounts within an area. The satellite-observed radiance results from a combination of clear-sky and cloudy radiances within a field of view. These two regimes result in a linear relationship between the two channels as shown in Figure 2. Using the model forecast to determine the vertical profile of temperature and moisture, a forward radiative model is used to compute theoretical top-of-atmosphere radiances, which is designated by the solid line in the figure. The linear relationship is extrapolated to the theoretical curve; the intersection results in the height of the cloud.

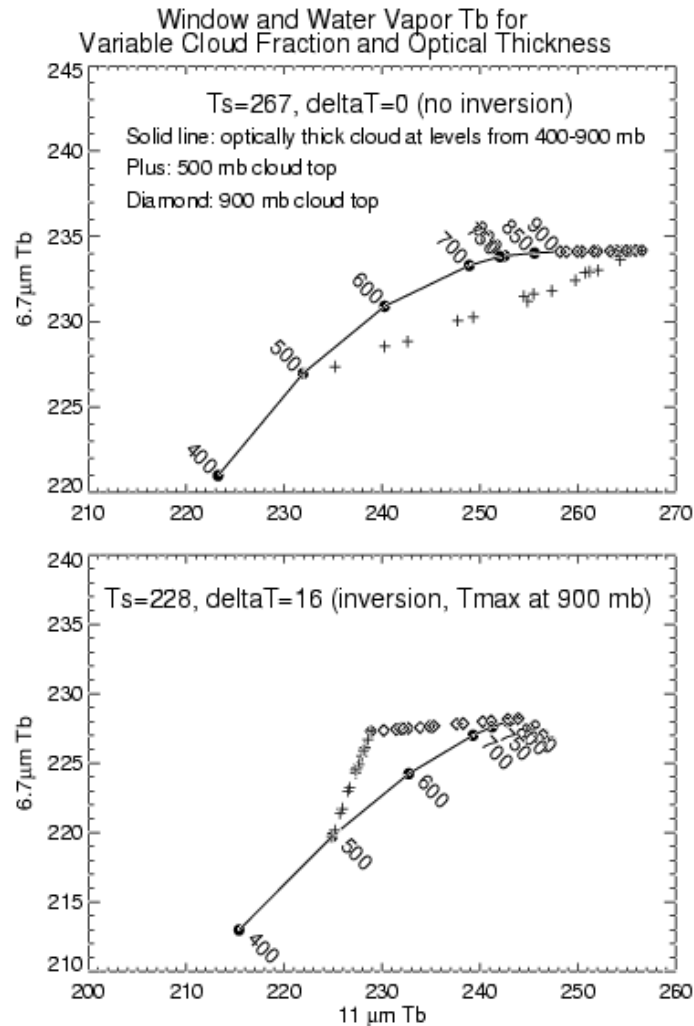


Figure 2: The relationship between the brightness temperature for the 6.7 μm and the 11 μm channels for varying cloud fraction. The top figure is for a surface temperature of 267 K. The bottom figure is for a surface temperature of 228 K with an inversion near the surface of 16° C, representing a polar atmosphere. (Courtesy of Jeff Key)

The CB method is applied to targets with an estimated height below 600 hPa that appear to be low-level cumulus. A histogram is computed to separate clear from cloudy pixels. Assuming the distributions are normal, the cloud base height can be estimated. The mid-cloud temperature, also called the modal cloud temperature, is determined by examining the second derivative histogram of the cloudy distribution, while the cloud top temperature is estimated to be located at the coldest 5% of the cloudy distribution. The cloud

base temperature is assumed to have the same difference from the modal cloud temperature as the cloud top temperature.

The initial target locations are investigated one-by-one to compute a displacement speed with the same feature at a time before and after the target image time. Prior to wind vector determination for each target, the "best" height assignment value is selected from the four potential height values. The height selection process is dependent upon the satellite channel. Infrared wind vector heights will be determined from one of three height values: IRW, H2O, or CB. Water vapor heights are chosen from either H2O or WVH methods. The lowest pressure (highest altitude) value of all of the calculated height values is used as the final wind vector height assignment value. If the final infrared height is based on the IRW method and a CB height is available, the CB height will be used for the vector height.

For each water vapor channel target, a cloud contamination value is determined to identify clear or cloud contaminated scenes. If there is an H2O height, it is subtracted from the WVH height; if not, the WVH height is subtracted from the IRW height. If the magnitude of this difference is greater than the threshold value of 75 hPa the scene is labeled as "clear". Otherwise, the scene is labeled as "cloud contaminated".

Once the best height and cloud contamination values are determined, the wind vector calculation for the targets begins. A first guess wind is interpolated from the model forecast at the location and height of the target. This guess is used to calculate a position in the first and third images of the sequence where the cloud feature should be. The image data within the target and larger search box regions are read. A cross correlation is computed between the target and subregions throughout the search box for the first pair of images. This is defined as (in one dimension)

$$CrossCorr = \frac{\sum_i [(t(i) - \bar{t}) * (s(i) - \bar{s})]}{\sqrt{\sum_i [t(i) - \bar{t}]^2} * \sqrt{\sum_i [s(i) - \bar{s}]^2}} \quad (1)$$

where t refers to target pixels, s refers to search box pixels, and overbars designate the means of the respective boxes. The highest correlated point, maximum *CrossCorr* value, between the target array within the search box is found and the vector displacement between these two points is calculated. This process is then repeated for the second image pair. Once the intermediate wind vectors are determined, acceleration checks are performed. The intermediate vectors are compared to each other. If the difference in the u- or v-component is greater than 10 m s^{-1} , this vector is flagged as bad. The intermediate vectors are then compared to an interpolated model forecast wind vector. Departures greater than 10 m s^{-1} from the guess u- and v-components are flagged for each wind vector, although these are still considered good wind vectors. Slow vectors, speed less than 3 m s^{-1} and below 300 hPa over land are flagged as bad; possibly indicating the tracking of a land feature.

There are two independent routines used for automatic quality control of the satellite-derived winds. The first quality control routine utilizes the statistical properties of a computed quality indicator for each wind vector through various consistency tests. The Quality Indicator (QI) (Holmlund 1998, Holmlund et al. 2001) for each AMV is calculated by estimating consistency in the intermediate wind vector pairs, spatial coherence, and the deviation from the operational forecast. The tests have the general form of:

$$C = \frac{|V_2(x, y) - V_1(x, y)|}{f * [V_2(x, y) + V_1(x, y)] + 1} \quad (2)$$

where C is the consistency measure, V is an input value for each parameter (e.g., direction, speed, and vector), and f is an empirically determined factor. The subscripts 1 and 2

represent the first or second wind vector of the pair. A hyperbolic tangent function is applied to the each consistency value to normalize them between zero and one. These values are then weight-summed (all tests have an equal weight except the spatial test has double the weight) and scaled by 100 to give a final range of zero to 100 for a single QI value. A QI greater than 65 usually indicates a good wind.

The QI has been beneficial in the application of high-density winds, by providing a consistent estimation of the comparative accuracy associated with each vector. The use of the QI for data selection and error estimation can be improved further by combining it with the Recursive Filter Flag (RFF) (Hayden and Purser 1995, Velden et al. 1997) computed in the auto-editor. This second quality measure is a two stage, three-dimensional objective analysis, based upon a recursive filter analysis, which utilizes weighted numerical model information as a background field. Wind vector heights are also reassigned in this process through a minimization of a variational penalty function.

This objective analysis is a successive approximation method but contains a unique feature of locally varying scaling, which gives it greater flexibility over data which is spatially non-homogeneous, such as satellite-derived winds. The general properties of the Recursive Filter (RF) can be broken out into six areas (Hayden and Purser 1995):

1. The recursive filter: The algorithm in one-dimension is:

$$A_i' = \alpha A_{i-1} + (1 - \alpha) A_i, \quad 0 < \alpha < 1 \quad (3)$$

applied to a line of values A_i , where i is the grid point index along a line. The A_i' values are forward smoothed, as i increases monotonically. The smoothing parameter $(1-\alpha)$ controls the filter width. This is extended to three dimensions for operating on the satellite winds.

2. Gridpoint adjustment: In each pass, the influence of the data is interpolated back to the grid points. This influence is weighted based on the quality (#4 below) and a predetermined reliability (user-input, if known).
3. Successive approximation and locally varying scaling: The recursive filter is a “successive approximation” technique where the spatial scale varies as multiple passes through the data are made. This results in retaining finer details in the analysis. Moreover, by using a locally varying scaling, the smoothing parameter varies from one grid point to another based on the quality and density of the surrounding data. This results in more smoothing in data void and low quality regions; less smoothing in high density and good quality regions.
4. Quality control: The quality is determined from the deviation of the data from the background field (see #5 below) and data consistency. Data consistency is implicit after first pass, since the influence of data is interpolated back to the background in each pass (#2 above). A pass-dependent tolerance is used to quality control the data. This tolerance is decreased on successive passes since the background fit should improve if the data are of good quality.
5. Initial background field: The initial background field is either a highly smoothed analysis of the data or a user-controlled fit of the data to a model forecast. Because the MODIS winds are not evenly distributed spatially, the latter is used with a relatively loose fit to the forecast.
6. Final quality flag: The quality flag represents a combination of the fit of the observation to the background and the quality of the neighboring analysis. This is assigned to each satellite wind and varies from 0 (poor) to 100 (good).

The wind vector heights are then optionally adjusted by minimizing a simple variational penalty function, in the vertical, by using the initial three-dimensional wind analyses and the model forecast (Velden et al. 1997):

$$B_{m,k} = \left(\frac{V_m - V_{i,j,k}}{F_v} \right)^2 + \left(\frac{T_m - T_{i,j,k}}{F_t} \right)^2 + \left(\frac{P_m - P_{i,j,k}}{F_p} \right)^2 + \left(\frac{dd_m - dd_{i,j,k}}{F_{dd}} \right)^2 + \left(\frac{s_m - s_{i,j,k}}{F_s} \right)^2 \quad (4)$$

where V = velocity, T = temperature, P = pressure, dd = direction, and s = speed. The subscript m refers to an individual wind measurement, i and j are horizontal locations in the analysis, and k is the vertical level. The denominators F_x are user-defined weights that may be varied to emphasize specific terms in the penalty function. For the MODIS winds, the following weights are used (determined from statistical analysis of geostationary winds):

$$F_v = 7 \text{ m s}^{-1}$$

$$F_t = 2^\circ \text{ C}$$

$$F_p = 1.5 \text{ hPa}$$

$$F_{dd} = \text{not used}$$

$$F_s = \text{not used}$$

The vertical search for a best fit is limited to ± 150 hPa from the initial assignment. The height reassignment may fail if no minimum is found or if the minimum exceeds empirically determined thresholds. In these cases the vector is rejected.

The second stage of the RF analysis uses as input the same vectors, but now with reassigned heights, and the first stage analysis as the background field. The quality flag is based on the fit of the observations to the analysis.

2.2 Polar satellite winds algorithm

Typically, the geostationary satellites have been used to derive AMVs because they provide the best temporal and spatial sampling for tracking features, but they are limited to regions equatorward of 60° latitude. There have been several attempts at using AVHRR data for tracking clouds over the polar regions, but they have been historically limited to case studies. The use of polar satellites is problematic not only because of the temporal sampling (100-minute orbits) and reduced overlap region from successive passes, but also this can only be done over high latitudes where atmospheric conditions are additionally problematic: warm clouds over a cold surface, persistent low-level inversions and isothermal layers that potentially impact cloud height assignment, and lower water vapor amounts.

Since polar orbiting weather satellites have been in use longer than geostationary satellites, one would surmise that cloud tracking has a longer history with polar data. This certainly is the case as it began in the early 1960s. But, its history is not as continuous as is the geostationary satellite-derived winds because the polar-orbiters do not provide adequate temporal or spatial coverage in middle- and low-latitudes. The narrow swaths are available only every 100 minutes, with little overlap for tracking cloud features except in the polar regions.

Ted Fujita was a pioneer in remote sensing of atmospheric motion. He developed methods to handle satellite images to make accurate inferences of winds possible with TIROS pictures in the early 1960s. He introduced the concept of 'movie loops', to view a time sequence of images, and the use of landmarks to align the images. When viewed in a time sequence, cloud images from these satellites showed the potential for inferring atmospheric motion. Fujita developed the necessary rectification and analysis techniques to make those

satellite pictures useful for estimating the velocity of both low- and high-level winds. Fujita also showed how satellite-viewed cloud shadows could be used to quantitatively determine cloud-top height (Menzel 2001).

The next major effort was more than 20 years later when Turner and Warren (1989) and Herman (1989) used AVHRR data to retrieve winds over the polar regions. Little validation of the technique was done since the process was manual and there were very few radiosonde observations to compare. When compared to rawinsonde winds, the AVHRR winds were found to have an RMS difference of 6 m s^{-1} . Herman and Nagle (1994) compared cloud-drift winds from AVHRR to gradient winds computed with the High-Resolution Infrared Sounder (HIRS). The AVHRR winds were found to be comparable to the HIRS gradient winds, with RMS differences less than 5 m s^{-1} . Herman and Nagle (1994) derived gradient winds from polar orbiting sounders, concluding that they compared favorably with rawinsondes and exhibited errors similar to other satellite-derived wind techniques. Zou and Van Woert (2002) found that thermal winds from satellite-derived temperature profiles and surface wind fields over mid-and high-latitude oceans had a bias. They thought the lack of ageostrophic dynamics may contribute to this bias, as the only ageostrophy is in the measured surface winds.

The current technique for deriving polar winds (Key et al. 2003; Velden et al. 2005) uses the same algorithm designed for geostationary satellite data with a time-sequence of MODIS satellite imagery over the polar regions. The use of MODIS data has distinct advantages over AVHRR: higher spatial resolution, additional spectral bands (including a water vapor channel), and more accurate geolocation.

2.2.1 MODIS Data

NASA has two weather research satellites: Terra and Aqua. These polar orbiting satellites carry the MODIS instrument which is a 36 channel imager consisting of visible/near infrared (VNIR) channels at 250 m and 500 m resolution and thermal infrared (IR) at 1 km resolution at nadir. The spectral range in the VNIR wavelengths is 0.4 to 2.1 μm and in the IR, 3.6 to 14.3 μm (Barnes et al. 1998). The instrument is designed for multi-disciplinary research, with sensors in spectral bands for atmosphere, ocean, and land interests. For example, atmospheric products determining clear-sky vs. cloudy conditions (Ackerman et al. 2002) and deriving atmospheric profiles (Menzel et al. 2002) are routinely calculated. It is also used to generate oceanic products, such as sea surface temperature (Brown and Minnett 1999), and the serendipitous detection of internal waves caused by a tsunami (Santek and Winguth 2007).

The data, in Level 1B format, is acquired in near real-time from a NASA/NOAA processing system at the Goddard Space Flight Center (GSFC). The Level 1B format provides geolocated and calibrated radiances in the original satellite perspective. The calibration procedure to convert sensor-output digital numbers to reflected radiance for the VNIR bands and thermally emitted radiance for the IR bands is described in Guenther et al. (1998). Additionally, a destriping algorithm is applied to the water vapor band to correct for detector differences in the ten-element linear detector array (Barnes et al. 1998). An inverse Planck function is used to convert IR emitted radiances to brightness temperatures (Petty 2004) in the winds generation code.

2.2.2 Changes to winds algorithm

The CIMSS winds algorithm has evolved for more than 30 years. The options, parameters, and default settings were tuned to the temporal and spatial characteristics of images from geostationary satellites. Previously, no attempt had been made to track cloud features from polar orbiting satellite data using this software, therefore adjustments and changes were necessary. Significant algorithm changes include:

1. the ability to use higher bit-depth in the raw data for tracking features. The original method used 8-bit values (a grayscale range of 0 to 255) which were based on the brightness temperature of the pixel: 1° C change in brightness temperature was a unit change in grayscale. This would smooth the details in the 10-bit MODIS data, especially in the water vapor channel, to the point where features could not be tracked in the dry Arctic atmosphere.
2. adding a parallax correction to account for changing viewing angles of features from different passes in the image triplet.
3. adding the polar stereographic projection transform. Previously, the code would track only in the original satellite projection. This is not applicable to the MODIS swaths since the tracking algorithm operates on rectangles of data assumed to be in the same geographic projection. Features in unremapped MODIS images would change in shape and orientation from pass-to-pass due to different viewing angles. Reprojecting to a polar stereographic view removes that variability.
4. disabling a zenith angle check that is used for GOES to prevent tracking features too close to the limb of the earth. This was disabled for MODIS because once the data are remapped to a polar stereographic projection, the zenith angle information for the pixels is lost. Also, this issue is not as significant for MODIS because few features are

tracked near the edge of the pass (high zenith angles) because the majority of the overlap is in the center of the pass (Figure 3).

5. correcting bugs found while tracking near-polar features. There were problems if features crossed very close to the poles and crossed over the dateline. The algorithm still will not target in the region poleward of 89° latitude, but this area is on the fringe of the MODIS passes and not likely to produce good quality winds (Figure 3).

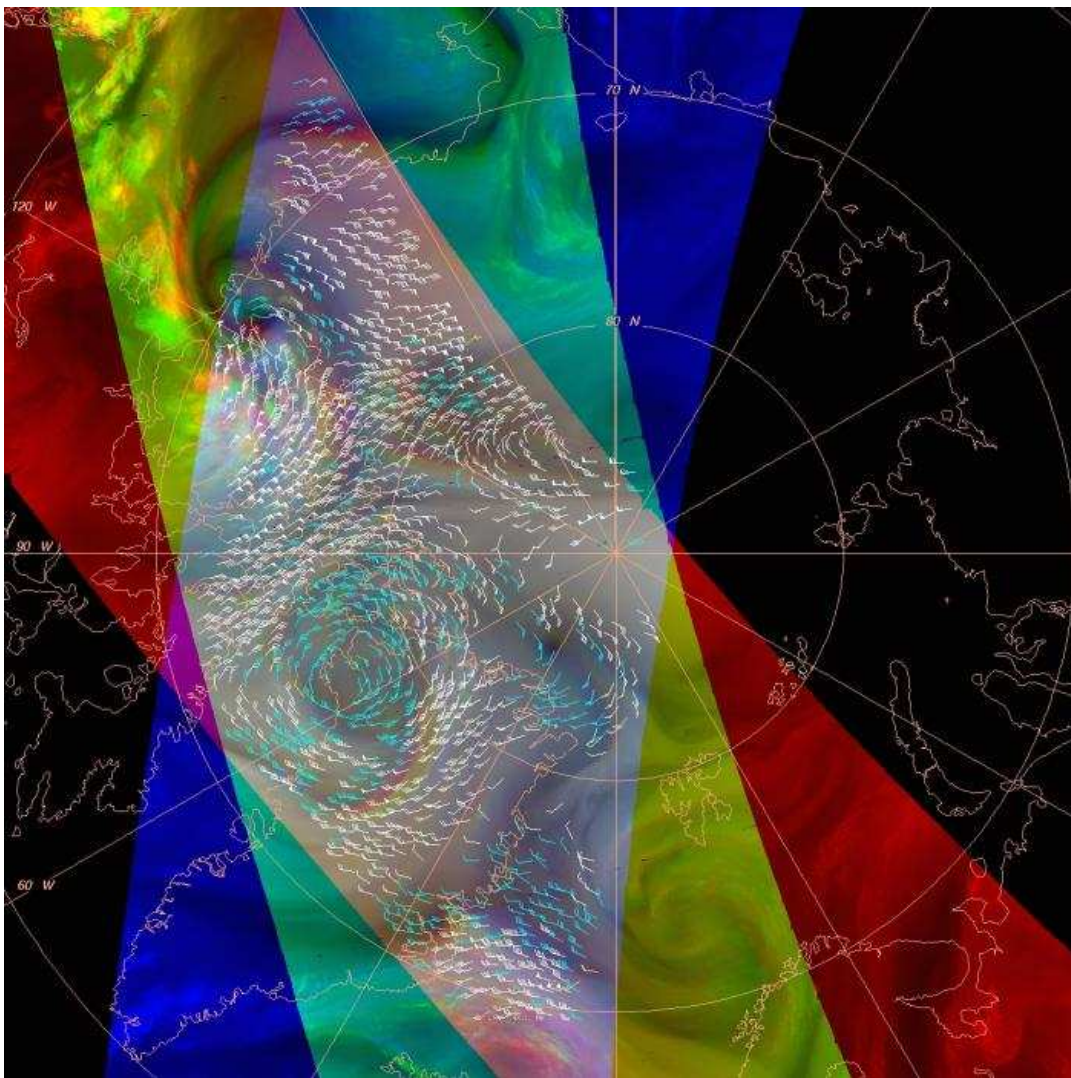


Figure 3: Coverage from three successive passes, 100 minutes apart, are depicted as red, green, and blue. The gray area is the region where the three passes overlap and winds are derived (shown as wind barbs).

There were also adjustments to existing user-configurable parameters:

1. the target box size and search box size were tuned for higher spatial and lower temporal resolution compared to GOES. This resulted in using a much larger search box as features move much further in 'image space' in 100 minutes at 2 km resolution compared to 15 minutes for GOES images at 4 km resolution. Also, the GOES search box is rectangular, longer in the east-west direction, to reduce computation time in the predominantly west to east flow in mid-latitudes. The search box is square for MODIS because even though the flow is primarily in a meridional direction, the tracking is in a 'circular' direction in a polar stereographic projection.
2. the use a different correlation routine for tracking features. It was found through testing that a cross correlation method for tracking features gave better spatial coverage than using the Euclidian norm correlation. The Euclidian norm has been used in GOES for many years and NESDIS uses this correlation technique for their production of the MODIS winds. NWP sites have noticed some difference in their statistics between the CIMSS- and NESDIS-produced MODIS winds because of the correlation difference, but the impact to the global forecasts is still very similar.

2.2.3 Polar orbit issues

The polar wind retrieval methodology builds on the cloud and water vapor feature tracking approach used with geostationary satellites. It is therefore necessary to track features over time in a sequence of images. Statistical analysis of visible, infrared, and water vapor wind datasets from geostationary satellites versus rawinsonde data have shown that the optimal processing intervals are 5 minutes for visible imagery at 1 km resolution, 10 minutes for infrared imagery at 4 km resolution, and 30 minutes for water vapor imagery at 8 km

resolution (Velden et al. 2000). For polar orbiting satellites, which circle the earth every 100 minutes, this temporal resolution is not possible with single satellite tracking.

Unlike the geostationary satellite which views an entire hemisphere at once, polar orbiting satellites view the polar regions with partially overlapping swaths taking an entire day to completely cover the area poleward of about 70° latitude. Figure 4a shows the frequency of time differences between successive overpasses at a given latitude-longitude point during one 24-hour period with a single satellite (Terra). The points show only those overpasses where the MODIS sensor would view the earth location at an angle of 50° or less. At larger scan angles the sensor would view the area near the pole on every overpass. At 60° latitude, there are two overpasses separated by about 10 hours and 13 hours. No useful wind information can be obtained at this latitude with only one satellite. At 80° latitude, there are many views separated by an orbital period of 100 minutes, but there is still a 13-hour gap each day. For other longitudes, the gap will occur earlier or later in the 24-hour period, so that the entire polar area will be covered by multiple overpasses over the course of a day. Although the 100-minute temporal sampling is significantly longer than the optimal processing intervals for geostationary satellites, in theory wind vectors can be obtained during part of every day for the area poleward of approximately 70° latitude.

Figure 4b shows the coverage with two satellites: Terra and Aqua. Temporal gaps of a few hours still exist at the lower latitudes of the polar regions, but at the higher latitudes the temporal coverage is very good. Given that geostationary satellites provide reliable wind information equatorward of about 60° latitude, near-global coverage can be obtained if polar-orbiting satellites are used for high-latitude coverage poleward of 70°. Note that there still remains a gap from about 60° to 70° latitude.

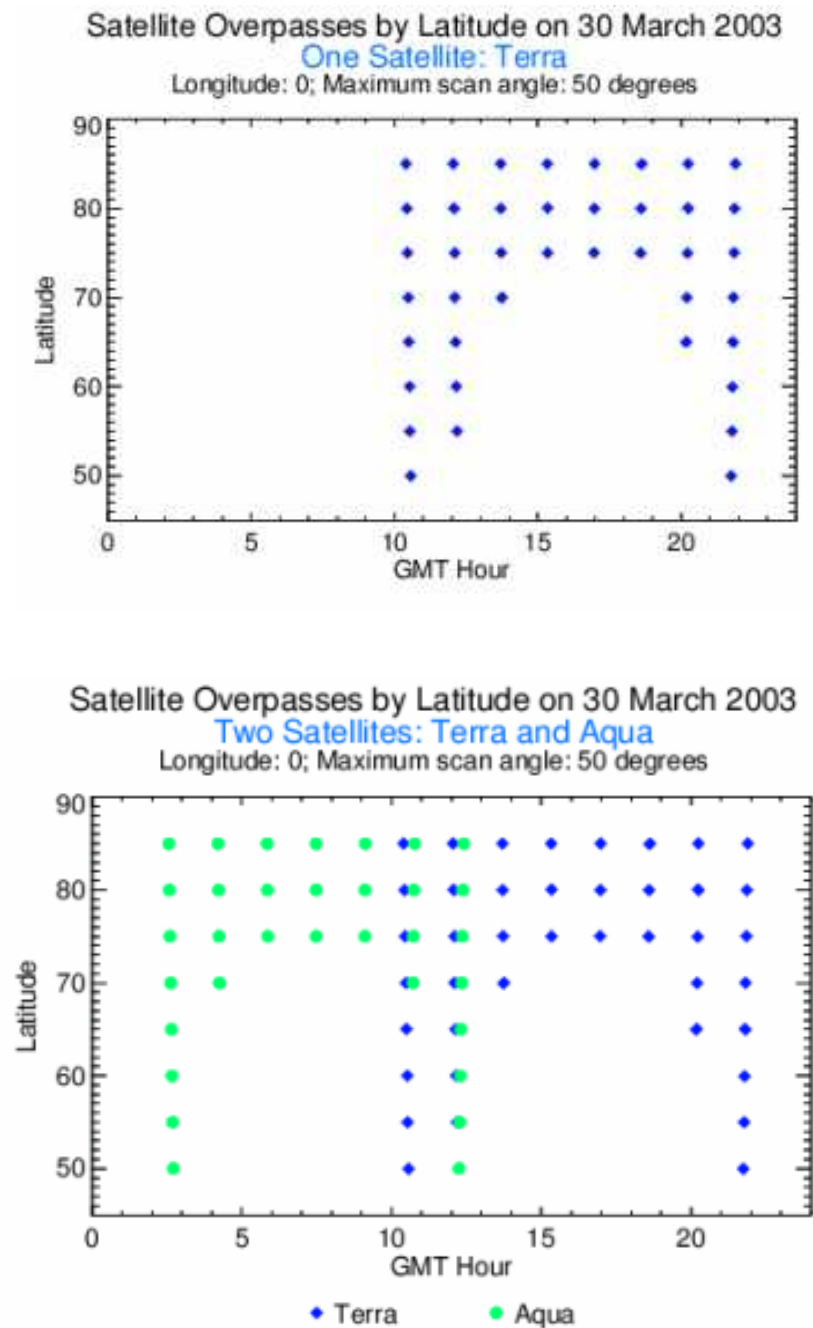


Figure 4: Satellite overpass frequency dependency on latitude. a) Top figure is for one satellite, Terra. b) Bottom figure for two satellites, Terra and Aqua.

The methodology employed for wind vector estimation requires three successive images for winds retrievals. Using a triplet, rather than a single pair of images, provides two

vectors for each target. This aids in the quality control by requiring a level of consistency in the vector pairs. However, this reduces the coverage of the polar winds by requiring the overlap of three consecutive passes (Figure 3). With geostationary satellites, the spatial coverage is constant. With a polar-orbiting satellite, the coverage from each successive orbit changes, so wind retrievals can only be done for the area of overlap between successive orbits. This is illustrated in Figure 3. Three successive passes over the Arctic are colored red, green, and blue; the overlap area is shades of gray. For each 200-minute time period (three successive orbits each separated by 100 minutes), wind vectors can be obtained in this overlap region.

2.2.4 Processing the MODIS passes

The MODIS Level 1B files are acquired in near real-time from the GSFC. The delay from real-time is generally from two to four hours. The files, a granule, contain 5 minutes of swath data; it takes two to four granules to cover our region of interest in the polar region. The original swath data, as scanned by the MODIS instrument, is 1 km resolution at nadir for the infrared channels. The data are remapped to a polar stereographic projection at 2 km resolution (true at 60° latitude). The lower resolution is chosen because: a) reprojecting at a higher resolution will result in pixel replication away from nadir; b) there is not an advantage of a high spatial resolution when the temporal resolution is 100 minutes (Jedlovec and Atkinson 1998). Images are then composited to form a single pass over the pole. The resulting images are 2800x2800 pixels, which covers the region poleward of 70° latitude (Figure 3).

Cloud and water vapor tracking with MODIS data is based on the established procedure used for GOES (section 2.1 *Geostationary satellite winds algorithm*). The following settings are used with the MODIS data:

- Cloud features are tracked in the infrared (IR) window band at 11 μm
- Water vapor (WV) features are tracked in the 6.7 μm band
- Targeting is performed using 13x13 pixel (26x26 km) boxes
- The gradient threshold for a valid target is 7° C for the IR, 1° C for the WV
- The cross correlation method is used to locate targets in the search box
- The search box is 50x50 pixels (100x100 km)

2.2.5 Parallax

An issue usually ignored when tracking features in geostationary images is parallax: the apparent displacement of a feature above ground that results from non-nadir viewing angles. Parallax is not as important in geostationary data because the change in parallax between images is usually insignificant as the features move very little with respect to the scanning geometry of the sensor. This is unlike images from polar orbiting satellites where the view may change substantially, orbit-to-orbit.

A cloud that is viewed off-nadir will appear to be further from the nadir position than it actually is (Figure 5).

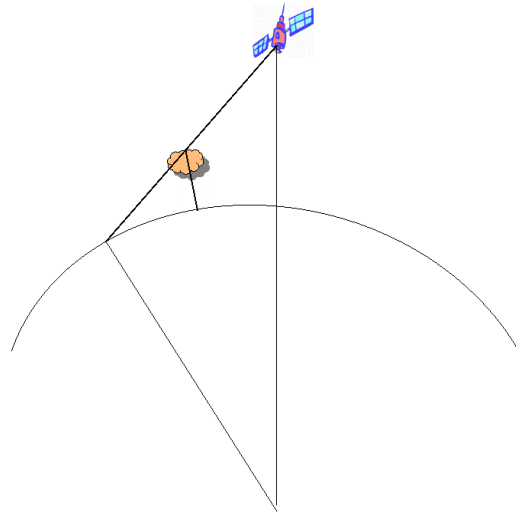


Figure 5: Off-nadir viewing of a cloud from a satellite.

The greater the viewing angle, the greater the displacement. For example, at 700 km from nadir the apparent location of a cloud with a height of 5 km will be approximately 5 km further from nadir than its actual position (Figure 6). At a 1000 km from nadir the displacement is 7 km. The displacement is not the same for a feature from one orbit to the next, as the viewing geometry and the actual cloud position change. Figure 7 illustrates that in this idealized overlap region, the speed error due to parallax for a 5 km cloud is generally less than 1.5 m s^{-1} . This theoretical error is confirmed in statistics from a three-week period that resulted in a mean speed error of less than 1 m s^{-1} . Also, it's important to note that the MODIS geolocation values have been adjusted for terrain elevation, which means the error due to parallax is inherently less over high terrain. See *Appendix A: Parallax Correction* for details on how the parallax is determined and applied to the wind vectors.

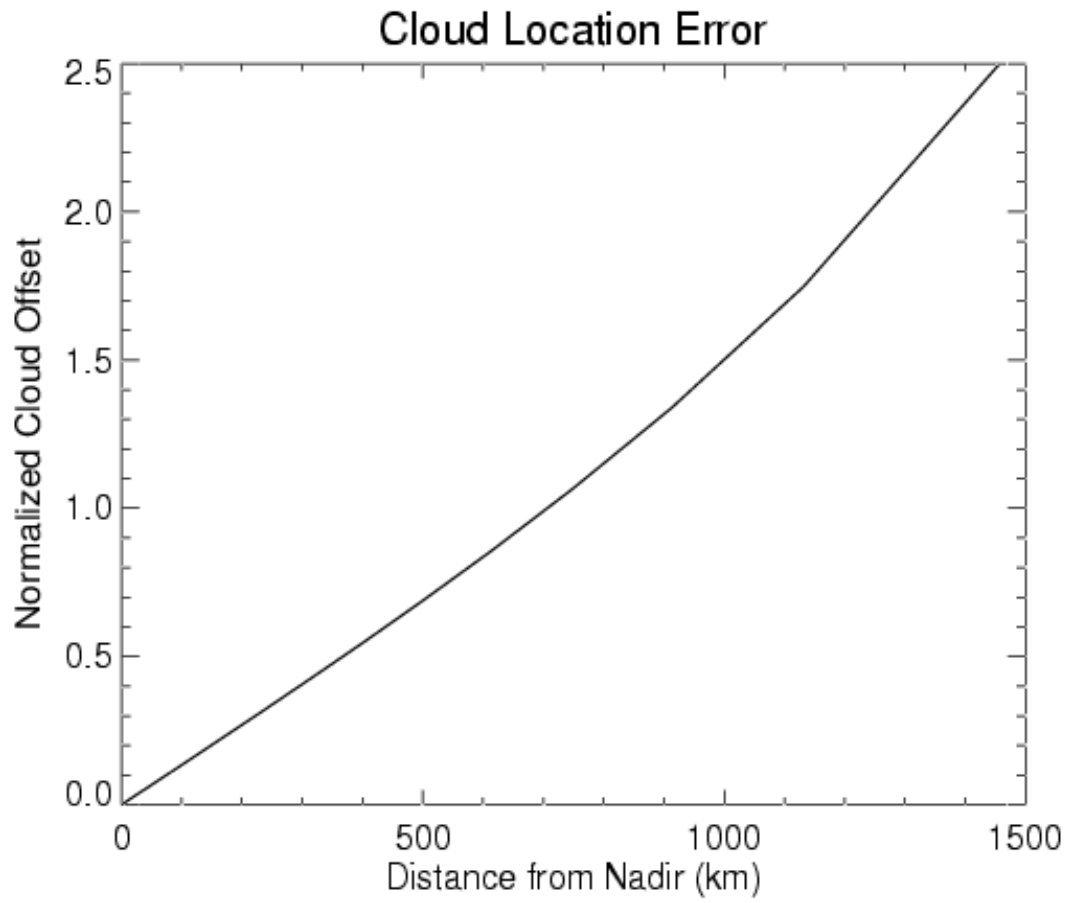


Figure 6: Error in cloud position due to parallax, relative to the cloud height.

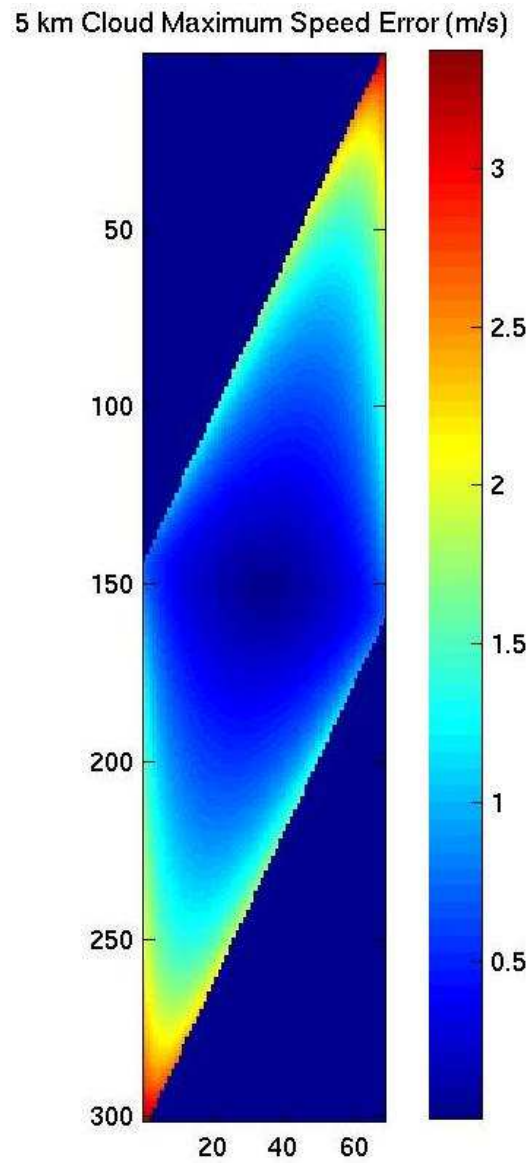


Figure 7: Error in wind speed (m s^{-1}) due to parallax shift. The parallelogram approximates the overlap region in three orbits as seen in Figure 3.

2.2.6 Atmospheric considerations

The meteorology over the Arctic and Antarctic presents challenges in remote-sensing and the wind-derivation process over what is typically encountered in middle- and lower-latitudes.

The cold, dry air over an ice (or very cold) surface is further complicated by the high terrain regions of Greenland and the Antarctic continent. The primary problem is in the height assignment algorithm where these environmental conditions have not been strictly accounted for:

1. There is a persistent low-level inversion evident in a profile of the Arctic standard atmosphere (Figure 8). This inversion, and possible isothermal layer, near 900 hPa could result in assigning a wind at an incorrect level because the clouds are thin and warmer than the surface. Since the height assignment routine begins at the top of the temperature profile and descends through the atmosphere to find the height that corresponds to the cloud brightness temperature, these clouds will appear too high in altitude. Nevertheless, this has not caused problems because many of these are filtered out in the quality control process and all NWP centers only retain high-altitude winds over land (generally above 600 hPa). This threshold is also applied to winds from geostationary satellite images.
2. Because of the dry conditions in the polar regions, there are fewer clouds for tracking compared to lower latitudes. Therefore, the majority of the MODIS winds are derived from water vapor images, many of those are designated as clear-sky. Since there is less than 1 cm of total precipitable water, on average, over the Arctic even in the summer (Figure 9), tracking features in the water vapor channel are potentially problematic. At times, surface features are apparent even though the channel peaks in the mid-troposphere. In these very dry situations, the water vapor targets will probably be assigned a height that is too low. This effect has not been quantified.

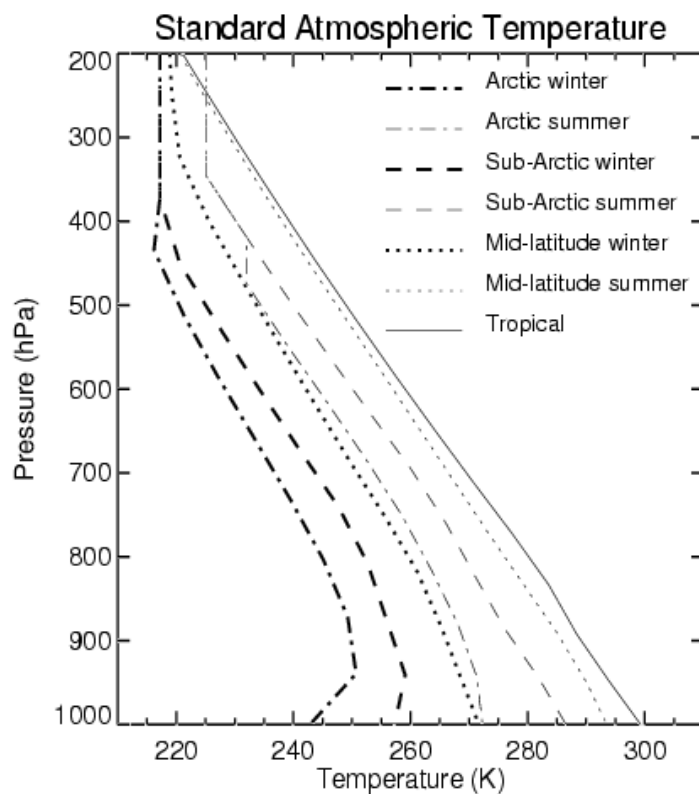


Figure 8: Standard atmosphere profile showing the persistent low-level inversion in the Arctic region (courtesy of Jeff Key).

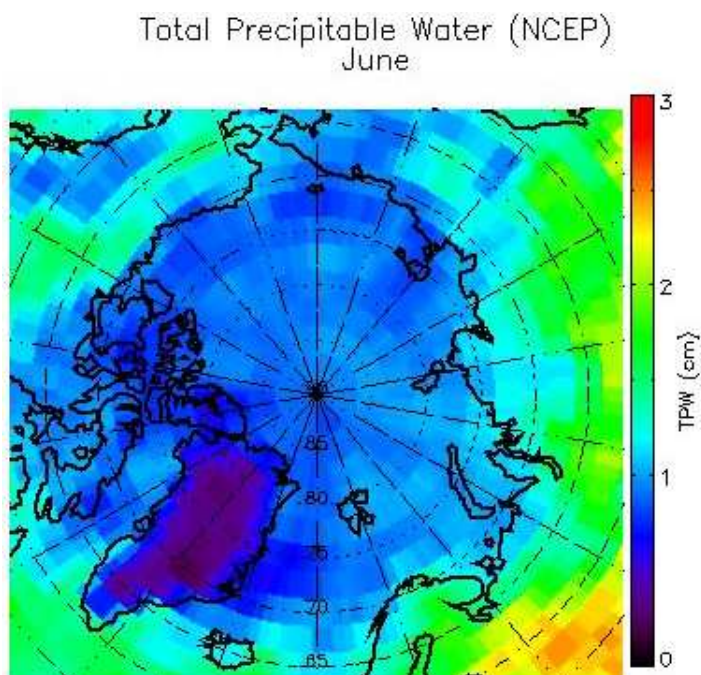


Figure 9: Average Total Precipitable Water over Arctic region in June from NCEP (courtesy of Jeff Key).

Despite these two major issues, the MODIS winds are still of value because the filtering and quality control at both CIMSS and the NWP sites will remove many of these erroneous winds. However, it is recognized that improvements to the current techniques should result in more and better quality satellite-derived winds.

2.2.7 Validation of MODIS polar winds

Rawinsondes are traditionally used to determine the accuracy of the satellite-derived winds. Validation of the MODIS winds is complicated by the lack of an extensive network of rawinsondes in the polar regions (Figure 1). Nevertheless, the following tables show that the MODIS winds have comparable errors to the geostationary satellite-derived winds.

Table 1 contains the Arctic statistics for the first MODIS winds experiment, a 30-day case study from 5 March to 3 April 2001 (more details on this winds dataset in the section *Early Experiments*). From a total of 927,000 winds at all height levels, there were 27,000 vectors within 150 km and +/- 1.5 hours of a rawinsonde report, which are the standard criteria used by NESDIS for comparison. This means only about 3% of the total winds generated were compared to rawinsondes. This is not solely due to the scarcity of rawinsonde locations but also to their availability every twelve hours. Since there are very few upper-air observations over the Antarctica, no statistics were computed in the southern polar region.

Table 1: Comparison (m s^{-1}) of Terra MODIS satellite winds, at all levels, to rawinsondes. Northern Hemisphere: 27,000 samples (90% WV) 5 March to 3 April 2001.

All levels	Satellite wind	Guess wind	Rawinsonde wind
NRMS difference	0.57	0.53	
RMS difference	8.11	7.29	
Average difference ($V_{diff_{mean}}$)	6.87	6.10	
Standard deviation ($V_{diff_{std}}$)	4.32	4.00	
Speed bias	-0.58	-1.14	
Speed (S_{avg})	14.31	13.76	14.89

The satellite-derived wind statistics are based on the vector difference between the MODIS and the rawinsonde winds using the following equation:

$$V_{diff} = \sqrt{(\bar{u} - u)^2 + (\bar{v} - v)^2} \quad (5)$$

where u , v are the satellite vector wind components and the overbar variables are the means from the rawinsonde. The guess wind statistics are determined similarly by using time and space interpolated guess winds to the MODIS winds locations. The RMS and normalized RMS (NRMS) differences are computed from the V_{diff} values by:

$$RMS = \sqrt{V_{diff_{mean}}^2 + V_{diff_{std}}^2} \quad (6)$$

$$NRMS = RMS / S_{avg} \quad (7)$$

where S_{avg} is the average speed.

The quality of the MODIS satellite winds in this first experiment is slightly less than the background guess wind, except for the speed bias which is better by about 0.5 m s^{-1} . The lower quality is not too surprising considering that clouds and water vapor features are not always true tracers of atmospheric motion at a specific level, but comparable errors to the

background field indicate that there should be real value in satellite-winds in data void regions. This is confirmed with the positive impact in forecasts using these polar winds.

An additional validation metric for determining the representativeness of the errors in the MODIS winds is to compare them to the errors in geostationary satellite winds. Recent statistics in Table 2 (GOES-12) and Table 3 (Terra MODIS) show similar values to the initial statistics computed in the first experiment.

Table 2: Comparison (m s^{-1}) of GOES-12 WV satellite winds to rawinsondes. Northern Hemisphere: 20,300 samples in December 2006.

All levels	Satellite wind	Guess wind	Rawinsonde wind
NRMS difference	0.28	0.24	
RMS difference	7.72	6.80	
Average difference	6.35	5.53	
Standard deviation	4.40	3.96	
Speed bias	-0.07	-1.12	
Speed	27.97	26.91	28.04

Table 3: Comparison (m s^{-1}) of Terra MODIS WV satellite winds to rawinsondes. Northern Hemisphere: 4,600 samples in December 2006.

All levels	Satellite wind	Guess wind	Rawinsonde wind
NRMS difference	0.44	0.41	
RMS difference	6.79	6.37	
Average difference	5.64	5.25	
Standard deviation	3.79	3.61	
Speed bias	-0.43	-1.03	
Speed	15.19	14.59	15.62

Note that the NRMS difference in the MODIS winds is much higher than the geostationary winds. This is due to the average wind speed is much faster for the GOES-12 winds, with the RMS differences about the same. One would expect lower speeds in the MODIS winds to result in smaller errors, but this discrepancy may be the result of the 100-minute time interval between images resulting in more variability in the winds.

3. Use of polar winds in global models

Several polar winds experiments were designed and implemented in collaboration with various NWP centers to assess the impact of the MODIS winds in global model forecasts (Key et al. 2005). As the value of these winds were recognized and put into more operational models, the technology developed at CIMSS for producing winds from polar orbiting satellites was transferred to NOAA/NESDIS, where the MODIS winds are now part of the operational suite of products. This section examines the early experiments, the difficulties with assimilating satellite-derived winds in numerical models, the impact on forecasts, and the use of the MODIS winds at operational NWP centers.

3.1 Early experiments

It was determined that a one-month dataset of polar winds would be the minimum needed to gauge the impact of the polar winds in forecasts. NASA's Data Assimilation Office (DAO), now the Global Modeling and Assimilation Office (GMAO), and the ECMWF were the first two modeling centers to test the impact of the MODIS winds. In preparation for generating the winds dataset, several thousand MODIS granules (a five-minute swath of data) were retrieved from the GSFC Distributed Active Archive Center (DAAC). The granules were then remapped, composited, and processed through the winds algorithm. This procedure took about six months to complete and resulted in the generation of over 1.6 million vectors, summarized in Table 4. Basic statistics of the MODIS winds over the Arctic are in Table 1.

**Table 4: Number of MODIS winds from Terra derived in the first experiment:
5 March to 3 April 2001.**

	Water Vapor	Infrared	Total
Arctic	780,000	147,000	927,000
Antarctic	634,000	126,000	760,000

The DAO and ECMWF independently came to the same conclusion: when the MODIS winds are assimilated, forecasts of the geopotential height for the Arctic, the Northern Hemisphere extratropics, and the Antarctic are improved significantly, especially in the three- to five-day forecasts (Key et al. 2003).

The success of this first experiment resulted in implementing a processing system that would generate the winds routinely, in near real-time, for continuous input into numerical models. This was developed at CIMSS (Santek et al. 2002; Santek et al. 2004) and later a nearly equivalent processing system was implemented at NESDIS.

As more NWP centers began using the winds routinely, a second experiment was designed for all users of the winds to determine the impact over a specified time period. The goal was to examine how the impact varied between different numerical models. Wind sets were generated by both CIMSS and NESDIS for this experiment entitled MOWSAP (MODIS Winds Special Acquisition Period). MOWSAP ran from 1 January 2004 to 15 February 2004. *Appendix B: Polar Winds Impact Reported at IWW* summarizes statements from modelers at the Seventh International Winds Workshop (IWW) on the impact polar winds have on forecasts.

3.2 Data assimilation issues

NWP centers have difficulty assimilating satellite-derived AMVs for a variety of reasons and it's not done consistently throughout the modeling community. Despite these shortcomings and variability in use, the MODIS winds have shown a positive impact in forecasts at many different NWP centers. Although no attempt was made to account for these problems in the current research, a summary of these issues is presented below as evidence that "poor data" (data lacking complete error characterization) can provide useful information in data void regions:

1. There is little error information provided with each observation. There are quality measures which assist in distinguishing a good from a poor vector, but thresholds are empirically determined by each NWP center. What is needed by the assimilation system is errors in the same units as the measured observation: m s^{-1} for the u- and v-components and hPa for the assigned level.
2. There are spatially correlated errors in the wind derivation technique. This violates an assumption of the assimilation process that observation errors are not correlated. These errors are on the order of 3 m s^{-1} and are due to (Bormann et al. 2003):

- a. The use of forecast temperature and humidity profiles for the height assignment. These profiles inherently have spatially correlated errors and mostly likely contribute to the largest AMV correlated error.
- b. Tracking targets in nearby regions may result in similar height assignment and tracking errors.
- c. The quality control techniques tend to favor winds that are consistent with nearby winds.

3. The winds algorithm assigns a single level to the vector, although it is well-recognized that clear-sky water vapor winds represent a layer (Rao et al. 2002).
4. Varying thresholds, weights, and blacklisting criteria are used by the different NWP centers. This is discussed in detail below.

3.2.1 Filtering the MODIS winds

Usually, not all AMVs are assimilated. A proven blacklisting scheme, used with the geostationary AMVs, is applied to the MODIS winds. For example, thresholds related to quality indicators, vectors too close to the surface, and speeds that deviate too much from the model background are applied to filter the winds. From Zapotocny et al. (2007), the MODIS winds were not assimilated by the Global Data Assimilation System (GDAS), which is used with the NCEP's GFS model, if:

1. they were above the tropopause. Some MODIS winds are erroneously tagged above the tropopause due to problems in height assignment near that inversion and using a forecast temperature profile.
2. they are closer than 200 hPa to the ground.
3. the difference between the observation and the model background is greater than 7 m s^{-1} .
4. the RFF is greater than or equal to 65 (see section 2.1 *Geostationary satellite winds algorithm* section for details on the RFF).

MODIS winds are incorporated similar to the geostationary winds with the same assimilation weights and the use of the re-assigned heights from the auto-editor.

However, the criteria vary among the different NWP centers. In comparison, the ECMWF uses winds if (Bormann and Thépaut 2004):

1. they are above 400 hPa over land.

2. they are above 700 hPa (IR) and 550 hPa (WV) over water.
3. the QI exceeds a varying threshold, dependent upon the latitude, spectral channel (IR, WV, or Visible), and altitude (Rohn et al. 2001).

Other criteria are used to thin the data (minimum spacing between vectors) and discard vectors that deviate too much from the first guess field (Rohn et al. 2001).

Another criterion is the timeliness of the data. If the winds are not available by the assimilation cutoff time, they can not be used. Bormann and Thépaut (2004) determined that only about 20% of the winds generated are not available in time for assimilation for the ECMWF model.

Each center has derived its own list of thresholds and criteria for blacklisting satellite-derived winds. Despite these differences, the impact of the MODIS winds on forecasts is significant and some representative examples are presented in the next section.

3.2.2 Measuring the impact on forecasts

The typical method used to determine the quality of a forecast is the calculation of the anomaly correlation. The anomaly correlation is defined as the correlation between the predicted and analyzed anomalies of the variables. These anomalies are deviations from the mean climatological values (Krishnamurti et al. 2003). The anomaly correlation coefficient (ACC) is defined as:

$$ACC = \frac{\sum \left\{ [(Z_F - Z_C) - (\overline{Z_F - Z_C})] [(Z_V - Z_C) - (\overline{Z_V - Z_C})] \right\}}{\sqrt{\sum [(Z_F - Z_C) - (\overline{Z_F - Z_C})]^2 \sum [(Z_V - Z_C) - (\overline{Z_V - Z_C})]^2}} \quad (8)$$

where Z is the geopotential height (usually 500 or 1000 hPa) and the subscripts refer to F (forecast), C (climatology), and V (verifying analysis).

Examples from two NWP sites are used to illustrate different ways the ACC score is presented, for example: mean ACC values vs. forecast day or as a time series of daily values for a specific forecast day. Figure 10, from ECMWF, is the classic signature that the MODIS winds have on forecasts. This represents a monthly mean from the first experiment in March 2001. Over the Northern Hemisphere, the MODIS winds have neutral impact on the forecasts out to about two days. From Day 3 to Day 5 a positive impact is evident and increases later in the forecast period. How much of this hemispheric improvement is only due to a significant improvement in the polar regions? Bormann and Thépaut (2004) reported a statistically positive impact in the Day 8 forecast over Europe and the N. Atlantic Ocean for an experiment in the summer of 2002. They found that the largest improvement over Europe was dependent on synoptic flow, being more sensitive to north or northwesterly flow over the N. Atlantic. Riishojgaard and Zhu (2004) reported a slight positive impact in the Day 5 mid-latitude-only ACC score, being more significant in the Southern Hemisphere. These findings would indicate that changes in the polar regions in the analysis are propagating into mid-latitudes in later forecasts. One mechanism to explain this is shown in Figure 11. This is a conceptualized view of the indirect circulation near the jet stream: parcels descending from the mid-troposphere poleward of the jet to lower levels in mid-latitudes. Figure 12 gives the actual trajectories based on NCEP's GFS model forecast, showing that it only take 48 hours for an air parcel to move from the mid-troposphere over Siberia to low levels over the western US.

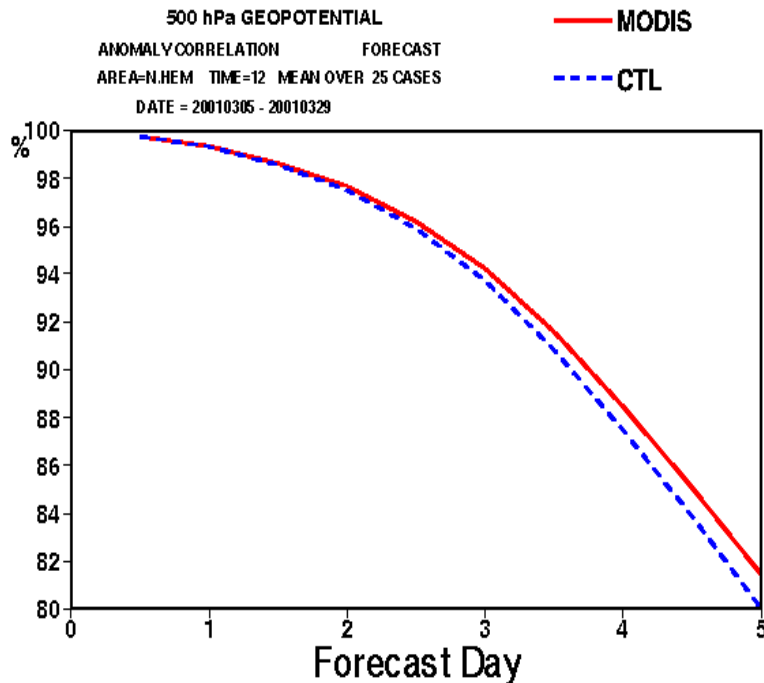


Figure 10: Anomaly correlation for 500 hPa geopotential, each experiment verified against its own analysis. Forecast scores are the correlation between the forecast geopotential height anomalies, with and without the MODIS winds, and their own analyses. (Courtesy of ECMWF)

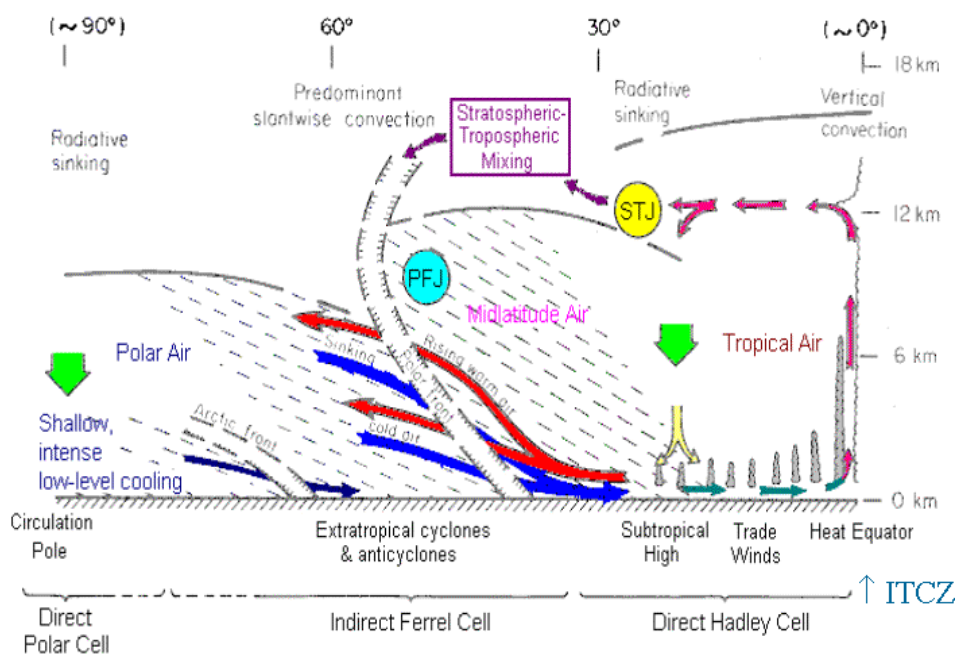


Figure 11: Meridional cross-section from the equator to the pole (from Palmén and Newton, 1969).

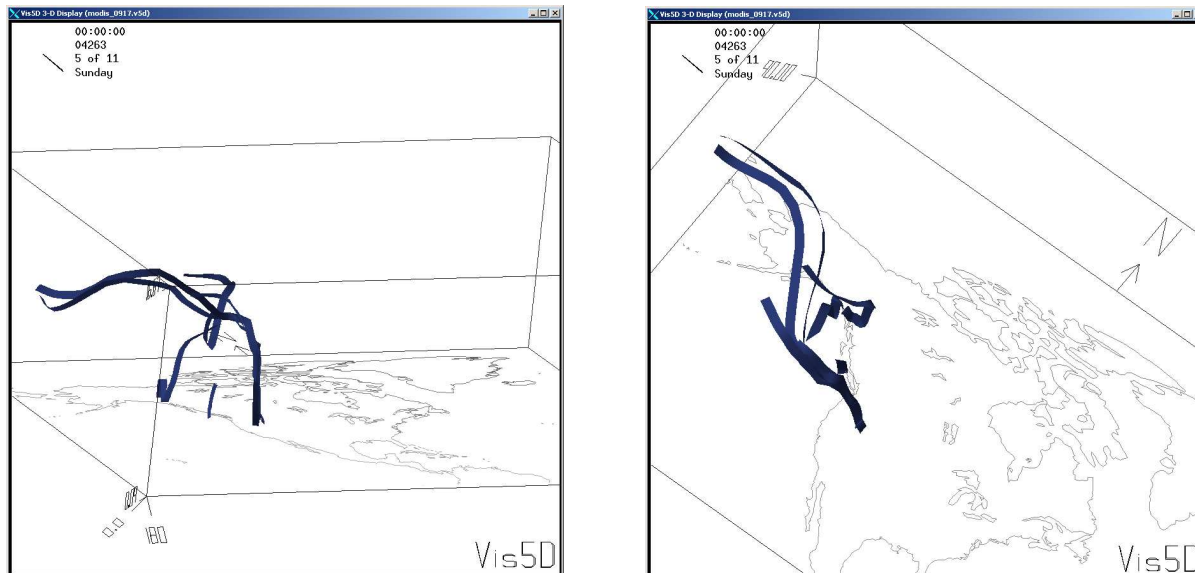


Figure 12: The ribbons depict trajectories originating in Siberia that arrive in the western US in about 48 hours, descending from about 8-9 km to the surface. The left panel shows the vertical descent; the right panel is a view from the top to show the horizontal displacement. These are extracted from forecast fields of u,v,w from the GFS model initialized at 17 September 2004 at 0000 GMT.

The daily scores of the 500 hPa ACC show an interesting signature that has been observed by more than one center (Figure 13 and Figure 14). Figure 13 is a one-month period in the summer of 2003 for the 60-hour forecast. On any given day, the impact of the MODIS winds is very small: sometimes better, other times worse. However, towards the end of the period there is a forecast bust, where the ACC drops significantly¹. The drop in the ACC is much less for the forecast including the MODIS winds. Figure 14 is from the GFS during the late-summer 2004 and a similar impact is observed. Riishojgaard et al. (2006) found that in mid-latitudes the “main contribution of the MODIS wind observations is to reduce the severity of the forecast busts.” This implies that some poor forecasts may be the

¹ It is not known to the author how much a single forecast bust improvement in the ACC would impact a monthly mean (as in Figure 10).

result of a lack of information about high-latitude weather systems (Bormann and Thépaut 2003) that subsequently impact the mid-latitude flow.

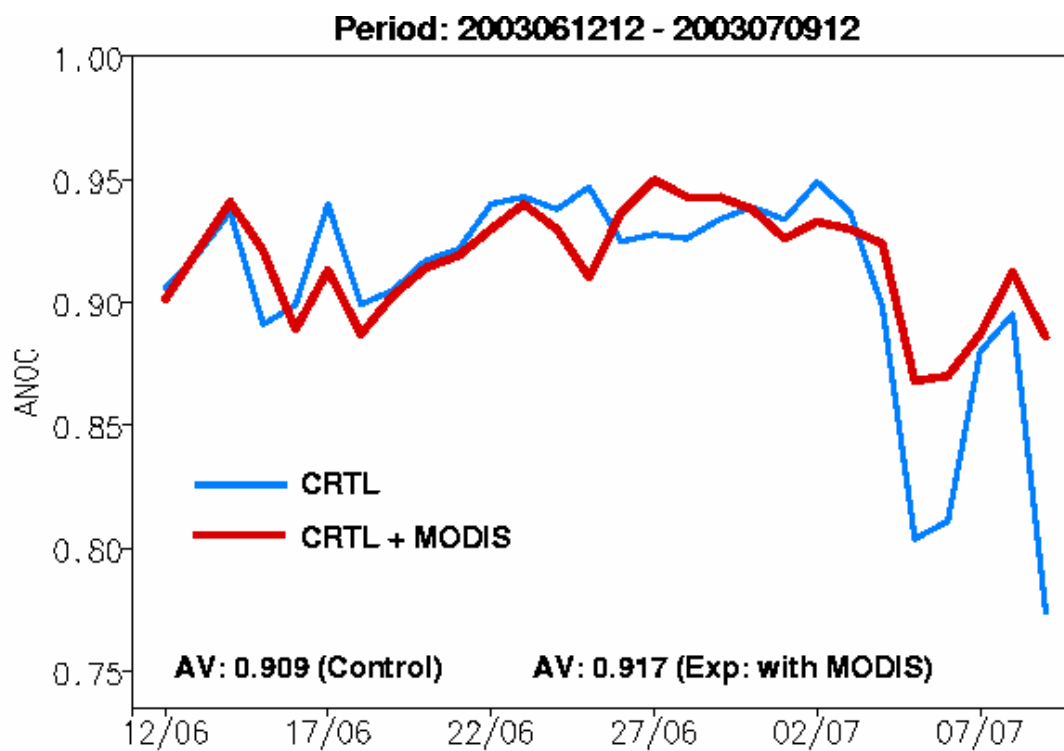


Figure 13: 60-hour ACC for the northern hemisphere 500 hPa geopotential heights from the Deutscher Wetterdienst (DWD) global model. Time period is from 12 June to 9 July 2003 (from Cress 2004).

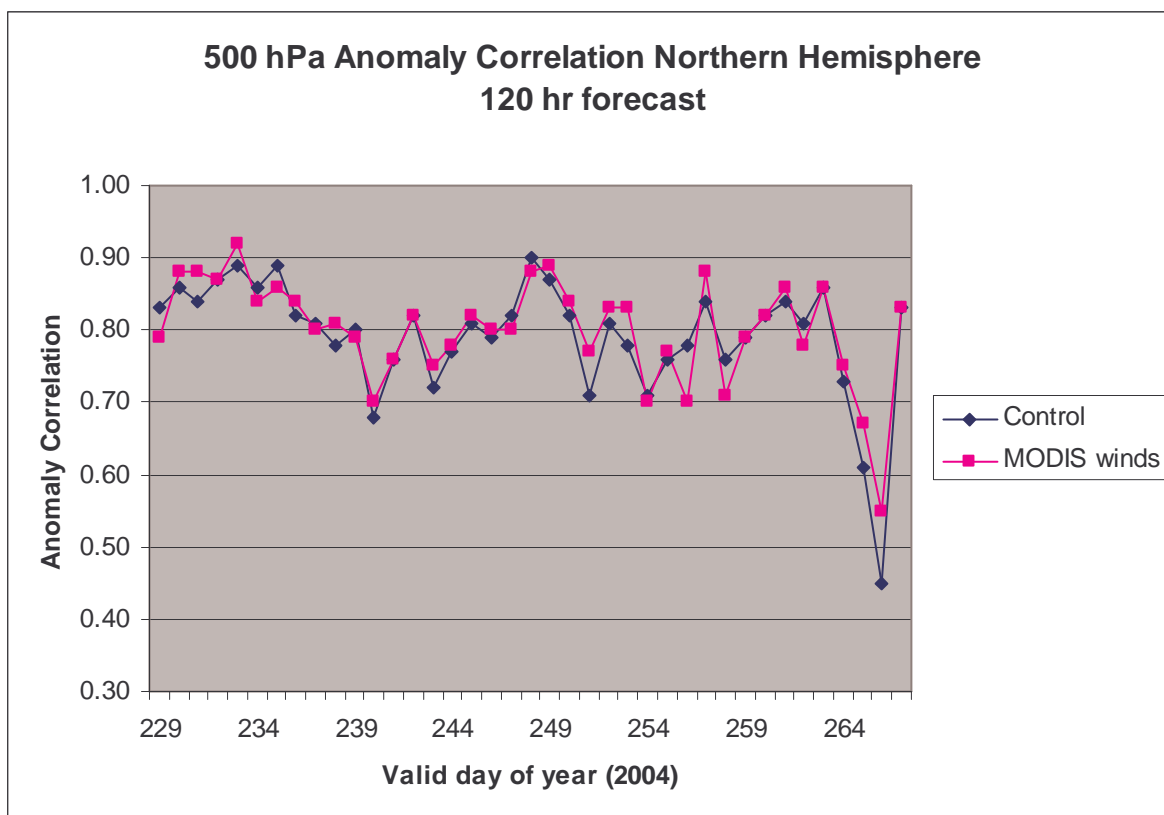


Figure 14: GFS 120-hour ACC for the northern hemisphere 500 hPa geopotential heights from 11 August to 22 September 2004.

In addition to the ACC score, other parameters have been used to determine the impact of the MODIS winds on forecasts. Figure 15 depicts accumulated snowfall for a 5-day forecast (Bormann and Thépat 2003). The top panel is the control run (no MODIS winds), the middle panel included the MODIS winds, and the bottom panel is the verifying analysis. The forecast with the MODIS winds is much better than the control, which was due to a modification of a low pressure system north of Alaska (not shown). As the low moved southward across Alaska during the forecast period, it was not as intense as the control had it, resulting in less precipitation in southern Alaska.

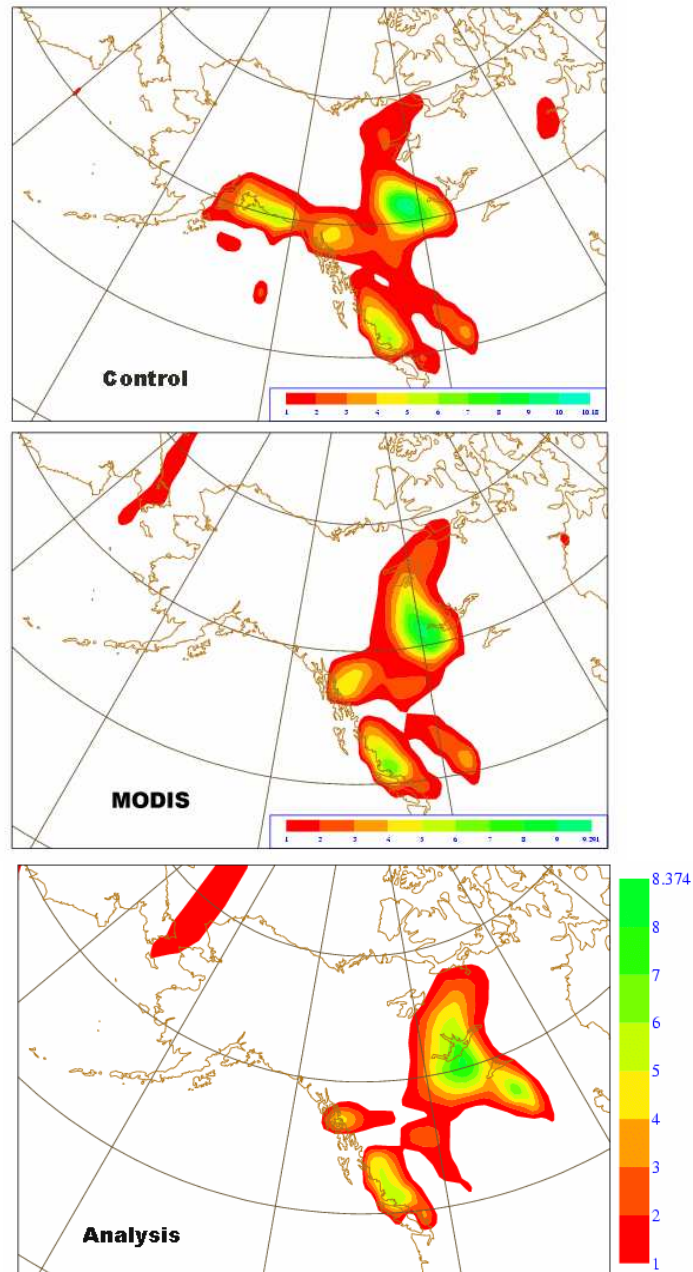


Figure 15: Accumulated snowfall forecasts (mm water equivalent) over Alaska for 20 March 2001. Inclusion of MODIS winds in the analysis produced a more accurate forecast. Top is the snowfall from the 5-day Control forecast (no MODIS winds); middle is the snowfall from the 5-day forecast that included the MODIS winds in the analysis; bottom is the snowfall from a 12-hr forecast for verification (“truth”). (Courtesy of ECMWF)

3.3 Operational use of MODIS winds

The positive impact of the MODIS winds has been documented in the literature (Key et al. 2003; Pauley and Pauley 2004; Bormann and Thépaut 2004; Pauley and Pauley 2005; Zapotocny et al. 2006). The consistent results between NWP centers resulted in all of the major centers to include the polar winds in their global operational models. Table 5 enumerates the sites along with their operational begin date.

Table 5: Operational use of MODIS Polar Winds as of January 2007

<u>NWP Site</u>	<u>Operational Begin Date</u>
ECMWF European Centre for Medium-Range Weather Forecasts	January 2003
GMAO Global Modeling and Assimilation Office	Unknown
JMA Japan Meteorological Agency	May 2004
CMC Canadian Meteorological Centre	September 2004
FNMOG US Navy, Fleet Numerical Meteorology and Oceanography Center	October 2004
Met Office United Kingdom	January 2005
NCEP National Centers for Environmental Prediction	November 2005
DWD Deutscher Wetterdienst	Early 2006

4. Model experiments

There are two types of data used in this study: the satellite-derived winds and the output of the model runs that include the satellite-derived winds (and a control). The previous sections provided some background information and statistics of the MODIS winds. But, the primary data used in the analysis in the following sections are model output from experiments run using the GFS and the Navy Operational Global Atmospheric Prediction System (NOGAPS) models.

There are many remotely-sensed measurements over the polar regions from polar orbiting satellites that are assimilated into global forecast models, but their measurements don't stop there as they extend to all latitudes along the path of the satellite. The one exception is the MODIS winds, as they are only poleward of 65° latitude, and for this reason they are a unique dataset to investigate their global impact. The ability to routinely derive winds from a sequence of polar orbiting passes was developed at CIMSS in 2001 for the primary purpose of determining the impact that polar winds have in global numerical model forecasts. Since then, it is estimated that over 100 million winds have been produced and retrieved by NWP sites worldwide.

Our collaborations with the NWP centers that make use of the MODIS winds resulted in our ability to have access to the output of some of the experimental runs for analysis. Data was acquired for the GFS model from NCEP and for the NOGAPS model from the Naval Research Laboratory (NRL); the primary analysis used the GFS output. As a check on how representative the polar winds assimilation was in the GFS, output from the NOGAPS was examined. Also, output from global Advanced Microwave Sounding Unit (AMSU) radiance assimilation was qualitatively compared to the polar winds impact in terms of the magnitude

and geographic influence. The AMSU radiances are a much different data type (global coverage and they directly affect the temperature field) and they provide an interesting contrast to assimilating a mass-based parameter only over the polar regions.

4.1 MODIS winds assimilated in the GFS

Using the operational version of the NCEP's assimilation system (GDAS) and the pre-operational model (GFS), a side-by-side experiment was run for a six-week period from 10 August to 18 September 2004, with and without the MODIS polar winds². This model has a resolution of T254 with 64 layers (Jung et al. 2007). T254 corresponds to a horizontal grid point spacing of approximately 0.5 degrees. Cases were chosen well into the experiment so that any 'data shock' adjustments are not an issue in interpreting the differences in the model runs.

The GFS model output was provided in GRIdded Binary (GRIB) format on constant pressure surfaces at 50 hPa intervals. The precision of the output variables is 0.1 units.

Several cases within this period have been examined to determine how winds in the polar regions may affect the height and wind fields into the lower latitudes. Since the largest impact reported by NWP centers is in the 3- to 5-day forecast, the ACC for the 120-hour forecast is used to choose the cases (Figure 14). Forecasts for five cases were chosen based on the ACC and long-lived tropical cyclones (Table 6).

² Zapotocny, personal communication, 5 February 2005; Jung, personal communication, 11 April 2005.

Table 6: Five cases from September 2004. The ACC values are northern hemisphere, 120-hour forecast for all wave numbers.

Day	MODIS ACC	Control ACC	Comments
Case 1: 06 Sep 2004	0.77	0.76	ACC similar
Case 2: 07 Sep 2004	0.71	0.78	MODIS ACC worse
Case 3: 11 Sep 2004	0.82	0.82	Hurricane Ivan
Case 4: 12 Sep 2004	0.86	0.84	ACC similar
Case 5: 17 Sep 2004	0.55	0.45	Forecast bust Hurricane Karl

The five cases chosen include positive, neutral, and negative forecast impact and two Atlantic tropical cyclones, Ivan and Karl. Even though it is late summer and the dynamics are stronger in the southern hemisphere, cases in the northern hemisphere were chosen because the verification of the forecast is better in the north (due to more traditional observations) and to investigate the impact on hurricane track forecasts.

4.2 Additional model experiments

In addition to the MODIS winds in the GFS model, two additional experiments were investigated: the assimilation of MODIS winds in the NOGAPS model and AMSU radiances in the GFS. Although these additional datasets are in two different years (but during the same season), they do provide a qualitative measure of how representative the impacts observed in the analyses and forecasts are, compared to when the same data type is used in a different model and a different data type is assimilated into the same model.

An experiment similar to the GFS was performed using the NOGAPS model for the same season in a different year, 2005. The models are both spectral but the assimilation systems are different. The GDAS (input to the GFS) uses the Spectral Statistical Interpolation (SSI) scheme, while the Naval Research Laboratory Atmospheric Variational

Data Assimilation System (NAVDAS) (Daley and Baker 2001) (input to the NOGAPS) is a gridpoint assimilation system. This difference may be important in how and where the MODIS winds impact the analysis.

The third experiment uses the GFS model assimilating global AMSU radiances, which are run for the same season, but in yet a different year (2003). It is important to note that this dataset is global and is included as standard data in the MODIS winds experiment, conducted in 2004.

Since the other experiments are in different years, they cannot be directly compared, but instead the *patterned features of the differences are important*. This is a qualitative measure of how the data affect the forecasts by examining how the patterns of the difference features are similar or dissimilar in the different experiments.

4.3 MODIS winds dataset

MODIS winds derived operationally at NOAA/NESDIS are input in the GFS model. These winds are very similar to what is produced at CIMSS. The primary difference in the processing is that NESDIS uses the Euclidean norm correlation, while CIMSS uses the cross correlation technique. It appears that the cross correlation method result in more wind vectors in regions of weak gradient. NWP centers have evaluated both sets of winds and have found very similar impacts from both. This is probably due to the filtering and thinning which substantially reduces the winds vectors that are actually assimilated.

The wind coverage for a specific assimilation cycle is shown in Figure 16. The 0000 GMT run uses winds from 2100 to 0300 GMT available by 0600 GMT. This results in good coverage over the Arctic except from 0 to 60 E. Therefore, 83% of the region north of 70°N latitude has MODIS wind observations at each assimilation time. The 60 degree gap appears

in different areas of the polar region depending on the time of day. For the five case studies, Table 7 summarizes the number of winds generated at CIMSS, which are generally higher than those from NESDIS.

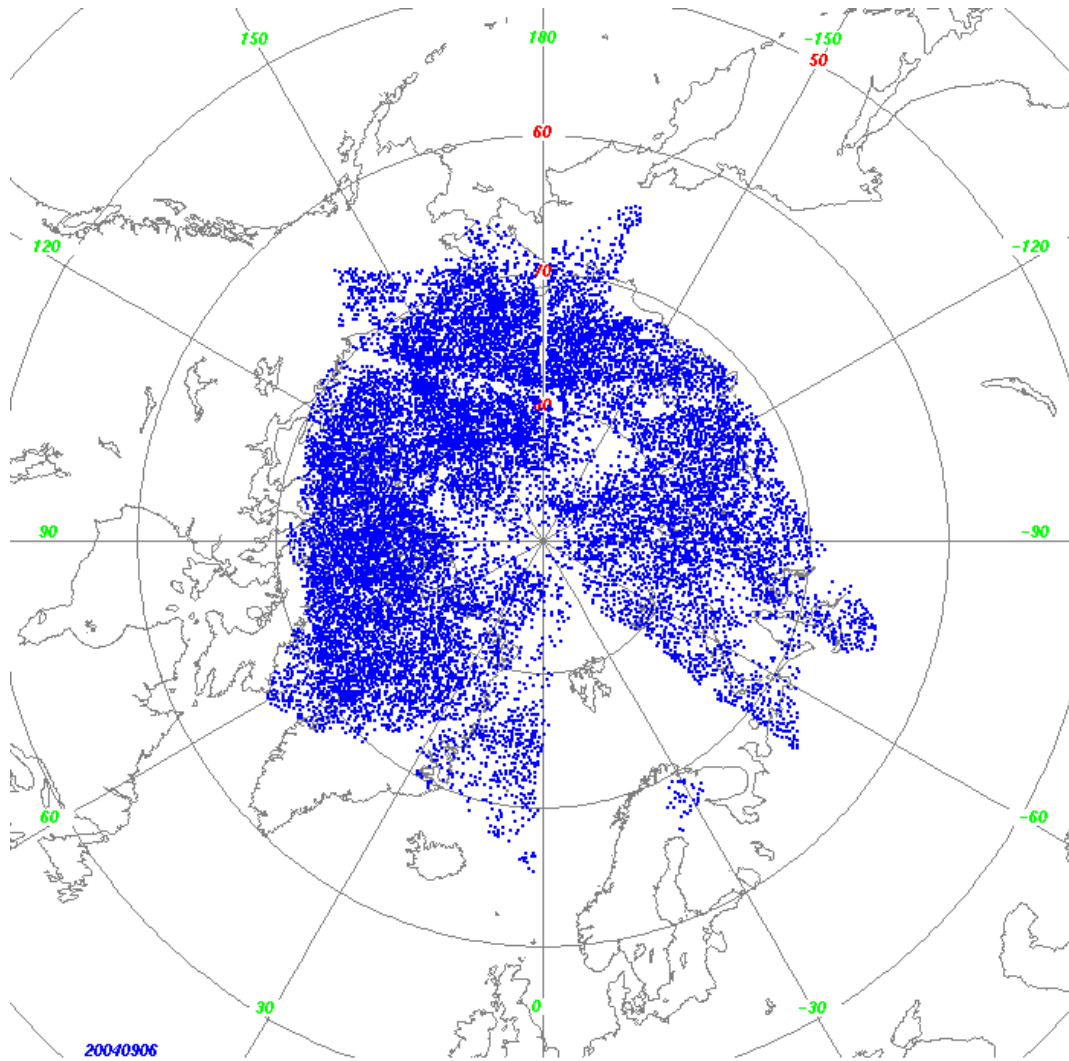


Figure 16: MODIS wind coverage for the 0000 GMT assimilation cycle on 06 September 2004. There are about 21,300 winds at this time: +/- 3 hours from model run time, arriving by 6 hours after the synoptic time.

Table 7: Number of MODIS wind observations that are potentially available for the 0000 GMT cycle for the five case studies.

Day	Number of Winds
06 Sep 2004	21,300
07 Sep 2004	12,271
11 Sep 2004	15,075
12 Sep 2004	7,115
17 Sep 2004	15,303

There are many fewer winds on 12 September 2004. Since the winds-generation process runs in an unattended mode, there are several common problems that have been observed that cause many fewer winds to be generated: problems with the processing of the raw MODIS data at the GSFC, missing background grids, and networking issues.

Possible mechanisms that propagate polar AMV information into lower latitudes

Two areas are investigated to explain the differences in the two model runs: data assimilation and dynamics near the jet stream. A few aspects of data assimilation are presented because the addition of any data results in adjustments to the model atmospheric state. For example, the mass balance is affected by adding wind information and the temperature field is affected by the inclusion of satellite radiances. Once the data are assimilated, differences in the analysis and subsequent forecasts are examined in terms of dynamical parameters based on the available model output fields. These differences will be used to explain how the addition of polar winds can affect lower latitude weather systems.

4.4 Data Assimilation

The effect of MODIS winds on the GFS analysis may be due, in part, to factors inherent in the assimilation system, such as a dynamic bias correction, spectral assimilation, and gravity waves. These can spread over the entire domain very quickly; faster than atmospheric dynamics can explain.

4.4.1 Dynamic bias correction

A bias correction is a statistical technique to account for systematic errors in the observations, which is important since the assimilation system assumes only random errors are present. A dynamic bias correction for satellite radiances is built into the GDAS, which is unlike other observations (such as, rawinsondes) where the bias correction is applied outside the assimilation. This correction accounts for the combined biases in the radiative forward model, instrument, number of vertical levels, airmass, etc. which can not be determined independently. However, this dynamic bias correction may result in changes to the analysis

in regions far away from the observed radiance data or from the inclusion of other types of data. Two examples follow.

Su et al. (2001) showed that the assimilation of GOES imager water vapor radiances had a similar impact over the Indian Ocean as they did within the GOES-8 and GOES-10 coverage areas in the western hemisphere. In this case, the bias correction for AMSU-B and HIRS radiances changed slightly, which spread throughout the entire model domain.

The addition of the MODIS winds may affect the radiance bias correction as when satellite winds are added, an adjustment takes place in the height field (conservation of momentum), which in turns affects the temperature field (thermal wind balance constraint), which alters the radiance bias correction, which propagates globally. Therefore, adding MODIS winds has a direct effect on the satellite radiance bias correction. It is not known how large this effect is.

The GDAS bias correction is dynamic. It starts with a guess from the previous analysis and is modified within the analysis. NAVDAS uses a static bias correction. Having a static bias correction would mean the effects would not propagate globally quickly. Instead, it would occur through the forecast³.

4.4.2 Spectral assimilation

The SSI (Parrish and Derber, 1992) used in the GDAS has two characteristics that may make it difficult to interpret how the addition of data affects the forecast:

1. All the data are interpolated globally. The weighting is less for observations farther from the grid point, but it is evident in poorly observed regions.

³ Jung, personal communication, 15 August 2005.

2. The analyses are initialized as an independent step resulting in adjustments away from the data. This initialization is necessary to correct for any imbalance in the mass and temperature fields that could result in amplifying gravity waves.

These result in changes in regions away from the observed data, which will undoubtedly affect the forecasts. Examining difference fields in the analyses may give an indication of how important these characteristics are, but it is complicated by the fact that MODIS winds are continually assimilated so their affect is cumulative. This will be most evident in data void regions.

4.4.3 Gravity waves

Gravity waves may affect the entire circulation in just a few time steps, in as little time as a few minutes. Grid point models may change the fields farther away faster through gravity waves than spectral models. Even though spectral models truncate to a certain maximum wave number every time step, changes to all fields will still occur rather quickly and spread throughout the entire domain⁴.

4.5 Dynamics

The classic equator-to-pole cross-section from Palmén and Newton (1969) (Figure 11) illustrates the importance of understanding the state of the atmosphere near the polar jet stream, the vehicle carrying synoptic-scale weather systems. Equatorward of the jet is where the primary observing network is. The MODIS winds are derived generally poleward of the polar jet, where conventional weather observations are relatively scarce. One would expect that this information would improve the representation of the mass field in the model. Thus,

⁴ Zapotocny, personal communication, 15 Aug 2005.

the circulation and extent of the jet on the poleward side would be better defined, as far south as the transition region between the polar and Ferrell cells.

The cloud and water vapor features tracked in the MODIS water vapor channel are near the polar tropopause, usually in the range of 400 to 500 hPa (about 6 km). The infrared winds are generally lower, because the vertical cloud extent is suppressed in the cold, dry polar region. Since the majority of the winds are from the water vapor channel, most of the analysis in this study will be on the 500 hPa surface.

Two basic concepts were considered when attributing changes in the wind field to affecting dynamics near the jet stream:

1. Zonal phase speed of synoptic-scale Rossby waves
2. Ageostrophic wind relationship to wave propagation

4.5.1 Rossby wave

The barotropic Rossby zonal wave speed is (Holton 1992):

$$c_x = \bar{u} - (\beta / K^2) \quad (9)$$

where \bar{u} is the mean zonal wind speed, β is the earth's vorticity gradient, and K is the total horizontal wave number ($K^2 = (l^2 + k^2)$, where the wavenumbers k and l are equal to $2\pi/\text{wavelength}$). As an example, for a 6000 km wave at 50°N latitude ($\beta = 1.4 \times 10^{-11} \text{ m}^{-1} \text{ s}^{-1}$), the zonal wave speed is about 7 m s^{-1} slower than the mean zonal wind speed.

According to the Rossby equation (Eq. 9), there are two ways that the MODIS winds can affect the zonal wave propagation speed: a change in the mean zonal wind or a change in the wavelength. To effect a 1 m s^{-1} change in the wave speed (which is equivalent to a 430 km displacement in position over 5 days) the mean zonal wind would need to change by 1 m s^{-1} , the wavelength by about 500 km, or some combination. To quantify this, the change

in wave propagation speed will be measured to infer what changes are needed to the mean zonal wind and/or the wavelength to account for the observed difference in the forecast wave position.

4.5.2 Ageostrophic wind

Radiance measurements from satellite sounding instruments are assimilated in models resulting in an improved depiction of the vertical temperature and moisture structure, with the thermal wind equation as a balance constraint. What additional information do the MODIS winds provide that result in an additional improvement in forecasts? Since the thermal wind equation is based on the geostrophic wind profile, perhaps the MODIS winds provide an ageostrophic component since they are a measure of the total wind. The ageostrophic component of the wind is essentially the acceleration part of the wind, affecting the development and movement of baroclinic waves.

The geostrophic wind is only dependent on the gradient of the geopotential height field:

$$\vec{V}_g \equiv f_0^{-1} \hat{k} \times \nabla_p \Phi \quad (10)$$

where f_0 is the constant Coriolis parameter.

The ageostrophic wind is the total derivative (D/Dt) of the geostrophic wind, which can be separated into a local time derivative and advection (Holton 1992):

$$\vec{V}_a = \frac{1}{f_0} \hat{k} \times \frac{D_g \vec{V}_g}{Dt} = \frac{1}{f_0} \left[\hat{k} \times \frac{\partial \vec{V}_g}{\partial t} + \hat{k} \times (\vec{V}_g \cdot \nabla) \vec{V}_g \right] \quad (11)$$

The first term is the isallobaric wind; the second term is the inertial advective component of the ageostrophic wind. In the mid-troposphere the isallobaric wind is much smaller than the

advective term by about an order of magnitude (because of the higher wind speeds aloft), so it will be ignored. Therefore:

$$\vec{V}_a \approx \vec{V}_{adv} = \frac{1}{f_0} [\hat{k} \times (\vec{V}_g \cdot \nabla) \vec{V}_g] \quad (12)$$

By applying $\nabla \cdot$ to both sides of the equation, it can be shown that (Martin 2006) (see *Appendix C: Derive Ageostrophic Wind Relation to Vorticity Advection*):

$$\nabla \cdot \vec{V}_a = -\frac{1}{f_0} \vec{V}_g \cdot \nabla \zeta_g \quad (13)$$

which states that the divergence of the advective component of the ageostrophic wind is related to the geostrophic advection of the geostrophic relative vorticity (ζ_g). According to quasi-geostrophic theory, “advection of relative vorticity tends to move the vorticity pattern and hence the troughs and ridges” downstream (Holton 1992), therefore a change in the ageostrophic wind will affect the speed of the baroclinic waves. A qualitative assessment will be done on how differences in the divergence of the ageostrophic wind in the analysis affect the wave propagation speed in forecasts.

5. Analysis

Section 3.2.2 *Measuring the impact on forecasts* presented two ways that the ACC scores are used to quantify model impact: monthly means and time series. Also, an example was presented on using patterns in total precipitation to determine the model impact. In this study, the following methods are used to analyze the differences in the model runs to better explain dynamical reasons for what is observed:

1. Analysis impact: Assimilation effects: This will show differences that are related to the assimilation system, not related to atmosphere dynamics.
2. Forecast impact: Wavelength: Examine the ACC differences based on wavelength regimes (from planetary to synoptic scale) to determine if there is a preferred scale that the MODIS winds impact.
3. Analysis impact: Geographic: A cross-section of 500 hPa height differences along a latitude circle at the analysis times are used to determine where the MODIS had the largest impact, geographically. This is quantified by computing the power spectra in geographic space.
4. Analysis and forecast: Thickness difference: Investigate patterns in the 1000-500 hPa thickness difference for the analysis and forecasts. Determine if a pattern or signature emerges in later forecast times, when the MODIS winds impact is the greatest. Since thickness is dependent on mass and temperature through the hypsometric equation, the impact of the MODIS winds and the AMSU radiances can also be inter-compared.
5. Analysis and forecast: Ageostrophic wind: Compute the ageostrophic wind differences between the MODIS wind and control runs. Qualitatively examine how the propagation of these anomalies is reflected in the forecast height field.

6. Forecast impact: Phase shift in waves: Compute the correlation coefficient of the 500 hPa heights along a latitude circle for the 120-hour forecast time to determine the phase shift of the waves between the two model runs. This is computed for the entire latitude circle and for specific waves.
7. Forecast impact: Tropical cyclone positions: Determine the position of the tropical cyclones in the 120-hour forecasts vs. the actual location. Show how a change in the speed of mid-latitude systems may affect these forecast positions.

The primary emphasis of this work is to investigate *dynamical reasons* to explain the positive impact that the MODIS winds have on forecasts. However, there are *mechanisms inherent in the assimilation* and the model that will also impact the forecast when new data are introduced. Unfortunately, no satisfactory way was found to separate these two effects in the datasets provided.

It was found that the successful interpretation of difference fields (between the MODIS winds run and the control) is parameter dependent. For example, wind speed differences exhibit large variations in the analysis without much correlation to dynamic features, thereby making it difficult to associate with changing forecast wave positions. While 1000-500 hPa thickness differences in the analysis were small, they increased in magnitude in the forecasts, traveling along with specific wave features.

5.1 Analysis impact: Assimilation effects

Spectral interpolation and dynamic bias correction effects are shown in Figure 17, when the MODIS data is first introduced at the beginning of the experiment. This figure depicts analysis differences in the 800 hPa winds only six hours after the first assimilation of the MODIS winds. It is not physically possible for upper-tropospheric polar winds, poleward of

65° latitude, to have an impact on lower-tropospheric winds in the tropics in only six hours. Therefore, it is deduced that the assimilation system spread the influence of this new data to data void areas, for example the oceanic regions, while the winds over the continents are mostly unchanged (where rawinsondes are weighted higher than satellite-derived winds). Figure 18 is six days into the experiment. The differences are now larger in magnitude, but are still primarily over the oceans, although some significant differences are noted over the African continent in the vicinity of the Intertropical Convergence Zone (ITCZ).

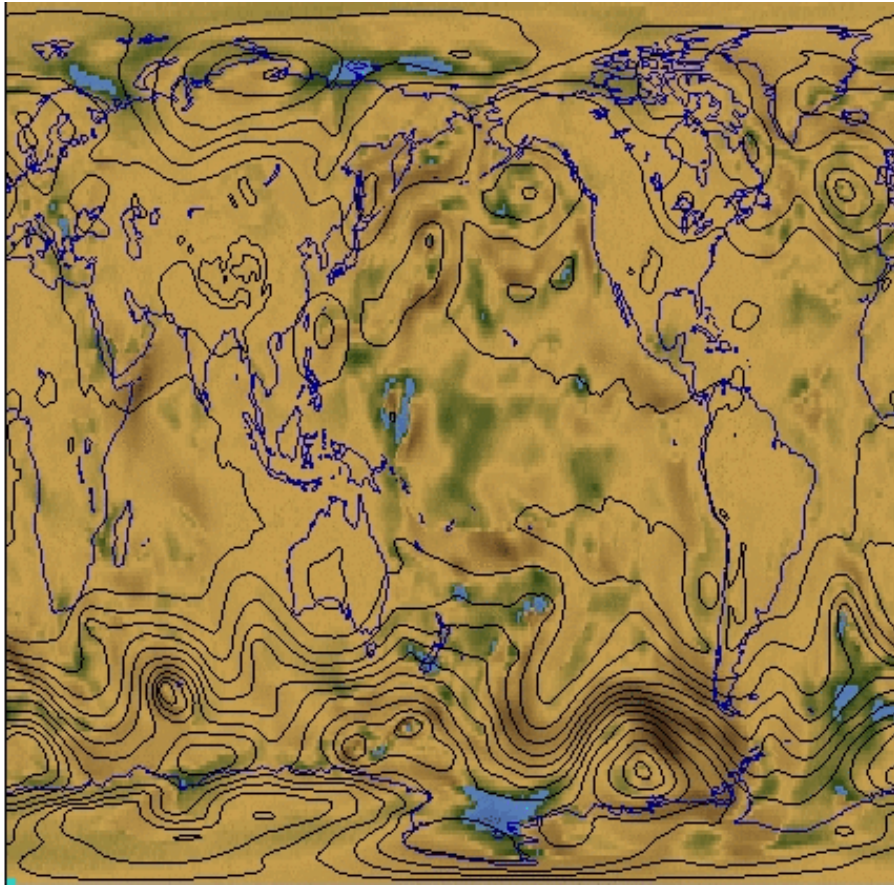


Figure 17: Wind speed difference between the model run with and without the MODIS winds at 800 hPa. This is 6 hours into the experiment. The yellow is close to zero difference; the brown to black is up to a +7 m/s difference; the green to blue is from -1 to -6 m/s difference. This is an analysis grid, not a forecast.

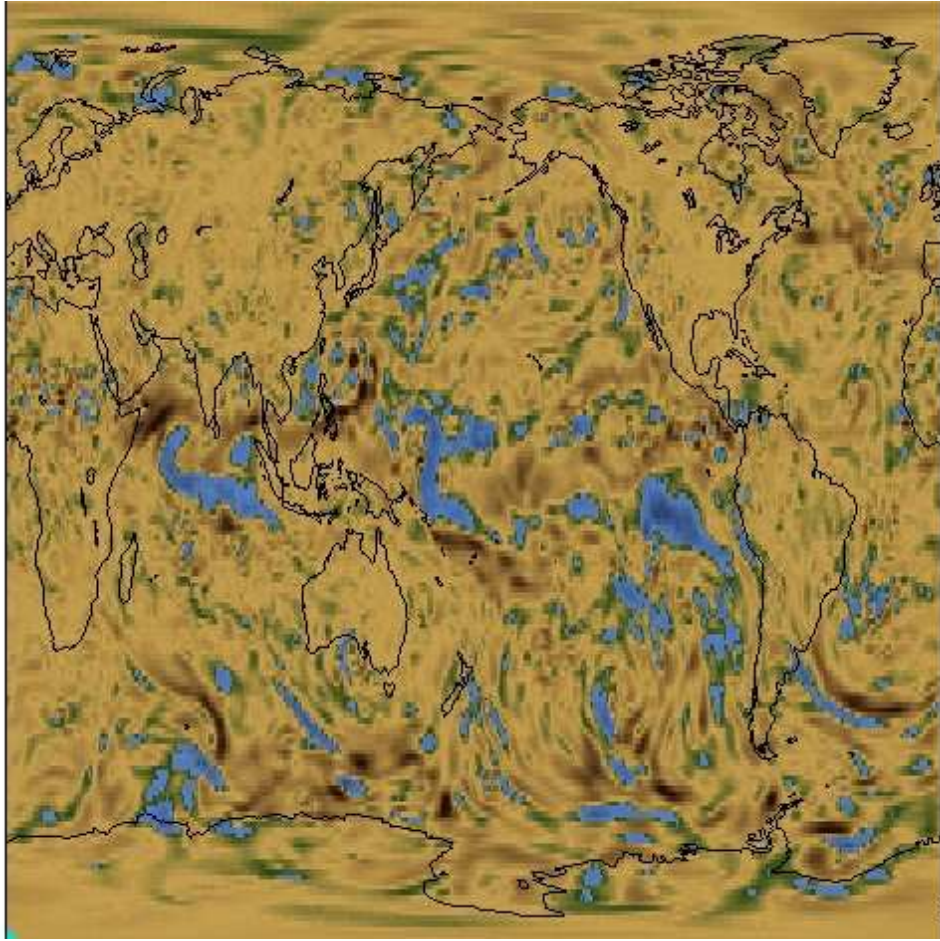


Figure 18: Wind speed difference between the model run with and without the MODIS winds at 800 hPa. This is 6 days into the experiment. Same color scheme as Figure 17. This is an analysis grid, not a forecast.

5.2 Forecast impact: Wavelength

Most NWP centers use the anomaly correlation to evaluate how an experimental forecast performed compared to a control. Examples of the overall ACC scores were shown in Figure 13 and Figure 14. For this experiment, the ACC is also computed in wavelength bins, which gives an indication of the horizontal scale that the MODIS winds impact the greatest. Figure 19 depicts the 500 hPa 120-hour forecast ACC differences by wavenumber range for the

entire 39-day experiment. Positive differences reflect an improvement in the forecast due to the MODIS winds. The largest change in the ACC due to the addition of the MODIS winds is in the wavenumber range from 10-20, synoptic scale waves (wavelengths of approximately 1500 to 3000 km in mid-latitudes). This was the case 67% of the time. The MODIS winds had the largest effect on long waves (4-9 wavenumbers) 12% of the time and very long planetary wave (1-3 wavenumbers) 21% of the time. Since the MODIS winds are retrieved at meso- to synoptic-scale resolution, having the primary impact in the 10-20 wavenumber bin is expected.

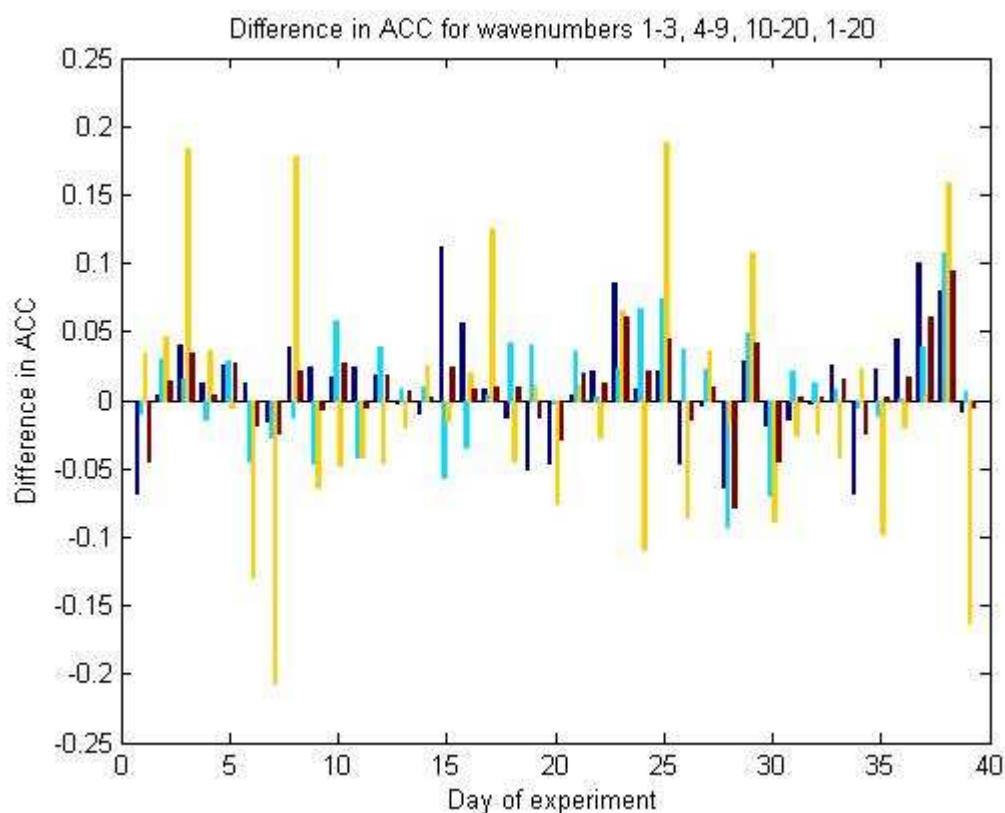


Figure 19: Difference in ACC between the MODIS winds and control model run at 500 hPa for the 120-hour forecast in the northern hemisphere for the entire experiment: 11 August to 22 September 2004. The colors represent ranges of wavenumbers: blue 1-3, cyan 4-9, yellow 10-20, red 1-20.

This figure also gives an unsettling impression that the addition of the MODIS winds results in about an equivalent number of positive and negative impact cases for the synoptic-scale waves (yellow bars). This was not investigated any further, except to note that even though the impact varies widely at these wavenumbers, the overall ACC difference (red bars) illustrates that the experiment including the MODIS winds resulted in a positive or neutral impact 70% of the days.

5.3 Analysis impact: Geographic

To determine where (geographically) the impact of the MODIS winds is largest in the analyses, a latitude slice at 50°N for the 500 hPa height differences between the MODIS and control run is analyzed. This latitude belt was chosen because the jet streams were generally centered there during early and mid-September 2004, the time frame of the five cases.

An example of this latitude cross-section is shown in Figure 20 for the 11 September 2004 case. The differences in the analyses range from approximately -6 to +6 gpm. These height differences will be largest where the assimilation system adjusts the mass to bring the model atmospheric state into balance. In examining the five cases qualitatively, there were four longitudes where large differences primarily occurred. A large difference is defined as +/- 4 gpm from the normalized mean. These areas are noted, along with the local synoptic flow conditions, in Table 8. The longitudes represent a band +/-20 degrees wide where there was at least one case of a large difference in the 500 hPa analyses.

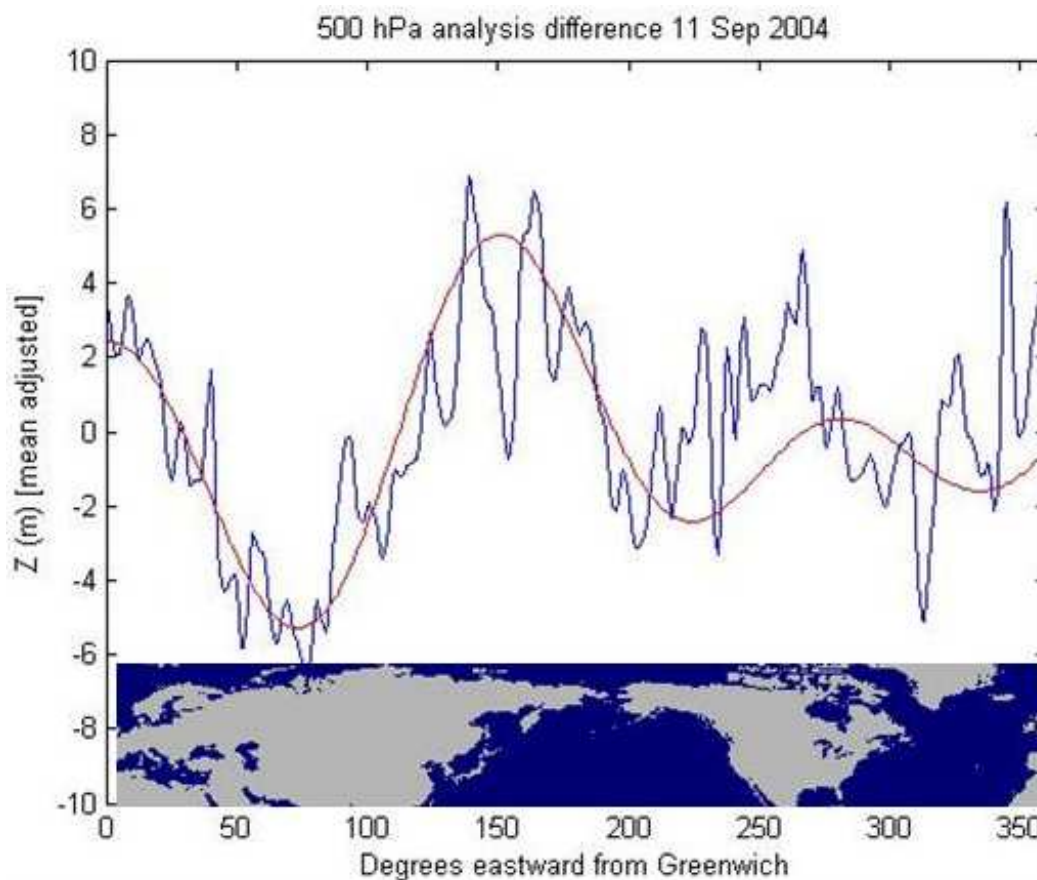


Figure 20: The difference in the analysis height field between the MODIS run and the control for 11 September 2004 for a latitude circle at 50°N. The blue line is the mean adjusted difference, in geopotential meters. The red line represents the signal from the three highest frequencies from the power spectrum (see Figure 21).

Table 8: Large difference in analyses for a latitude cross-section of heights. X indicates a large difference with a subscript indicating the type of flow: T – trough, R – ridge, Z – zonal flow.

Date\Longitude	50°E W. Asia	180°E N. Pacific	90°W Mid USA	30°W N. Atlantic
06 Sep 2004	T	X _T	X _T	X _T
07 Sep 2004	X _T	X _Z	T	X _T
11 Sep 2004	X _T	X _T	X _Z	X _T
12 Sep 2004	X _T	X _T	Z	X _T
17 Sep 2004	R	X _T	Z	X _T

A T,R, or Z in the table without the X means the difference is small. There are other longitudes with troughs (usually weak) or jets where the difference in the analyses is also small.

The table shows that each of the days had a large difference in the N. Pacific and N. Atlantic, consistent with Figure 20. Moreover, 9 out of 10 times it was in a region with a trough or closed low. This is a region of very little conventional data and is very dynamic (off the east coast of the continents). Three out of four cases of a trough over West Asia were areas of large differences, where the troughs were deep. This is not a data void region as there are many rawinsondes in Russia. Over the central USA, only two out of the five days had a significant difference: one zonal; one trough. The troughs were much less intense than the ones over West Asia. This is not a data void region.

The difference in longitude between the three observed areas of largest height differences is subjectively determined to be 130° and 150° . This can be quantified by computing a power spectrum derived from the Fast Fourier Transform (FFT). The input into the FFT is the difference in the 500 hPa heights between the analysis including the MODIS winds and the control analysis at 1 degree intervals (the output grid resolution) along 50°N latitude. The power spectrum will show if there is a preferred frequency in the geographic location of the large differences. The amplitude of the power spectrum gives an indication of how large the difference is at that longitude.

Figure 21 is the power spectrum for the height differences from Figure 20. The frequency is relative to 360° , so the wavelength is simply $360/\text{frequency}$. The three largest amplitudes are labeled with their corresponding wavelengths: 255° , 170° , and 127.5° . That means the largest impact of the MODIS winds occur at those longitude spacings. The

amplitudes of frequencies greater than 5 (wavelengths less than 72°) were generally small in all five case studies and did not contribute significantly to the overall wave pattern.

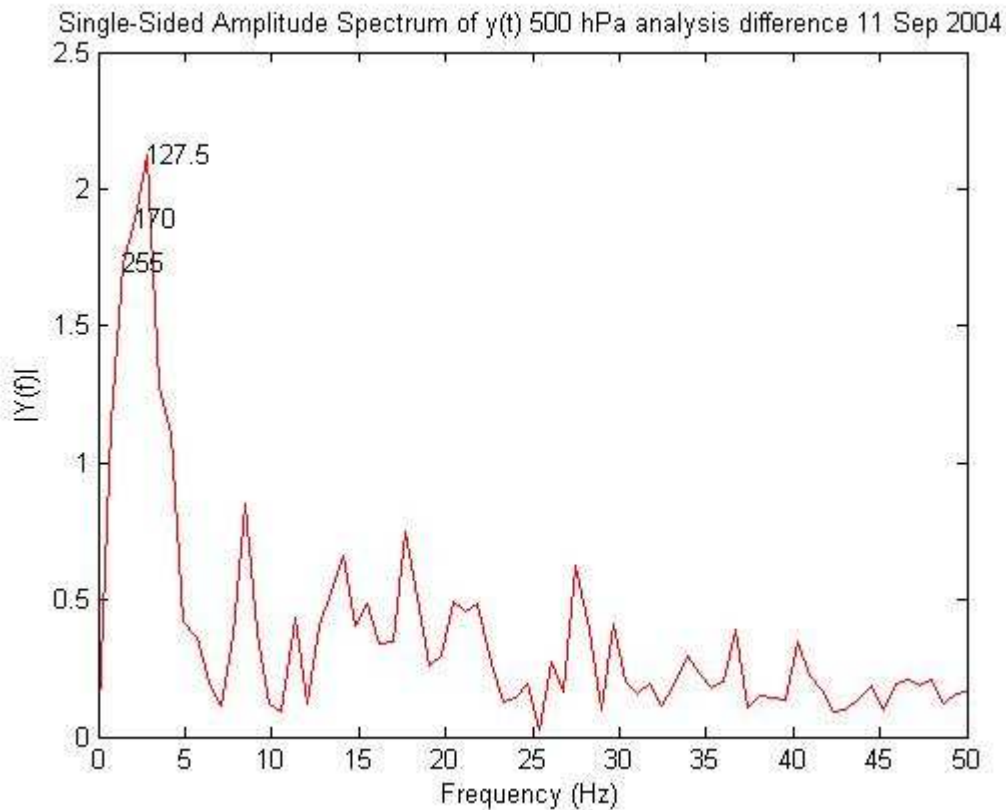


Figure 21: The power spectrum of the height field analysis difference in longitude space (from Figure 20). The frequency is relative to a 360 degree cycle. The highest amplitude frequencies are labeled in wavelength (255° , 170° , 127.5°) in the graph.

The power spectra for these 5 cases show wavelengths of 128° or 170° have one of the highest three amplitudes on all days, with both frequencies on 3 out of 5 days. As noted before, there is about a ± 20 degree variation in the longitude position for the height differences, so the power spectra quantitatively confirms the longitude spacing of the significant difference areas: west Asia, the North Pacific Ocean, and the North Atlantic Ocean.

5.4 Analysis and forecast: Thickness difference

The ACC provides a good measure of the overall impact that the MODIS winds had on the forecast on a hemispheric scale, but it doesn't give an indication where the improvements are in terms of geographic location, pressure levels, meteorological parameters, and flow regimes. This type of analysis is needed to better understand and explain how the polar winds positively affect forecasts into low-latitudes. After experimenting with several output model parameters, differences in the 1000-500 hPa thicknesses between the MODIS and control runs were chosen.

The hypsometric equation (Holton 1992) relates temperature and mass: the distance between two geopotential height fields (Φ_1, Φ_0) on isobaric levels (p_0, p_1), is dependent on the layer mean temperature ($\langle T \rangle$):

$$\Phi_1 - \Phi_0 = R\langle T \rangle \ln(p_0/p_1) \quad (14)$$

where R is the gas constant for dry air. When winds are assimilated into a numerical model system, an adjustment to the mass field takes place. Basically, this is because the gradient of the geopotential height (or mass) defines the wind field. Also, this change in the geopotential height requires an adjustment to the temperature structure, for the thermal wind relationship to hold. The thermal wind is simply the gradient of the thickness (Holton 1992):

$$\vec{V}_T = \frac{1}{f} \hat{k} \times \nabla(\Phi_1 - \Phi_0) \quad (15)$$

The geostrophic (Eq. 10), hypsometric (Eq. 14), and the thermal wind (Eq. 15) equations bring together the basic atmospheric properties of wind, mass, and temperature through a single diagnostic parameter of thickness. Thickness differences provide a similar way to examine changes in the mass structure (due to the MODIS winds assimilation) in the primary

experiment and the thermal structure (due to AMSU radiance assimilation) in the secondary experiment. By examining differences in thickness, the impact due to winds (MODIS polar winds) or temperature (AMSU radiances) can be inter-compared. The goal in this part of the analysis is determine how the MODIS winds affect the analyses forecasts, not necessarily to quantify how much better or worse the forecast is as the ACC gives a measure of that.

A set of rules were developed for interpreting the thickness difference fields to characterize how the addition of different data affects the speed of troughs and ridges, and their change in amplitude. The color of the change indicates increasing thickness (red) and decreasing thickness (blue) from the addition of the MODIS winds. Specifically for the northern hemisphere, the change in thickness in the westerlies can be interpreted, thus:

1. Red feature centered in a trough: weaker trough
2. Red feature centered in a ridge: stronger ridge
3. Blue feature centered in a trough: stronger trough
4. Blue feature centered in a ridge: weaker ridge
5. Red feature west of ridge (east of trough): wave speed decreased
6. Red feature east of ridge (west of trough): wave speed increased
7. Blue feature west of ridge (east of trough): wave speed increased
8. Blue feature east of ridge (west of trough): wave speed decreased.

In general terms, the position of the differences can be interpreted as: when a difference feature is centered on a ridge or trough, it indicates a change in the amplitude of the wave. If the difference feature is displaced from a ridge or trough, it indicates a change in wave phase speed. These rules will be designated R1 to R8 in the following case study discussions.

The five cases are analyzed in the following sections. The above rules are applied only over the northern hemisphere, primarily in the jet stream region at about 50°N latitude.

Tables of the ACC values by wavenumber (see *5.2 Forecast impact: Wavelength*) are included in each section. Also, the impact on the MODIS winds in the NOGAPS forecasts and the AMSU radiances in the GFS forecasts are discussed.

5.4.1 Case 1: 06 September 2004

The overall ACC for the two different model runs is essentially the same at about 0.76 for the 120-hour forecast over the northern hemisphere (Table 9). The most improvement by the MODIS winds is in the 10-20 wavenumber range.

Table 9: 06 September 2004 ACC values for the Northern Hemisphere, 120-hour forecast by wavenumber range.

Wavenumbers:	1-3	4-9	10-20	1-20
MODIS run	0.776	0.798	0.324	0.765
Control run	0.780	0.776	0.288	0.757

Figure 22 shows the difference in thickness for the analysis on 06 September 2004. This is a good example of the 3-wave pattern discussed in section 5.3 *Analysis impact: Geographic*. The most intense cyclonic systems are over western Russia, the North Pacific, and the North Atlantic. The two oceanic regions are areas where the thickness differences are significant, as evident by the blue features.

In the North Atlantic, the blue region is to the east of the trough which indicates that the MODIS winds have this trough placed farther to the east than the control (R7). In the intermediate forecasts (not shown) prior to the 72-hour forecast, the blue difference feature rotates one time around the low before kicking out with the wave east of Greenland (Figure 23). Now the blue/red difference couplet indicates the wave pattern has slowed (R5, R8), displaced to the west. By 120 hours (Figure 24), this wave has become part of the cyclone north of the strong ridge over Europe. The other significant difference area in the analysis is

over the North Pacific. This blue feature can be traced to the short wave off the west coast of the US by the 120-hour forecast. Here the blue feature is centered in the trough indicating that the MODIS winds have made the trough deeper (R3).

The thickness difference from the analysis through the 120-hour forecast show how small differences in just a few specific areas are magnified and eventually affect the flow throughout the entire jet stream and northward. Also, the example in the North Atlantic shows how a wave initially positioned farther east in the analysis is then subsequently slowed down in the forecast.

A difference in the 120-hour forecast in the lower-latitudes of the Atlantic is associated with easterlies south of the subtropical high. For example, the blue/red couplet in the west-central Atlantic is due to a westward shift of a mid-level thickness trough in the MODIS winds 120-hour forecast. More detailed analysis of changes in low-latitudes will be examined in tropical cyclone situations on the other case study days.

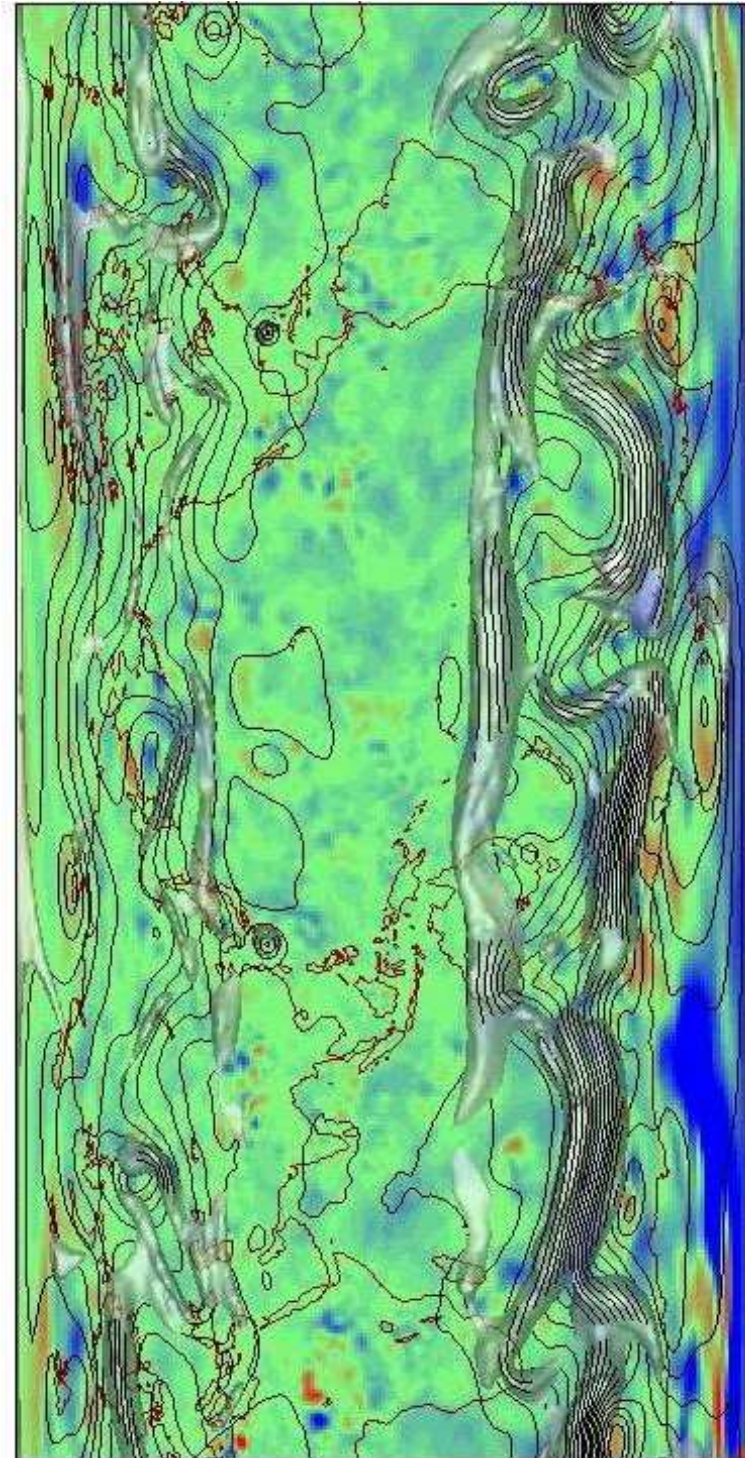


Figure 22: Thickness difference, with and without MODIS winds for the GFS analysis on 06 September 2004 at 0000 GMT. The color range from blue to red denotes a range of -30 to +30 gpm difference. Near zero difference is in green. The 30 m s^{-1} wind speed, representing the jet stream, is in transparent white.

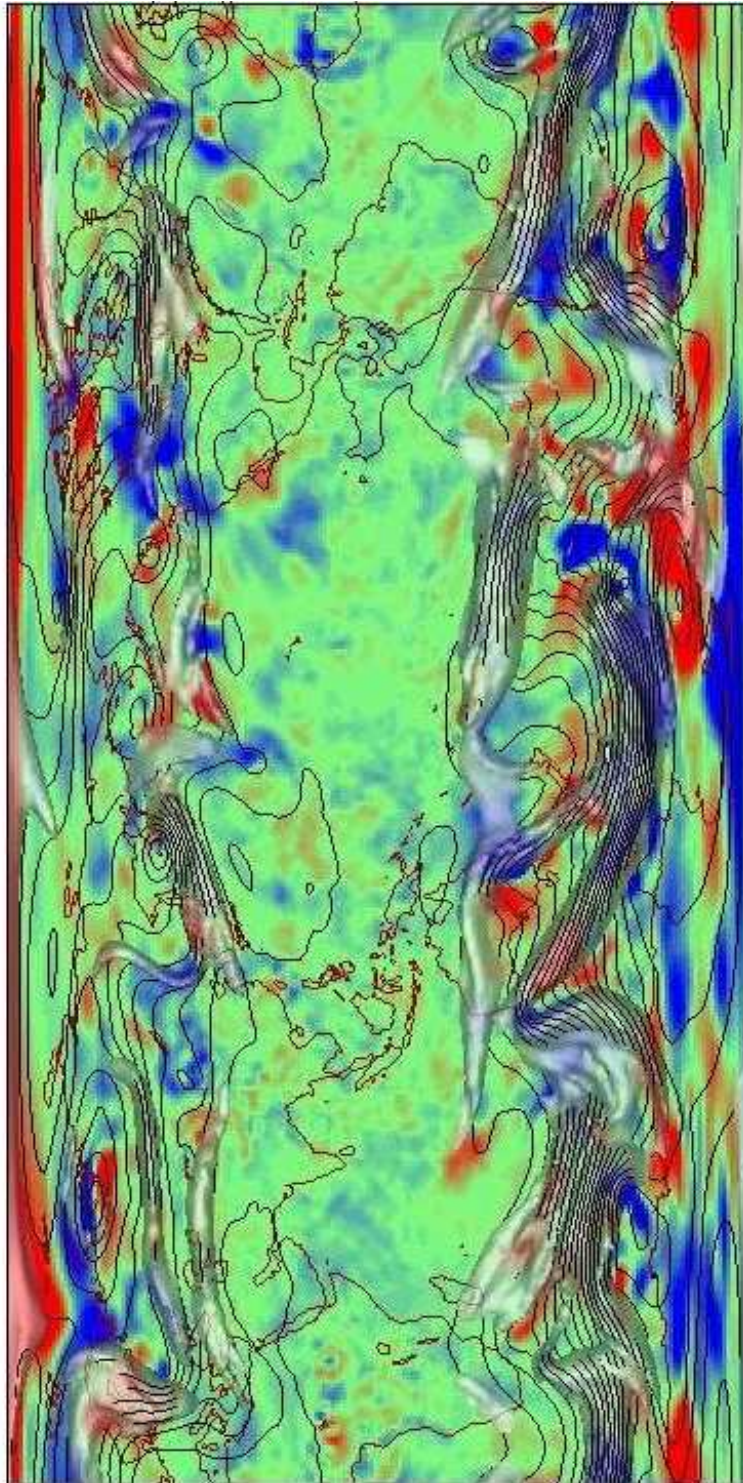


Figure 23: Thickness difference, with and without MODIS winds for the GFS 72-hour forecast from 06 September 2004 at 0000 GMT model run. Same color scheme as Figure 22.

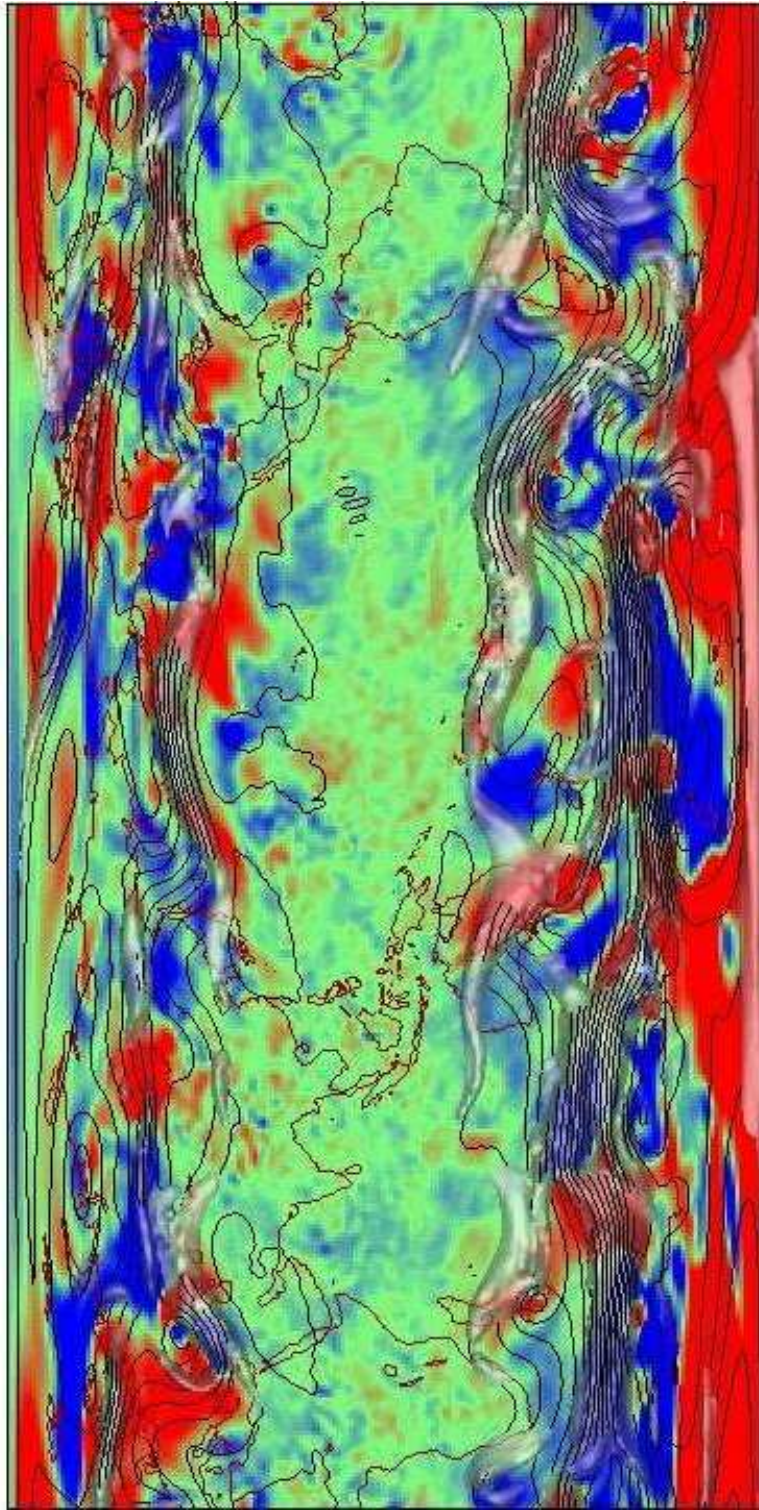


Figure 24: Thickness difference, with and without MODIS winds for the GFS 120-hour forecast from 06 September 2004 at 0000 GMT model run. Same color scheme as Figure 22.

5.4.2 Case 2: 07 September 2004

This case is a forecast run beginning 24 hours later than Case 1 and the control has a much better ACC, 0.78 vs. 0.71, where in Case 1 it was neutral. In terms of impact by different wavenumbers (Table 10) the control was much better than the MODIS winds run except for the synoptic-scale waves when the ACC is about the same (0.228 vs. 0.211).

Table 10: 07 September 2004 ACC values for the Northern Hemisphere, 120-hour forecast by wavenumber range.

Wavenumbers:	1-3	4-9	10-20	1-20
MODIS run	0.780	0.643	0.211	0.705
Control run	0.844	0.736	0.228	0.783

The 3-wave trough system is still evident on this day (Figure 25) as it was on the previous day (Figure 22), but the impact of the MODIS winds on the analysis isn't as significant: the blue regions are not as large in magnitude. By the 120-hour forecast (Figure 26) there are large thickness differences throughout the northern hemisphere, seemingly similar to the previous day (Figure 24). However, based on the ACC, the addition of the MODIS winds has negatively impacted the forecast compared to the control. What is different in this case? Closer inspection of these two figures for the 120-hour forecast reveals that there are significant differences in how the waves are affected. Two of the most striking examples are:

1. The ridge located over eastern Europe was red now it's blue. This indicates that the forecast tendency of the ridge due to the MODIS winds has gone from being stronger (R2) to weaker (R4).
2. The ridge over eastern Canada was blue now it's red. This is the opposite tendency from the first example.

It's difficult to determine what happened over the 24 hour period from 06 September and 07 September 2004 that would account for the MODIS wind impact going from neutral to worse than the control. Moreover, it is not known if the reverse tendency illustrated in the two examples is relevant to the change in forecast skill.

Since the ACC values for the control are comparable on the two days (0.757 and 0.783), the issue may be with the assimilation of the MODIS winds or the winds themselves.

Some potential problems:

1. There are additional assimilation and model runs at 0600, 1200, and 1800 GMT each day. No information or statistics are available from those intermediate times, except for the model analysis grids. A cursory view of the thickness difference for those times did not indicate that the impact due to the MODIS winds was different than what was typically observed throughout the experiment.
2. The ACC values for the intermediate assimilation times were not available, so a trend or significant change of the ACC at a specific time cannot be determined. This information could be useful in diagnosing a cause for the degraded forecast.
3. The best forecasts come from data that are not only accurate, but also continuously available to the assimilation system⁵. It is not known what winds were actually used or if there were any interruptions in the availability of the MODIS winds during the experiment. Table 7 indicates there were 40% fewer MODIS winds available on this day compared to the previous day. It is not known how fluctuations in the volume of winds affects the assimilation or forecasts.

⁵ Jung, personal communication, 05 May 2005.

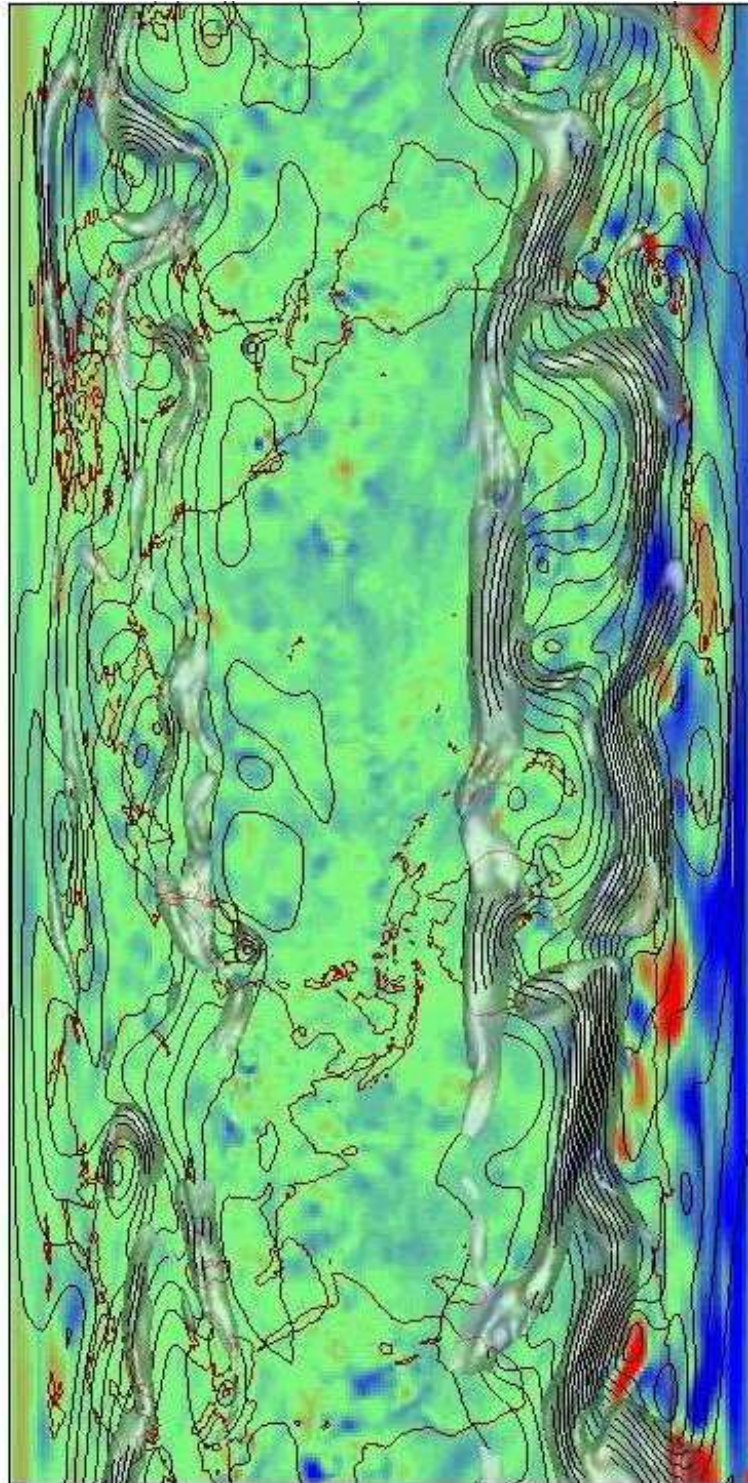


Figure 25: Thickness difference, with and without MODIS winds for the GFS analysis on 07 September 2004 at 0000 GMT model run. Same color scheme as Figure 22.

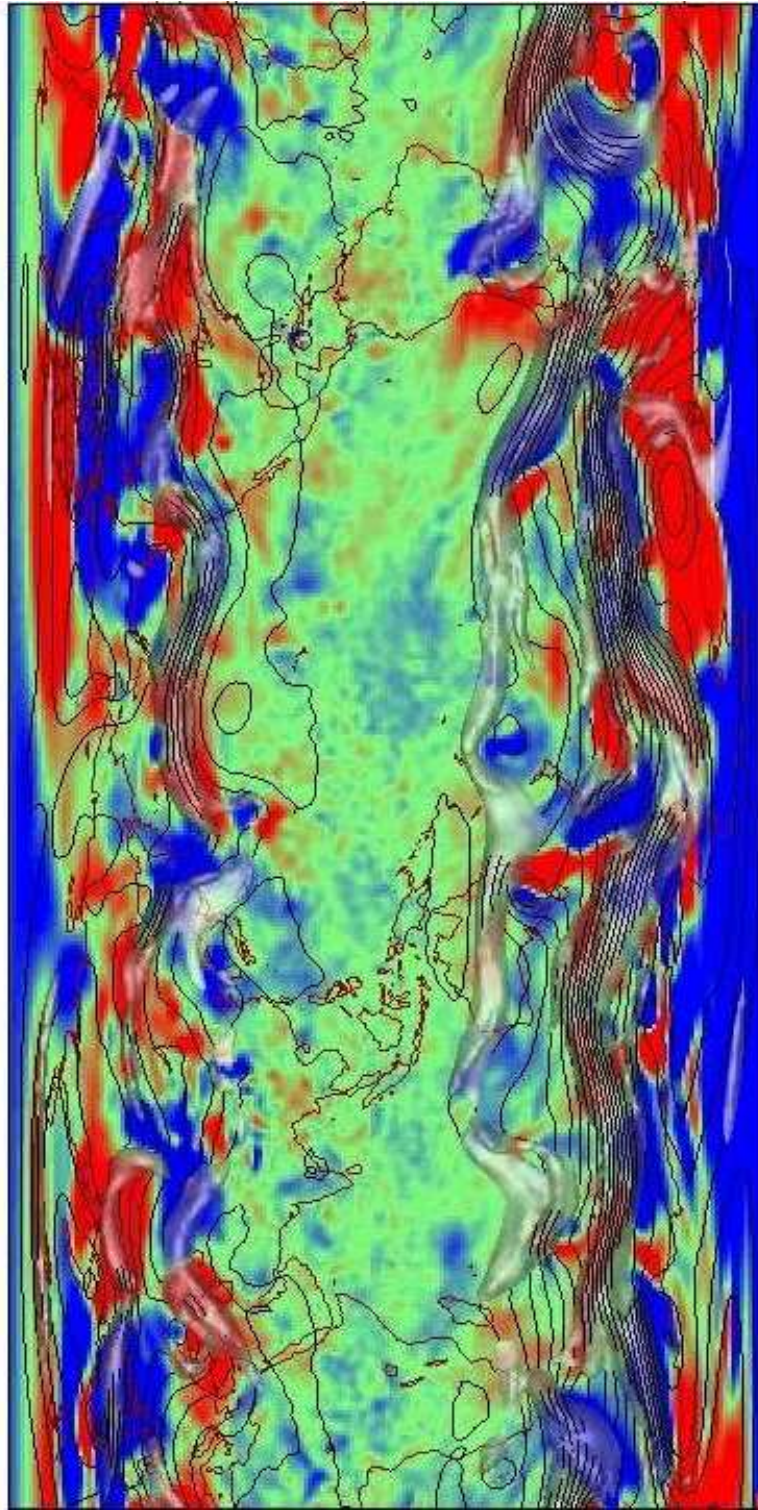


Figure 26: Thickness difference, with and without MODIS winds for the GFS 120-hour forecast from 07 September 2004 at 0000 GMT model run. Same color scheme as Figure 22.

5.4.3 Case 3: 11 September 2004

The ACC for the two different model runs is essentially the same at all wavenumbers for the 120-hour forecast over the northern hemisphere (Table 11) on this day, but the significance of this case is the presence of Hurricane Ivan (south of Cuba in Figure 27).

Table 11: 11 September 2004 ACC values for the Northern Hemisphere, 120-hour forecast by wavenumber range.

Wavenumbers:	1-3	4-9	10-20	1-20
MODIS run	0.891	0.777	0.459	0.822
Control run	0.894	0.765	0.483	0.820

The impact in the analysis is generally small, but with two regions where it is significant: in the jet stream in the West and East Pacific. By the 72-hour forecast (Figure 28), there is evidence that the trough/ridge system extending from the southwest US to the upper Great Lakes region is slowing (R8 for trough; R5 for ridge). In the 120-hour forecast, the blue is now centered in the trough indicating it is deeper (R3) and the ridge is still held (R5) back compared to the control. The slowing of this pattern is reflected to the south where Hurricane Ivan is positioned farther west: the red feature to the west of the blue near South Carolina (Figure 29).

Hurricane Ivan began its life as a tropical cyclone in early September 2004. It moved west-northwestward for several days steered by the winds of the subtropical ridge to its north. On 11 September 2004 Ivan was near Jamaica, just south of eastern Cuba (Figure 27). The three to five-day forecast from this date brings the hurricane to landfall in the Gulf coast area of the US. The global models at this time “prematurely eroded the large and

strong subtropical ridge to the north of Ivan that extended well westward across the Bahamas, Florida, and into the Gulf of Mexico.” (Stewart 2004) This tendency resulted in Ivan being forecasted to take a more easterly track across Florida, and in some forecasts, east of Florida. The model run including the MODIS winds held the subtropical ridge more westward (note the 5880 contour in the eastern Atlantic Ocean in Figure 30) along with the jet stream ridge to the north (red shading in the Great Lakes region in Figure 29) compared to the control. This resulted in a somewhat improved forecast track for Hurricane Ivan in the 96-hour forecast, although it was still too far east: over Florida (MODIS: 29.7°N 81.8°W; Control: 29.6°N 81.0°W) instead of the central Gulf of Mexico at 24.7°N 87.0°W (Figure 30). An error of 756 km and 805 km, respectively.

The 120-hour forecast verifying at 0000 GMT on 16 September 2004 had the same tendency (Figure 31). Ivan was forecasted to be over eastern South Carolina (MODIS: 33.7°N 80.4°W; Control 33.8°N 79.2°W), but the actual position was at 28.9°N 88.2°W just south of the Louisiana/Mississippi border, as a 110 kt tropical cyclone. The location error was 915 km (MODIS) and 1014 km (Control). Using the technique described in section 5.6 *Forecast impact: Phase shift in waves*, the displacement of the ridge from 40°W to 90°W longitude, along 50°N latitude) was 109 km in the 120-hour forecast. This value agrees well with the 99 km improvement in the hurricane position. Although the long range forecast was poor in this case, the westward shift by approximately the same amount of the jet stream ridge and subtropical high kept Hurricane Ivan farther west.

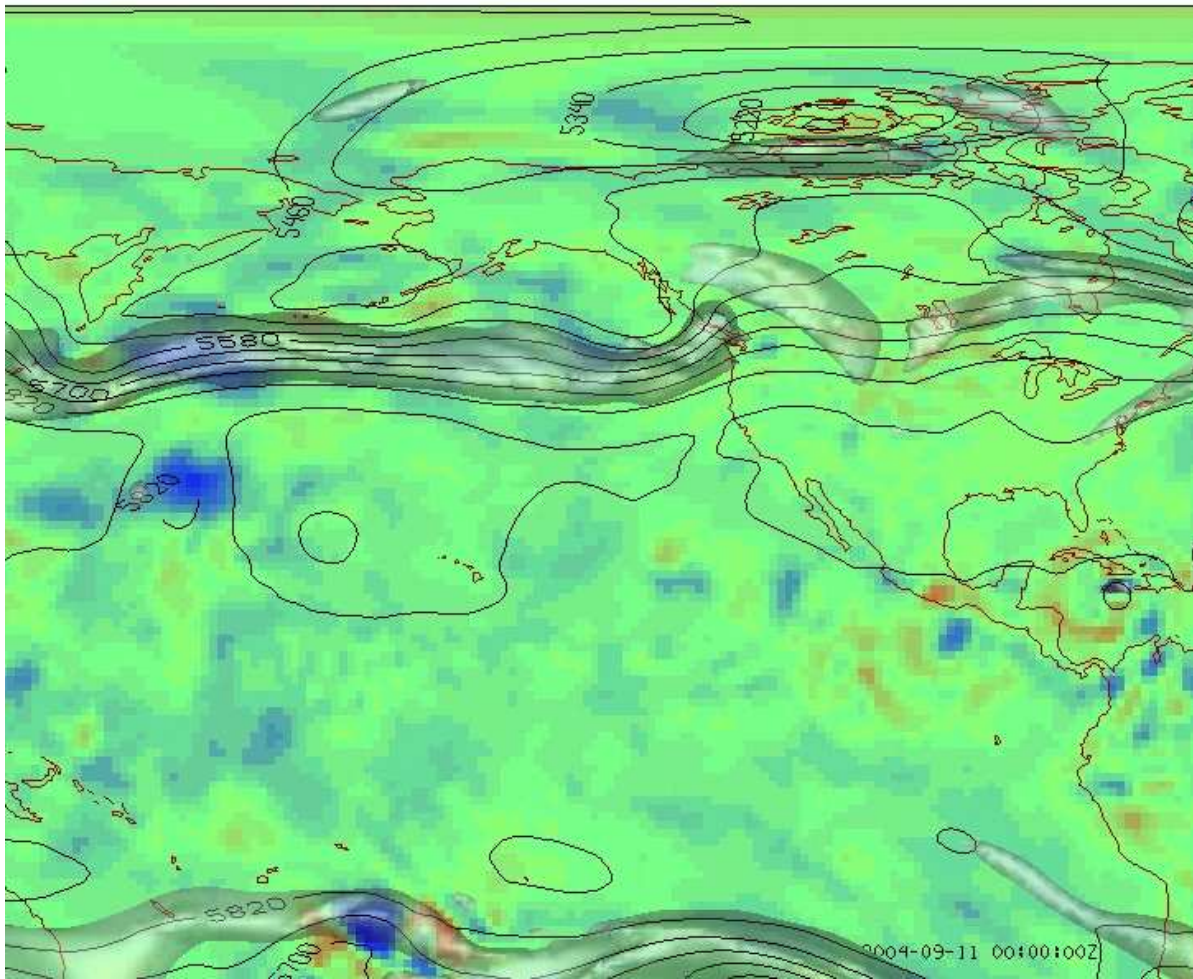


Figure 27: GFS analysis differences of the 1000-500 hPa field, with and without the MODIS winds for 11 September 2004. Same contours and color scheme as Figure 22.

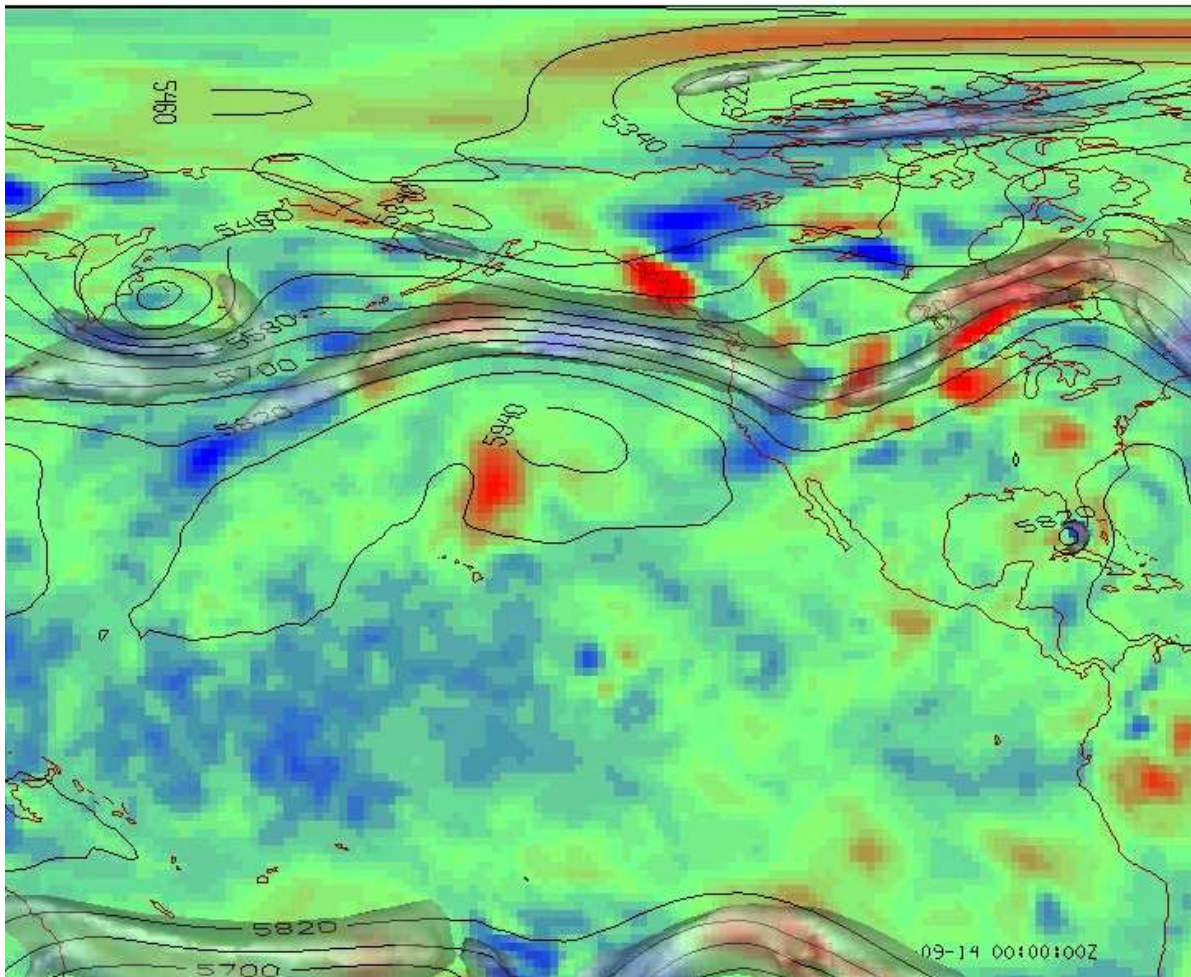


Figure 28: 72-hour GFS forecast differences of the 1000-500 hPa field, with and without the MODIS winds. Valid 0000 GMT on 14 September 2004. Same contours and color scheme as Figure 22.

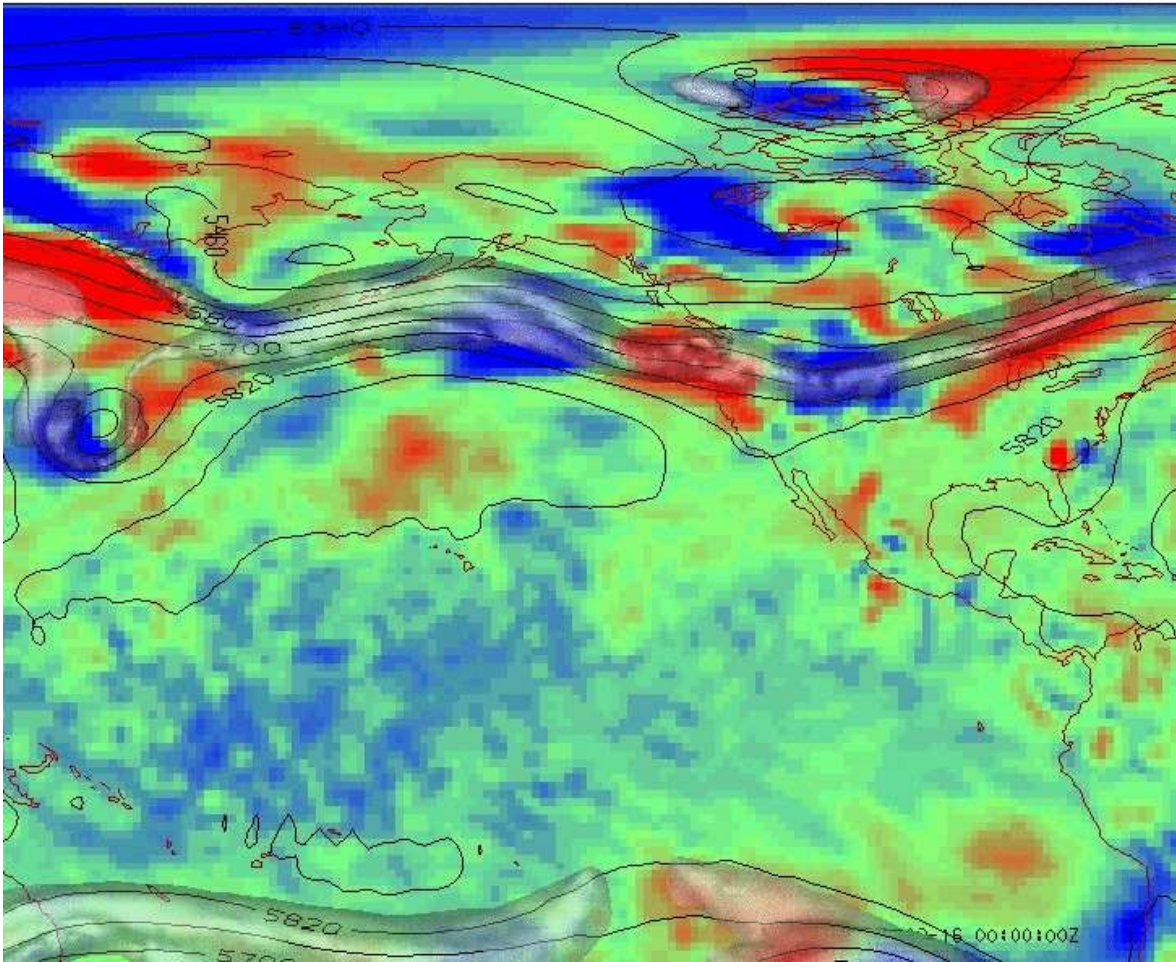


Figure 29: 120-hour GFS forecast differences of the 1000-500 hPa field, with and without the MODIS winds. Valid 0000 GMT on 16 September 2004. Same contours and color scheme as Figure 22.

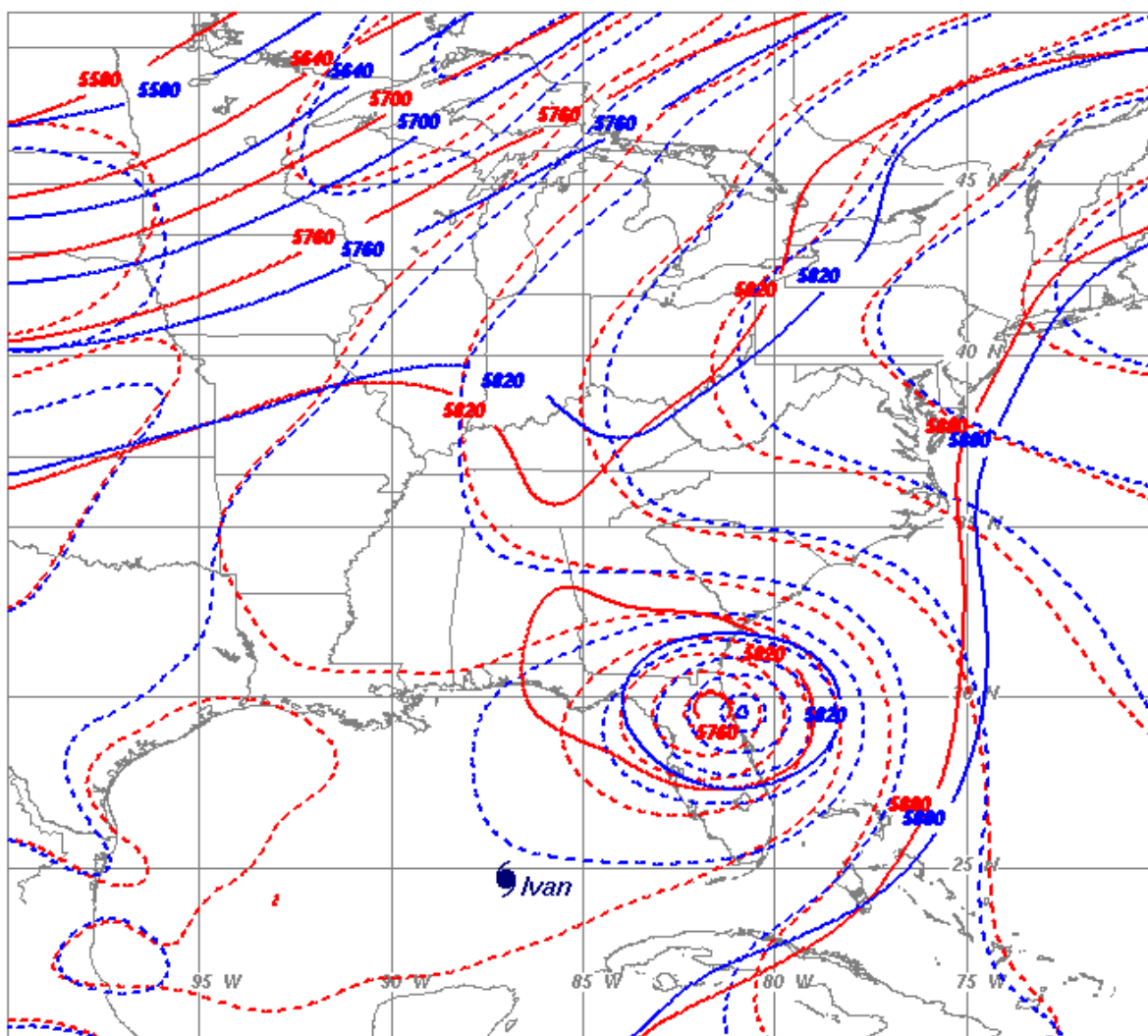


Figure 30: Hurricane Ivan over the southeast US for the 96-hour forecast from 0000 GMT on 11 September 2004. Solid red contours are the 500 hPa heights with MODIS winds; dashed red are 1000 hPa heights. Solid blue are 500 hPa heights of the control; dashed blue are 1000 hPa heights. Actual position at the forecast time of hurricane Ivan is shown with the hurricane symbol.

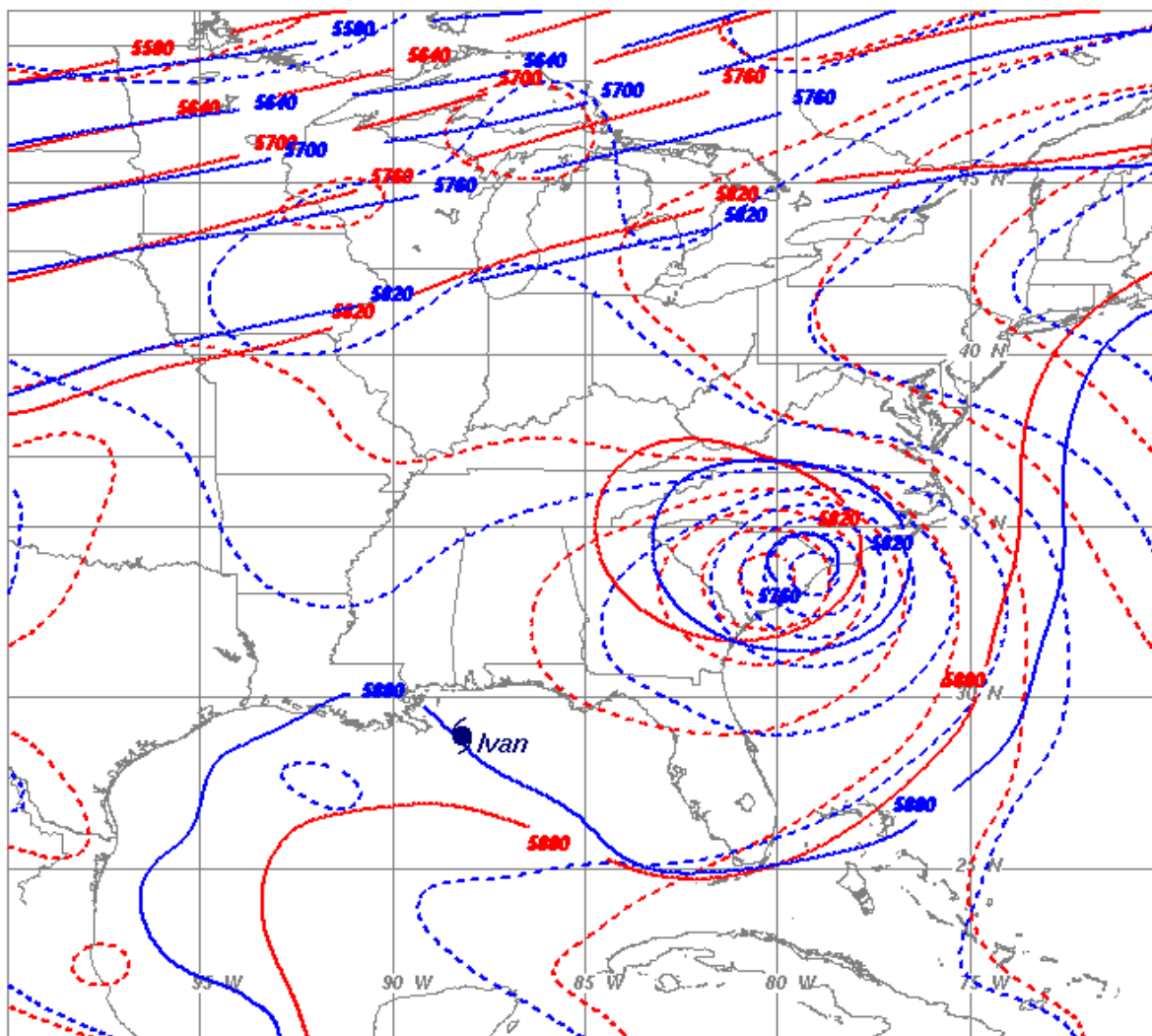


Figure 31: Hurricane Ivan over the southeast US for the 120-hour forecast from 0000 GMT on 11 September 2004. Solid red contours are the 500 hPa heights with MODIS winds; dashed red are 1000 hPa heights. Solid blue are 500 hPa heights of the control; dashed blue are 1000 hPa heights. Actual position at the forecast time of hurricane Ivan is shown with the hurricane symbol.

5.4.4 Case 4: 12 September 2004

The overall ACC for the two different model runs is essentially the same (0.86 vs. 0.84) for the 120-hour forecast over the northern hemisphere (Table 12).

Table 12: 12 September 2004 ACC values for the Northern Hemisphere, 120-hour forecast by wavenumber range.

Wavenumbers:	1-3	4-9	10-20	1-20
MODIS run	0.866	0.865	0.559	0.860
Control run	0.841	0.857	0.601	0.840

The forecast track of Hurricane Ivan is still too far east than the actual path, although in this model run the control has a better position by 200 km in the 120-hour forecast (not shown). This improvement is indicated by the blue feature to the west of the red feature just north of Florida in Figure 33. At this time, it is difficult to attribute this shift to a change in the jet stream position, as was done on the previous day, because the flow across the northern US is mostly zonal. There is a significant difference between the model runs on 11 and 12 September 2004, that may offer some explanation. There were about one-half as many MODIS winds generated on 12 September 2004 than there were on the previous day (Table 7). Just as the addition of new data requires an adjustment in the assimilation and model, removing (or partially removing) data may also cause problems. Nevertheless, the MODIS winds model run out-performed the control in terms of the overall ACC.

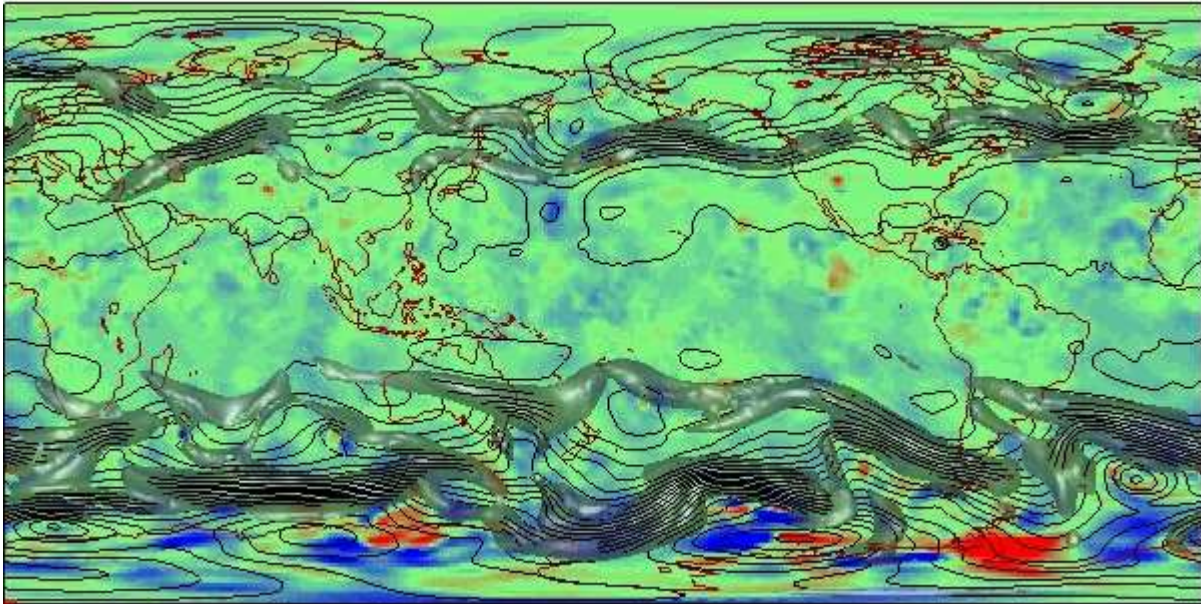


Figure 32: Thickness difference, with and without MODIS winds for the GFS analysis on 12 September 2004 at 0000 GMT model run. Same color scheme as Figure 22.

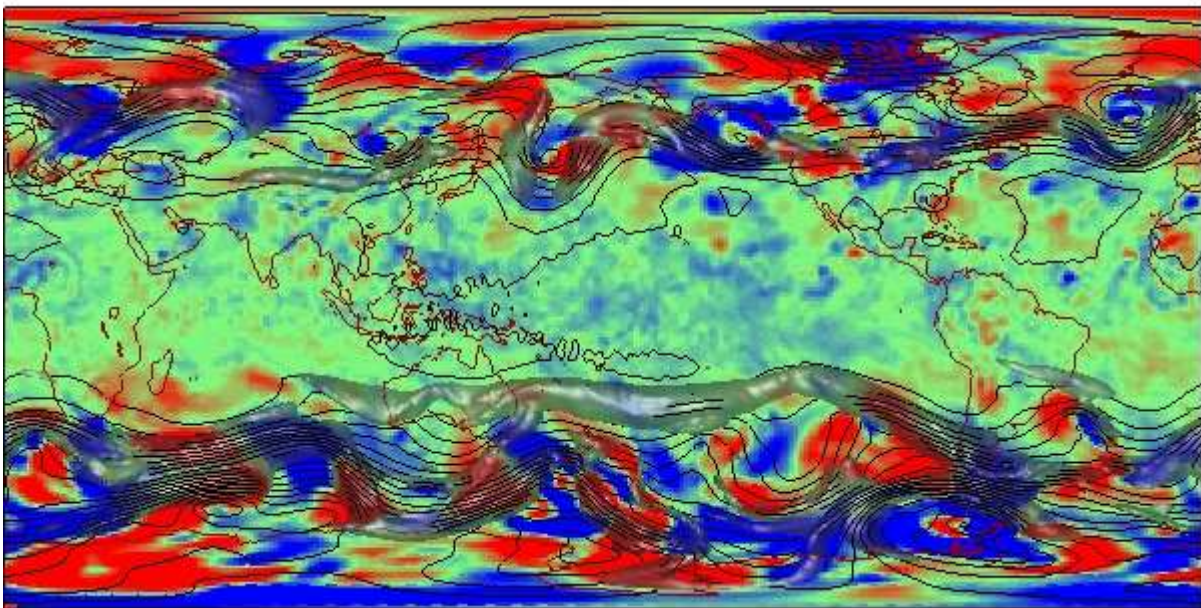


Figure 33: Thickness difference, with and without MODIS winds for the GFS 120-hour forecast from the 12 September 2004 0000 GMT model run. Same color scheme as Figure 22.

5.4.5 Case 5: 17 September 2004

The overall ACC for the control is much worse than the MODIS winds model run, although they are both considered a forecast bust (Table 13). A forecast bust is defined as the ACC below 0.6 for a five-day forecast (Kazumori 2007).

Table 13: 17 September 2004 ACC values for the Northern Hemisphere, 120-hour forecast by wavenumber range.

Wavenumbers:	1-3	4-9	10-20	1-20
MODIS run	0.512	0.614	0.300	0.546
Control run	0.433	0.506	0.140	0.452

In the analysis on this day (Figure 34) there is very little difference between the control and the MODIS winds run. Even by the 120-hour forecast, Figure 35, the difference between the two model runs is not as significant as the other days as evident by smaller areas of red and blue features in and poleward of the jet stream in the northern hemisphere, especially over Europe and Asia. Figure 36 is the verifying analysis for the MODIS experiment and is included so a visual assessment of the forecast bust can be determined. The most notable differences are:

- The small ridge north of Europe, on the far left part of the figure, in the 120-hour forecast is a trough in the analysis.
- The ridge over the central US is broad and centered over the east coast in the 120-hour forecast, while in the analysis it is centered to the west and not as broad.
- The jet in the steep trough off the east coast of the US appears more compact in the 120-hour forecast than it does in the cutoff circulation in the analysis.

This last area is the trough that affected the forecast position of Hurricane Karl, which remained in the mid-Atlantic Ocean throughout its lifetime. It moved generally northwestward for several days “until 22 September when it turned northeastward in response to a deep-layer baroclinic trough developing north of the hurricane.” (Beven 2004) The model containing the MODIS winds held back the advancement of this trough which permitted the forecast position of Karl to track farther west than the control (Figure 37). This resulted in an improved forecast track for Hurricane Karl in the 96-hour forecast, although it was still too far east (MODIS: 19.3°N 45.4°W; Control: 18.7°N 43.0°W) instead of at 18.7°N 47.0°W. This is an error of 184 km and 424 km, respectively.

The 120-hour forecast verifying at 0000 GMT on 22 September 2004 (Figure 38) had Karl moving northward in both model runs in response to the approaching trough, although that was too quick as Karl continued to move north-northwestward until later in this day. The location error at this time was 500 km (MODIS) and 555 km (Control). Using the technique described in section 5.6 *Forecast impact: Phase shift in waves*, the displacement of the wave from 20°W to 60°W at 35°N was 200 km in the 120-hour forecast. This value agrees well with the 240 km improvement in the hurricane position in the 96-hour forecast, but not for the 55 km difference in the 120-hour forecast. The reason the improvement was not as good in the later forecast was due to the trough in the MODIS winds experiment digging farther south than in the control, moving Karl north-northeastward too soon.

The area over the N. Atlantic Ocean has both zonal flow and an intense trough and is used to examine the normalized speed differences between the control and MODIS winds run. This should give an indication of the impact that the MODIS winds have on the forecast of the jet speed (and position) and wave position. Figure 39 is a representative case (from the five cases studied) showing that in regions of relatively zonal flow, the jet stream speed

and position is about the same (no contours in that area of the figure). The elongated contours in the trough result from a large displacement in the position of the trough between the two model runs. Other contours are generally in low wind speed regions, except for the 0.33 contour in Eastern Canada associated with a jet that is displaced because of the decreased speed of the ridge/trough system. Similar signatures were seen in the other cases:

1. the normalized speed differences are large where the ridge and trough positions differ in the two forecast runs,
2. the normalized speed differences were not large in zonal flow regimes, indicating that the MODIS winds do not affect the forecasted speed and position of the mid-latitude polar jet when oriented zonally.

This agrees with Bormann and Thépaut (2004) who found that the MODIS winds have a larger impact on forecasts over Europe when the flow was from the north or northwest.

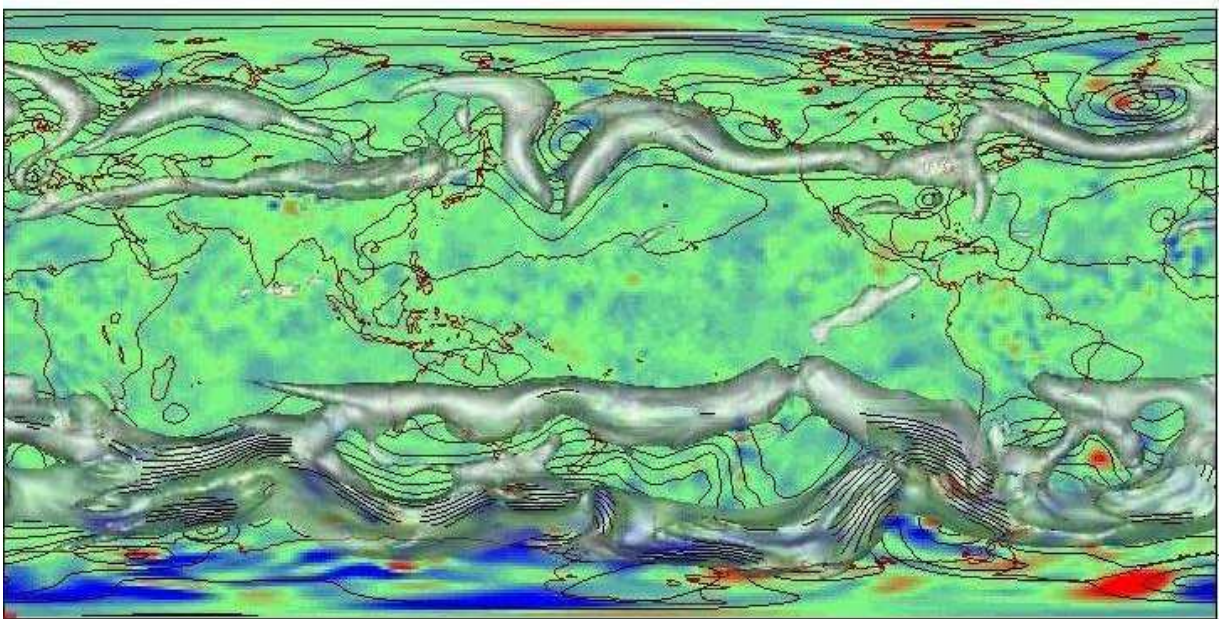


Figure 34: Thickness difference, with and without MODIS winds for the GFS analysis on 17 September 2004 at 0000 GMT model run. Same color scheme as Figure 22.

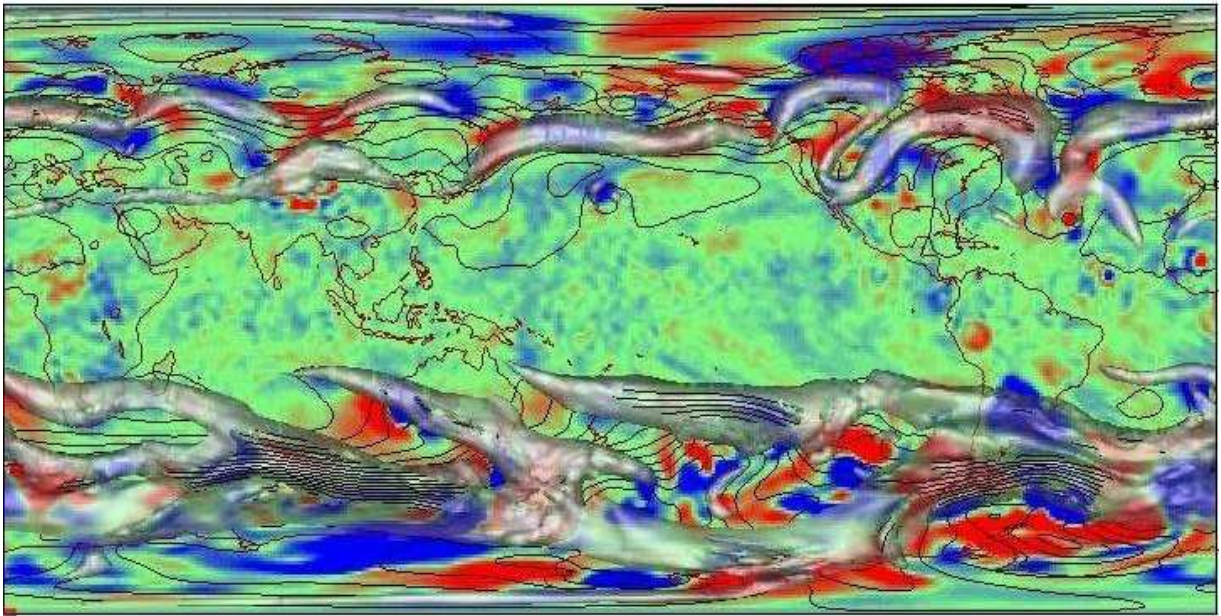


Figure 35: Thickness difference, with and without MODIS winds for the GFS 120-hour forecast from the 17 September 2004 0000 GMT model run. Same color scheme as Figure 22.

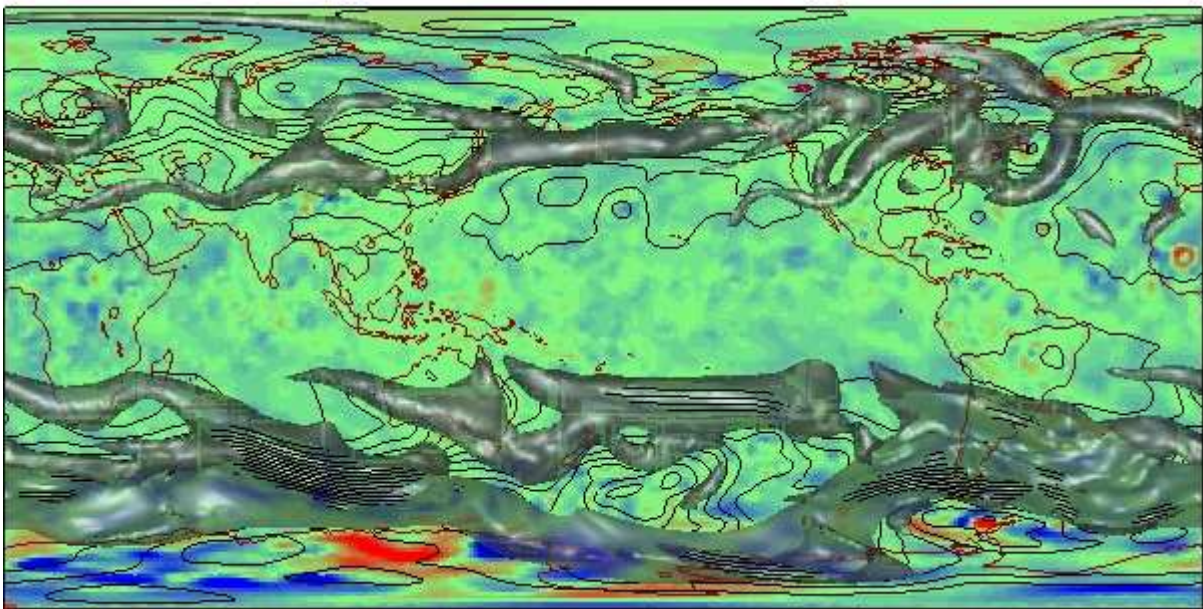


Figure 36: Thickness difference, with and without MODIS winds for the GFS verifying analysis on 22 September 2004 at 0000 GMT. Same color scheme as Figure 22.

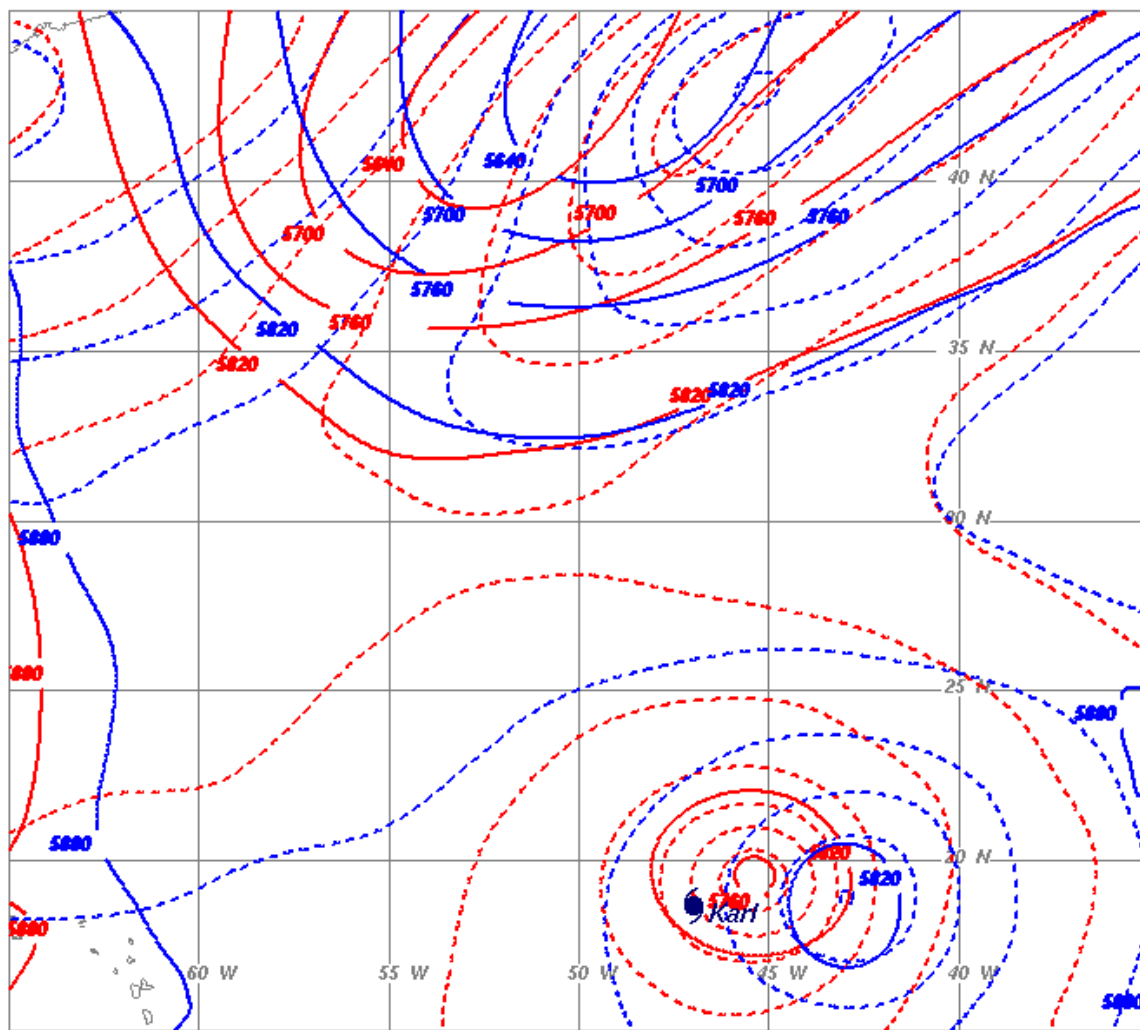


Figure 37: Hurricane Karl over the Atlantic Ocean in the 96-hour forecast from 0000 GMT 17 September 2004. Solid red contours are the 500 hPa heights with MODIS winds; dashed red are 1000 hPa heights. Solid blue are 500 hPa heights of the control; dashed blue are 1000 hPa heights. Actual position at the forecast time of hurricane Karl is shown with the hurricane symbol.

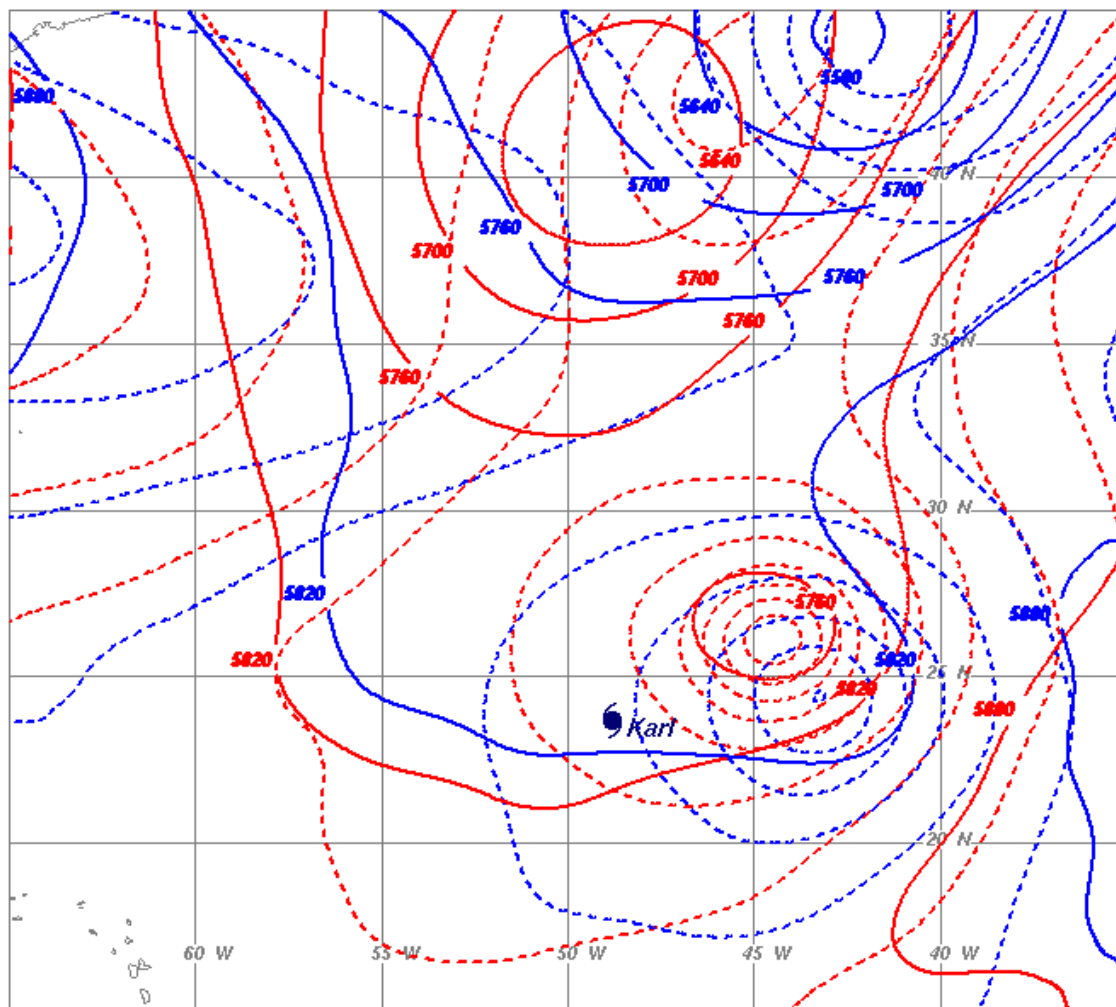


Figure 38: Hurricane Karl over the Atlantic Ocean in the 96-hour forecast from 0000 GMT 17 September 2004. Solid red contours are the 500 hPa heights with MODIS winds; dashed red are 1000 hPa heights. Solid blue are 500 hPa heights of the control; dashed blue are 1000 hPa heights. Actual position at the forecast time of hurricane Karl is shown with the hurricane symbol.

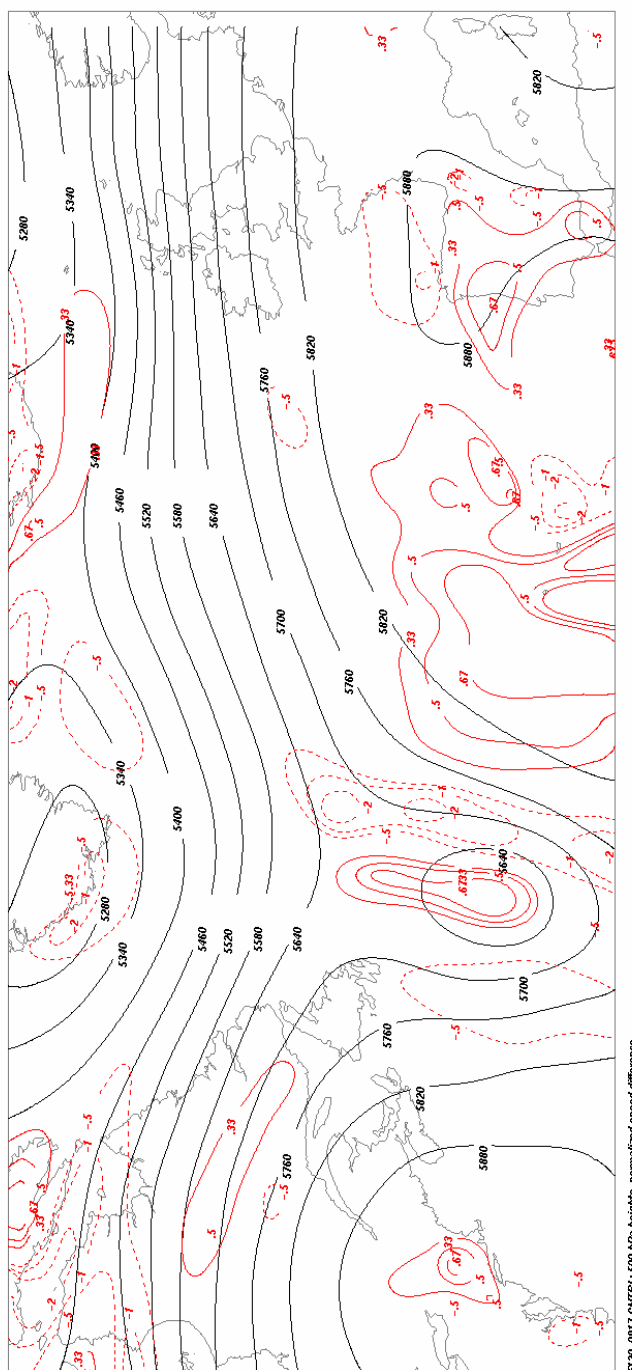


Figure 39: Normalized speed difference (red contours) with 500 hPa heights for the GFS 120-hour forecast from the 17 September 2004 0000 GMT control model run. Positive red contours: control winds are faster by a factor of 1.5, 2, and 3 (contours 0.33, 0.50, 0.67). Negative red contours: control winds are slower by a factor of 1.5, 2, and 3 (contours -0.50, -1, -2).

5.4.6 MODIS winds impact on the NOGAPS analyses and forecasts

Many NWP centers report positive impact in forecasts with the addition of the MODIS winds. As part of the determination on how the MODIS winds impact the analysis and subsequent forecasts, the output from a second model, the NOGAPS, is chosen to compare to what is observed in the GFS output. See *Appendix D: Impact of MODIS winds in the NOGAPS* for an analysis of two cases.

It was found that differences between the two assimilation systems, the GDAS and NAVDAS, could explain observed differences in the thickness fields. Three examples are:

1. The NOGAPS thickness difference features are smoother than what is observed from the GFS, even though the spatial resolution of the two models is approximately the same. The NAVDAS creates 'super observations' which may smooth out small-scale details, while the GDAS uses the winds as individual observations.
2. The NOGAPS differences are larger over the poles in the analysis than in the GFS. This may be due to the NAVDAS assigning a medium weight to the MODIS winds, while the GDAS uses a low weight.
3. The NOGAPS difference features do not spread as far south in the analysis as in the GDAS. This may be due to the dynamic bias correction and spectral interpolation⁶ in the GDAS, which tend to propagate the influence of observations well-away for the observed location.

Despite these differences in the assimilating and modeling, both systems result in an overall positive impact in forecasts.

⁶ The SSI in the GDAS is scheduled to be replaced by the Gridpoint Statistical Interpolation (GSI) in May 2007. This will make it more similar to the NAVDAS, in terms of the interpolation technique.

5.4.7 AMSU radiances impact on GFS analyses

An AMSU radiance denial experiment was investigated to determine the representativeness of the MODIS winds impact in GFS analyses. This is described in *Appendix E: Impact of AMSU Radiances in the GFS*. As with the MODIS winds thickness analysis, the AMSU radiances had a consistent impact over the two weeks of available grids. Because the radiances are a global dataset and are weighted higher than satellite winds in the assimilation, their impact on the analysis was larger than the MODIS winds. In fact, AMSU radiances have the largest impact of any assimilated satellite data (Zapotocny et al. 2007). Nevertheless, the MODIS winds still have an impact in their experiment where AMSU radiances were routinely assimilated. This additional impact over the thermally balanced radiances suggests that the MODIS winds may be providing non-balanced wind information (the ageostrophic component).

5.5 Analysis and forecast: Ageostrophic wind

The above analysis depicts changes in the geopotential height thickness due to the addition of the MODIS winds. The polar winds are derived generally poleward of 65° latitude, while the differences noted in the thickness field are near the jet stream at 50°N. The mass balance in the model propagates this wind information through adjustments in the height field. Since there is a balance between the winds and the height field, differences in the wind field near the jet stream were examined: specifically the geostrophic and ageostrophic winds.

The ageostrophic wind is computed here by taking the difference between the model wind and a computed geostrophic wind based on the geopotential height. This is not an accurate representation of the ageostrophic winds in model space, as independent post processes smooth the output grids without regard to maintaining a mass balance. Also, the parameter precision in the model output grids is 0.1 units, which may cause problems in computations where differences are small. Despite these shortcomings, computed fields of ageostrophic wind, Figure 40, match the schematic representation and speed (on the order of 20 m s^{-1}) in Shapiro and Kennedy (1981). Therefore, these computed ageostrophic winds will serve as a proxy.

The relationship between the divergence of the ageostrophic wind and vorticity advection (Equation 13) assumes that the isallobaric component of the ageostrophic wind is negligible. This simplification facilitated the derivation and resulted in a basic relationship. However, in the following discussions, the computed fields of ageostrophic wind (and derivatives) are based on the part of the total wind that is not in geostrophic balance; therefore, the complete ageostrophic wind is used.

Figure 41 and Figure 42 show the geostrophic and ageostrophic differences in the two analyses from 11 September 2004, respectively. These differences are about the same magnitude, with a maximum of about 5 m s^{-1} . These significant differences in the ageostrophic wind will have a direct effect on the speed of the associated shortwave, since the divergence of the ageostrophic wind is related to geostrophic vorticity advection (Eq. 13), an indicator of wave propagation speed.

Figure 43 and Figure 44 show the difference in the divergence of the ageostrophic wind at the analysis time of 0000 GMT on 11 September 2004. The oval areas are the largest differences and should correspond to where the largest change in wave speed would occur in the forecasts. Figure 45 depicts the same oval areas in the analysis (top) and the 72-hour forecast (bottom), overlaying the thickness difference regions. The two large thickness difference areas over the US in the 72-hour forecast are the result of the wave pattern being slowed. This is also the same region to where the large differences in the divergence of the ageostrophic wind have translated (ovals). The area in the central Pacific has also slowed. A significant thickness difference region just southeast of Alaska originated near ageostrophic wind difference in the West Pacific in the analysis, and moved quickly associated with a shortwave just north of the jet stream.

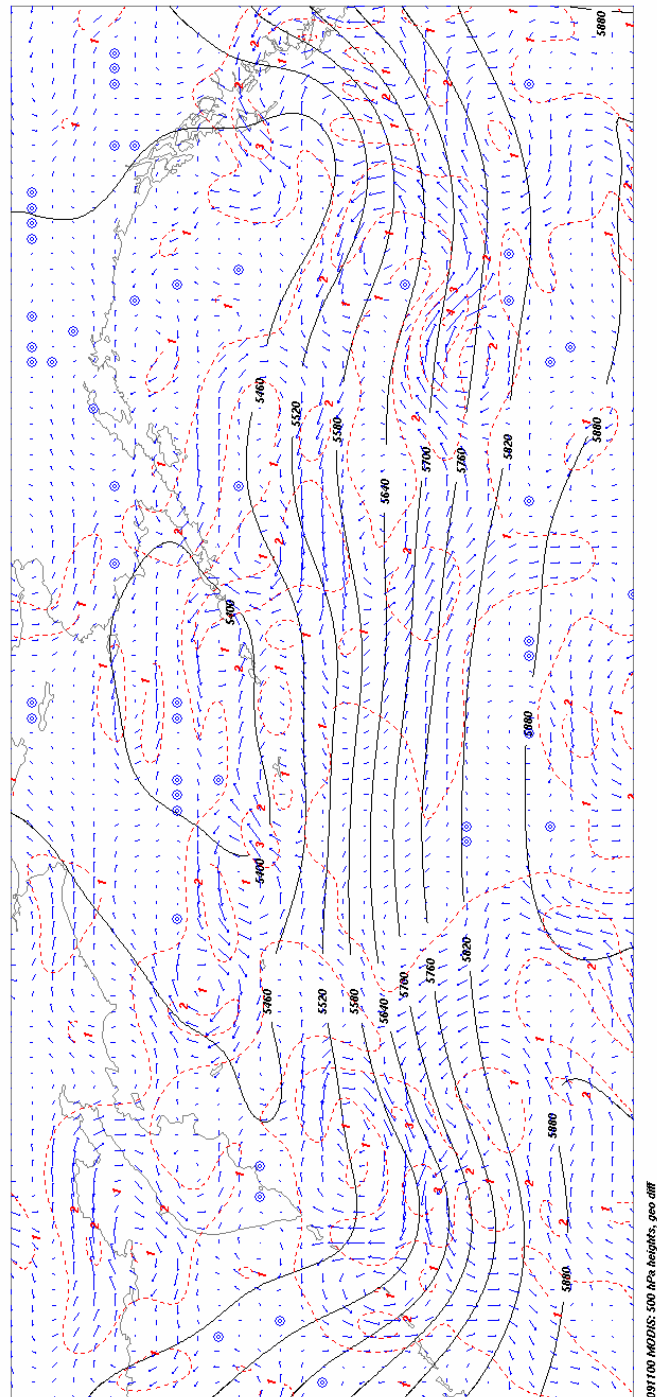


Figure 41: Geostrophic wind field differences for the analysis on 11 September 2004 over the North Pacific Ocean. Wind vector differences are shown as blue arrows. Dashed red contours are speed in m s^{-1} . Solid black contours are 500 hPa heights of the MODIS run.

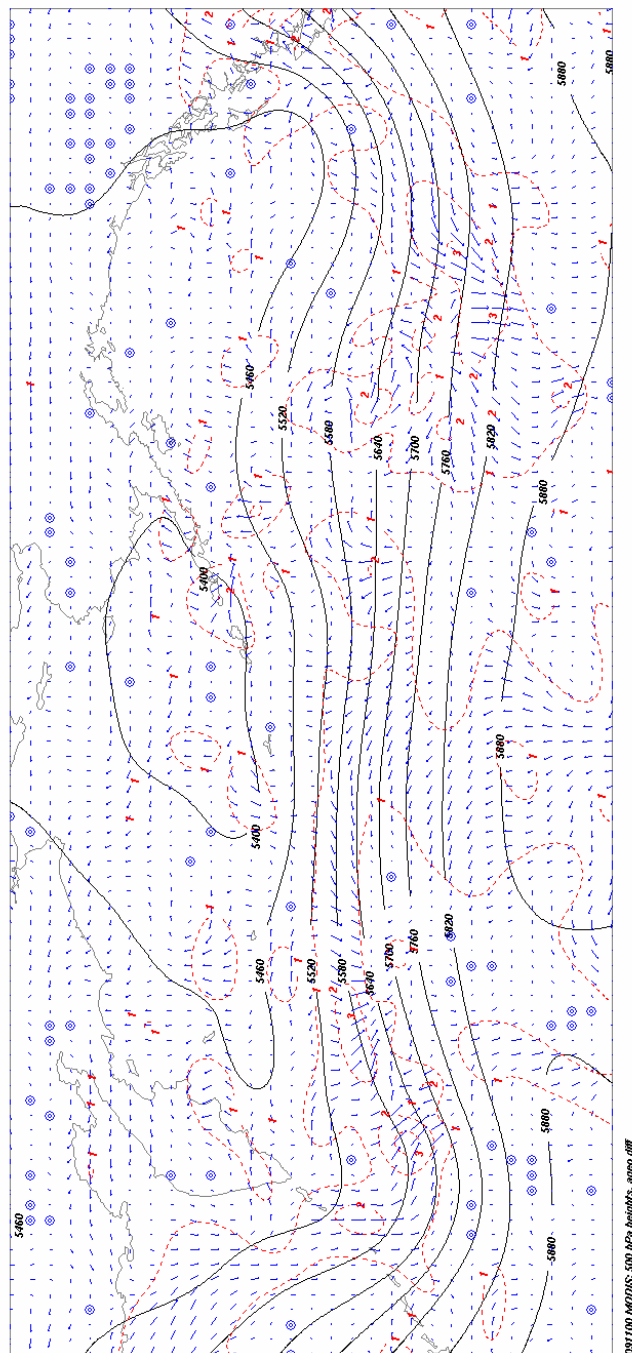


Figure 42: Ageostrophic wind field differences for the analysis on 11 September 2004 over the North Pacific Ocean. Wind vector differences are shown as blue arrows. Dashed red contours are speed in m s^{-1} . Solid black contours are 500 hPa heights of the MODIS run.

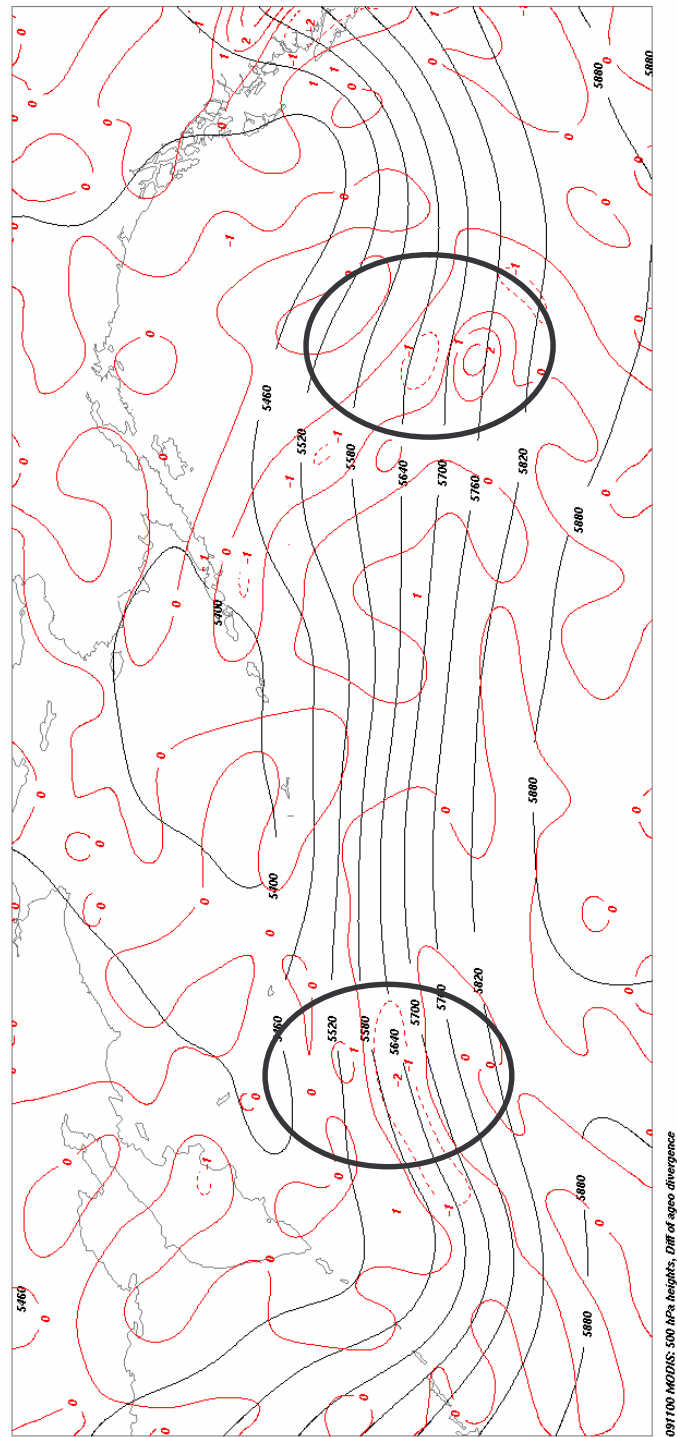


Figure 43: Difference in the divergence of the ageostrophic wind (10^{-5} s^{-1}) at 500 hPa between the MODIS winds and control model runs over the North Pacific Ocean. This is equivalent to the difference in vorticity advection (Eq. 13). The largest differences are circled. This is the analysis at 0000 GMT on 11 September 2004.

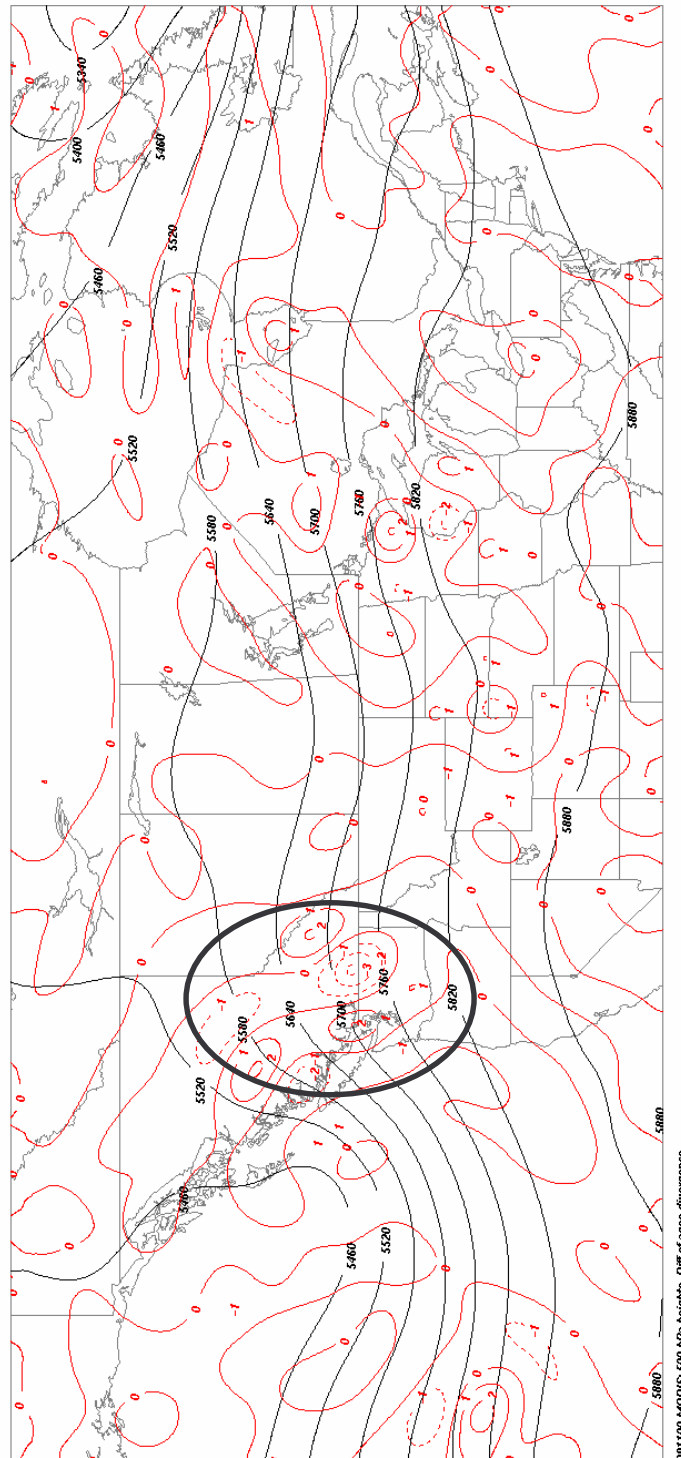


Figure 44: Difference in the divergence of the ageostrophic wind (10^{-5} s^{-1}) at 500 hPa between the MODIS winds and control model runs over the US and Canada. This is equivalent to the difference in the vorticity advection (Eq. 13). The largest differences are circled. This is the analysis at 0000 GMT on 11 September 2004.

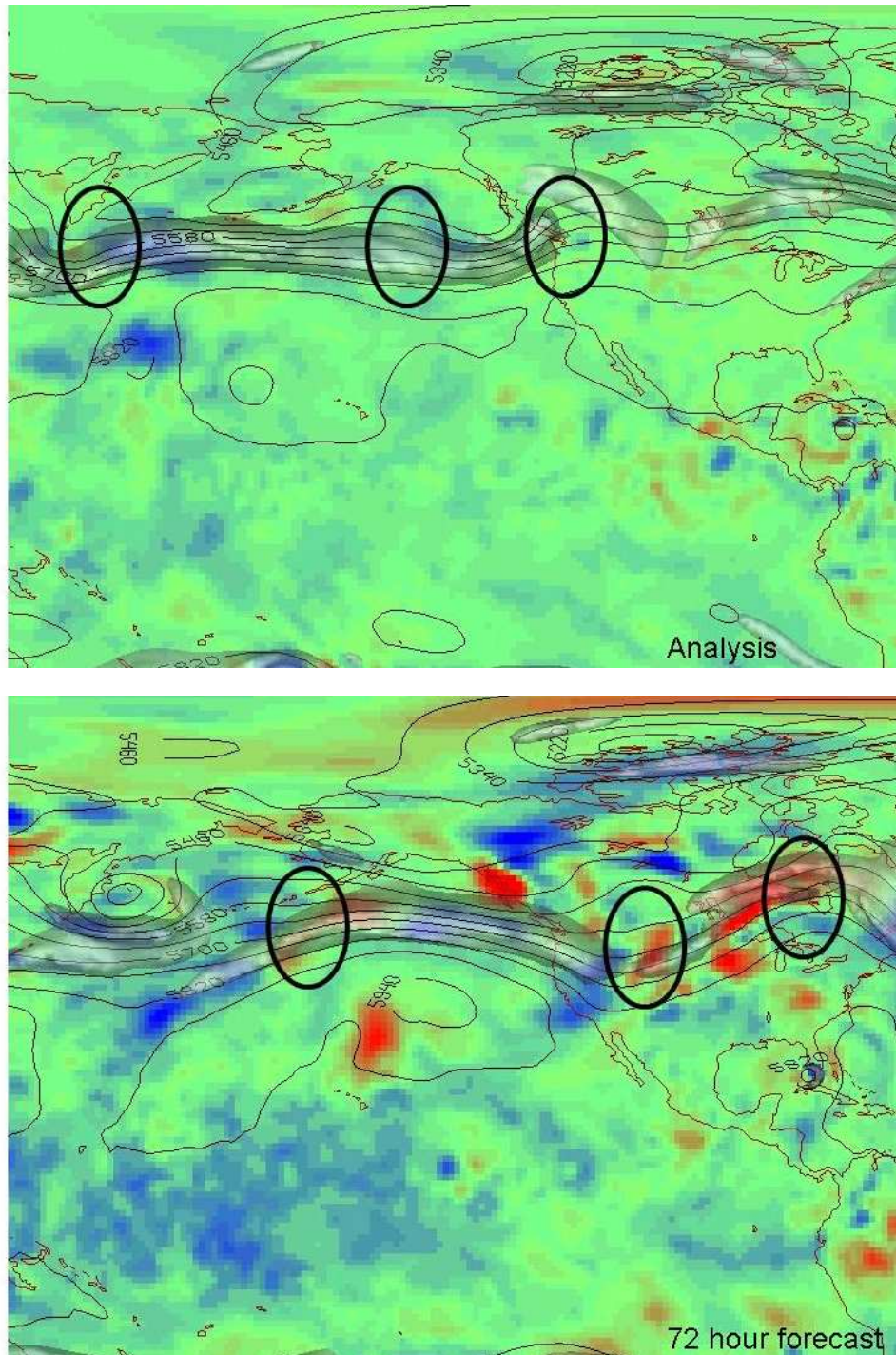


Figure 45: The analysis (top) and 72-hour forecast (bottom) showing differences in the 1000-500 hPa thickness, along with the MODIS 500 hPa heights. Same color scheme as Figure 22. The ovals are from Figure 43 and Figure 44. Positions of ovals in the 72-hour forecast represent a subjective positioning using intermediate forecast times to guide.

5.6 Forecast impact: Phase shift in waves

The previous section provided a qualitative assessment on how changes in the wind (or height) field near the jet stream affects the wave propagation speed. This section provides a measure on how large this speed difference is by determining the phase shift in the waves from the two model runs. This shift is computed in one dimension, in the zonal direction.

The phase shift of the 500 hPa waves for the 120-hour forecast between the MODIS winds and control is measured at both 35°N and 50°N. This is done by extracting the 500 hPa heights at the two latitude bands (Figure 46 and Figure 47). These figures show that the shift between the two models changes sign along the latitude band. Sometimes the MODIS winds slow the waves (longitude 320 to 340) or increase the wave speed (longitude 250 to 280) as seen in Figure 46. Table 14 summarizes the global phase shift at these two latitudes. This was done by fitting a 2nd order polynomial to the correlation coefficient evaluated with differing lag distances between the two curves.

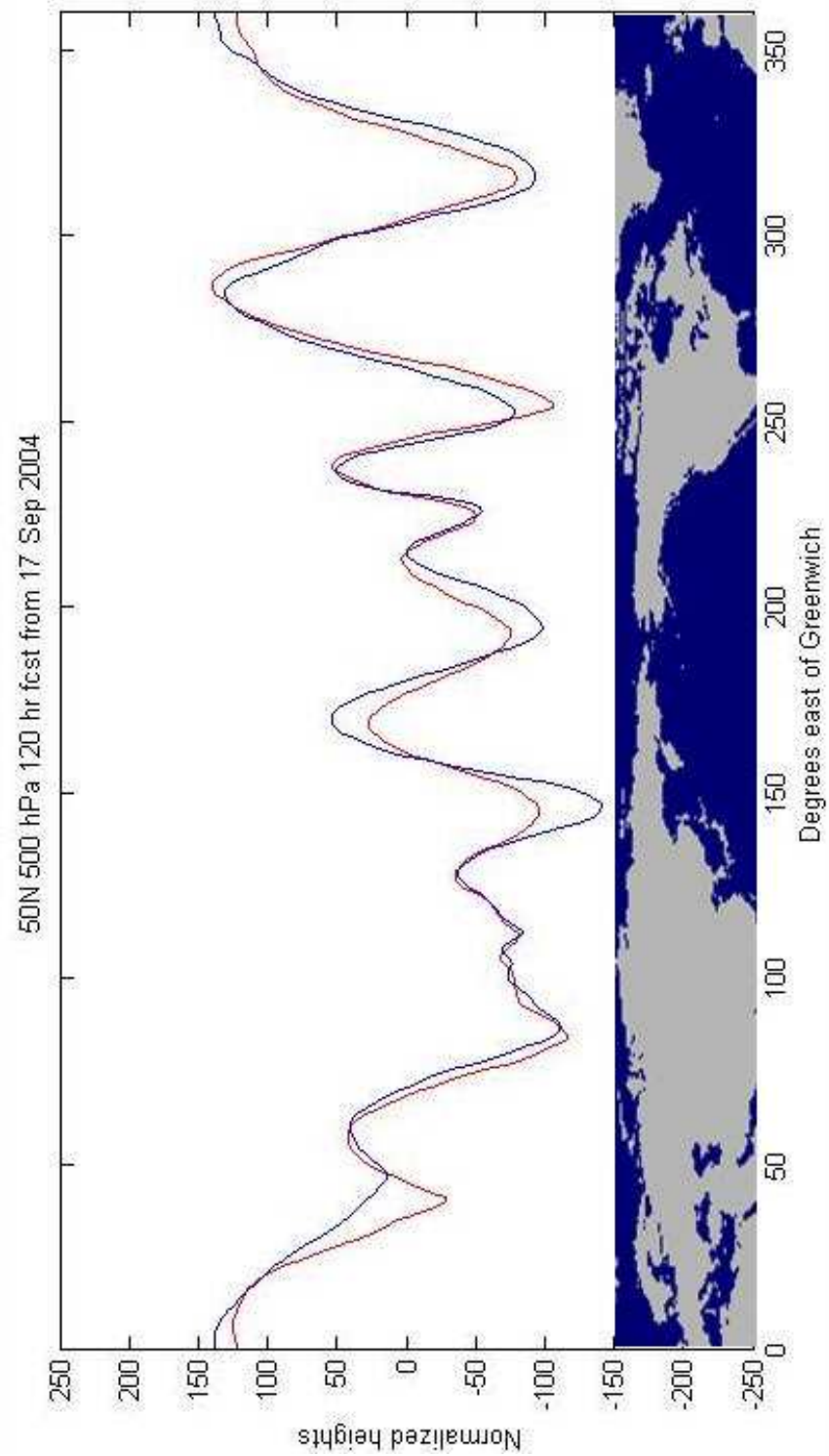


Figure 46: Latitude slice at 50°N of 500 hPa heights for the 120 hour forecast from 17 September 2004 for the control (blue) and the MODIS winds (red).

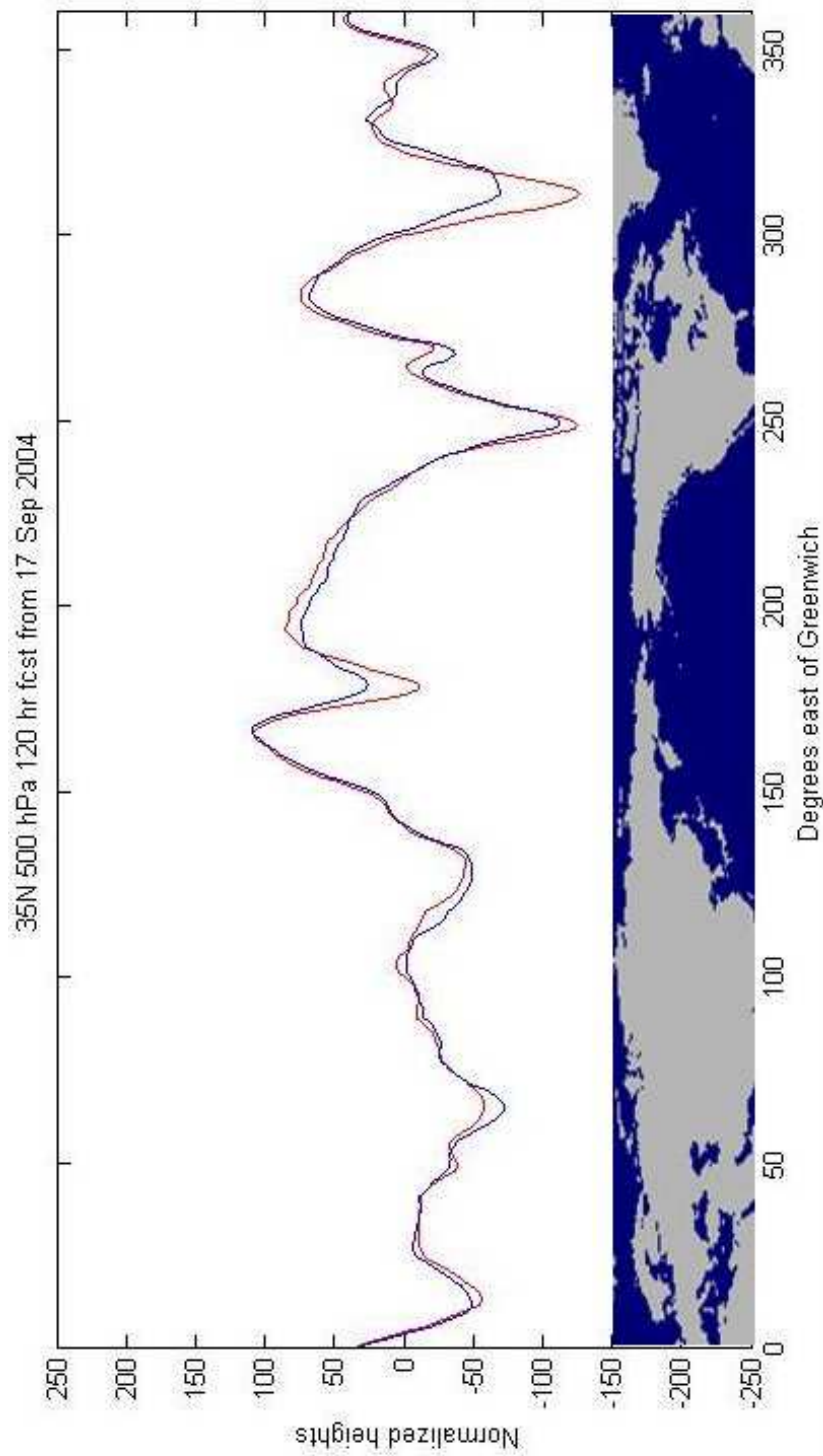


Figure 47: Latitude slice at 35°N of 500 hPa heights for the 120 hour forecast from 17 September 2004 for the control (blue) and the MODIS winds (red).

Table 14: Phase shift of 500 hPa heights at 50°N and 35°N for the 120-hour forecast for the five case studies. The shift is measured in degrees of longitude and is converted to kilometers in the table.

	50 N (deg. Long.)	50 N (km)	35 N (deg. Long.)	35 N (km)
06 Sep 04	+0.5	+35	-0.07	-6
07 Sep 04	-0.4	-31	-0.5	-49
11 Sep 04	-0.4	-30	-0.5	-49
12 Sep 04	-1.0	-74	+0.4	+33
17 Sep 04	-0.4	-28	-0.9	-85

These numbers are not very large for a 120-hour forecast, but they do represent an average shift which is composed of both positive and negative shifts around the latitude band, but it is negative 80% of the time for this limited number of cases. The average magnitude phase shift of the waves in these five cases is about 0.5 degrees longitude, or about 50 km. The shift for some specific waves has been measured at 100 to 200 km (see sections 5.4.3 Case 3: 11 September 2004 and 5.4.5 Case 5: 17 September 2004).

From the sensitivity analysis in section 4.5.1 *Rossby wave*, a 1 m s^{-1} change in zonal wind speed or a 500 km change in the wavelength will result in a 430 km change in wave position in five days. For the extreme case measured at a 200 km shift, this could result from about 0.5 m s^{-1} change in the zonal wind speed. The other factor that can change the wave speed is the wave amplitude, which has also changed in this example (see Figure 46 and Figure 47). This effect could be additive or canceling, but was not investigated further.

5.7 Forecast impact: Tropical cyclone positions

It's been well documented that the addition of satellite data improves the forecast tracks of tropical cyclones. Velden et al. (1998) showed this for geostationary winds and Baker and Campbell (2004) found improvement assimilating global AMSU-A radiances. These are cases where the satellite data is in the tropical regions. Surprisingly, the MODIS winds also have a positive impact on hurricane track forecasts, specifically for the 2004 season (Jung et al. 2007; Zapotocny et al. 2007).

NCEP's tropical cyclone track verification was done for the two model runs: with and without the MODIS winds for the 2004 hurricane season. A somewhat startling result is in Table 15 and Table 16. In the 120-hour forecast, the addition of the MODIS winds resulted in an average improvement of 50 nmi in the forecast track of tropical cyclones. Moreover, this better forecast occurred 70% of the time, which indicates that this was an overall improvement and not the result of large track differences in a few isolated cases. Also, as seen in other verifications, the impact of the MODIS winds is insignificant in the early forecast times, with the best impact in the five-day forecast which suggests that time is needed for information propagation.

Table 15: Tropical cyclone track forecast errors in nautical miles for the 2004 hurricane season

Forecast time (hrs)	0	24	48	120
Number of cases	74	64	52	34
Control error	13.2	66.5	102.8	301.1
Control + MODIS error	11.4	60.4	89.0	252.0

Table 16: Frequency (in percent) of superior tropical cyclone track performance for the 2004 hurricane season

Forecast time (hrs)	0	24	48	120
Number of cases	74	64	52	34
Control	48.9	44.8	39.6	29.4
Control + MODIS	51.1	55.2	60.4	70.6

These statistics are based on tropical (or subtropical) cyclones that were present at both the forecast time and verification time. The verification stops at the last time the system was either a tropical depression or a subtropical depression. This means these statistics cover the cyclones that have moved into mid-latitudes but are still tropical in nature. Also, this is a homogeneous verification, ensuring that both model runs contain the same tropical cyclones.

From the case study sections that included tropical cyclones, the following was found: The 120-hour forecast for Ivan on 11 September 2004 and Karl on 17 September 2004 have track improvement values close to the 50 nmi average found for the entire hurricane season (Table 17). The case of Ivan on 12 September 2004, where the MODIS winds degraded the forecast position by 108 nmi, appears to be anomalous.

Table 17: Tropical cyclone track differences (nmi) between the control and the MODIS winds runs. Positive indicates that the MODIS winds improved the track forecast.

Forecast time:	<u>96 hours</u>	<u>120 hours</u>
Ivan 11 September 2004	27	54
Ivan 12 September 2004	n/a	-108
Karl 17 September 2004	129	30

6. Conclusions

The assimilation of the MODIS polar winds in numerical models has resulted in a positive impact in forecasts not only in the polar regions, but also extending to lower latitudes. It was found that the data assimilation system can result in analysis differences in areas away from the data location that cannot be explained with atmospheric dynamics (mass and thermal balance constraints in the model reacting to the data addition). These differences can most likely be attributed to adjustments in the global dynamic bias correction and a spectral interpolation scheme used in NCEP's GDAS, but this was not investigated any further. The specific areas examined were adjustments to the mass, thermal, and wind fields (which are inherently inter-related) in the vicinity of the jet stream and how those changes affected the forecasts. It was found that:

1. In the model analysis, the mass adjustment required due to the addition of the MODIS winds results in a change to both the geostrophic and ageostrophic winds on the order of 5 m s^{-1} in the vicinity of the jet stream.
2. In all five cases, there is a predominant trough off the east coast of the two northern hemisphere continents; primarily data void regions. This is also the region where the MODIS winds have the largest and most consistent impact in analysis of the 500 hPa heights. The impact is not as consistent over the continents, where there is good rawinsonde coverage.
3. The MODIS winds have the largest impact on synoptic-scale waves (10 to 20 wave numbers, wavelengths of approximately 1500 to 3000 km in mid-latitudes), based on the northern hemisphere anomaly correlation coefficient at 500 hPa for the 120-hour forecast,

4. The addition of the MODIS winds results in an average change to the 500 hPa wave propagation on the order of 0.5 to 1 degree of longitude over a 120-hour forecast for latitude bands 50°N and 35°N.
 - a. In 8 out of 10 instances (from 2 latitude bands for 5 cases) the addition of the MODIS winds, on average, slowed the northern hemisphere wave progression as evident in the 120-hour forecasts. Interestingly, although perhaps coincidentally, this agrees with Francis (2002) that the zonal flow in the arctic region was too fast, westerly, in the model reanalysis fields.
 - b. The impact is much larger (up to 2 degrees of longitude or nearly 200 km) for specific waves.
5. Synoptic-scale waves in the vicinity of hurricanes Ivan and Karl were slowed (by 100 km and 200 km, respectively) with the addition of the MODIS winds, allowing these hurricanes to track further west in the 120-hour forecasts. These new positions were an improvement in the forecast.

From the five cases examined, it was determined that the addition of the polar winds modifies the mass balance in synoptic-scale waves near the polar jet streams, more consistently in data void regions. This change in mass balance is evident in differences in the ageostrophic wind, which has an effect on the speed and amplitude of baroclinic waves that extends from the jet stream into lower latitudes in later forecast times. These results reveal the substantial impact that polar-only observations have on the predictability of global weather systems.

7. Future Work

Although the observation of a change in the jet stream wave speed explains how measurements in the polar regions affect mid- and low-latitude flow, the question remains: What is the primary mechanism through which the information contributed by the polar winds affect the jet stream?

Many approaches were taken to begin to answer that question. Studies were done to examine the importance of the assimilation method and to determine the relative importance of the MODIS wind impact on large-scale Rossby waves and smaller scale short waves. However, with only limited opportunities to run specific experiments it is not completely understood if the positive forecast impact is primarily due to:

1. effects of the assimilation system,
2. a better positioning and/or resolving of dynamical features, or
3. a better measurement of the total wind, which may include a significant ageostrophic component in the jet regions?

Based on the knowledge gained in this research, additional experiments will be designed and case studies produced to further investigate and answer these questions.

Terra and Aqua are the only polar-orbiting satellites with a high-resolution water vapor sensor. However, these two satellites are at or nearly at the end of their designed lifetimes and the future satellite series, the National Polar-orbiting Operational Environmental Satellite System (NPOESS), will not have a water vapor channel. With more than two-thirds of the MODIS AMVs derived in the water vapor channel (many of these designated as clear-sky), how will the absence of this sensor affect model forecasts? Preliminary results from Riishojgaard et al. (2006) are not conclusive, except to note that the most significant impact

is achieved when both infrared and water vapor AMVs are assimilated simultaneously. More experiments are needed to better understand the relative contributions to forecast improvement from the AMVs derived from different sensors.

8. References

Ackerman, S., K. Strabala, W. P. Menzel, R. Frey, C. Moeller, L. Gumley, B. Baum, S. Seeman, and H. Zhang, 2002. Discriminating clear-sky from cloud with MODIS. ATBD, University of Wisconsin-Madison, Madison, WI.

Baker, N. L. and W. F. Campbell, 2004. The impact of AMSU-A radiance assimilation in the U.S. Navy's Operational Global Atmospheric Prediction System (NOGAPS). Thirteenth Conference on Satellite Meteorology and Oceanography, Norfolk, VA.

Barnes W.L., T.S. Pagano, and V.V. Salomonson, 1998, Prelaunch characteristics of the Moderate Resolution Imaging Spectroradiometer (MODIS) on EOS-AM1. IEEE Trans. Geosci. Remote Sensing, 36, 1088-1100.

Beven, J., 2004. Tropical Cyclone Report: Hurricane Karl. Retrieved 27 April 2007 from <http://www.nhc.noaa.gov/2004karl.shtml>.

Bormann, N., S. Saarinen, G. Kelly, J.-N. Thépaut, 2003. The spatial structure of observation errors in atmospheric motion vectors from geostationary satellite data. Mon. Wea. Rev., 131, 706-718.

Bormann, N., and J.-N. Thépaut, 2003. Assimilation of polar MODIS Atmospheric Motion Vectors at ECMWF, Twelfth Conference on Satellite Meteorology, AMS, Long Beach, CA.

Bormann, N., and J.-N. Thépaut, 2004. Impact of MODIS Polar Winds in ECMWF's 4DVAR Data Assimilation System. Mon. Wea. Rev., 132, 929-940.

Brown, O. B., and P. J. Minnett, 1999. MODIS Infrared Sea Surface Temperature Algorithm, Tech. Report ATBD25, University of Miami, Miami, FL.

Cress, A., 2004. Impact of MODIS winds on the global NWP system of the German weather Service. Proc. Of the Seventh Int. Winds Workshop, Helsinki, Finland, WMO (Available online at www.eumetsat.int/).

Daley, R. and E. Barker, 2001. NAVDAS: formulation and diagnostics. Mon. Wea. Rev., 129, 869-883.

Doswell, C.A. III, and L.F. Bosart, 2001. Extratropical synoptic-scale processes and severe convection. Severe Convective Storms , Meteor. Monogr , 28, no. 50, Amer. Meteor. Soc., 27-69.

Forsythe, M. and H. Berger, 2004. MODIS winds: Latest results at the MET Office, Proc. Of the Seventh Int. Winds Workshop, Helsinki, Finland, WMO (Available online at www.eumetsat.int/).

Francis, J. A., 2002. Validation of reanalysis upper-level winds in the Arctic with independent rawinsonde data. *Geophys. Res. Lett.*, 29, No. 9.

Gallimore, R. and D. Johnson, 1981. The forcing of the meridional circulation of the isentropic zonally averaged circumpolar vortex. *J. Atmos. Sci.*, 38, 583-599.

Guenther, B., G.D. Godden, X. Xiong, E. Knight, S.-Y. Qiu, H. Montgomery, M. Hopkins, M. Khayat, and Z. Hao, 1998. Prelaunch algorithm and data format for the Level 1 calibration products for the EOS-AM1 Moderate Resolution Imaging Spectroradiometer (MODIS). *IEEE Trans. Geosci. Remote Sensing*, 36, 1142-1151.

Hasler, A. F., W. E. Shenk, and W. C. Skillman, 1977. Wind estimates from cloud motions: Results from phases I, II, and III of an in situ aircraft verification experiment. *J. Appl. Meteor.*, 16, 812-815.

Hayden, C. and R.J. Pursor, 1995. Recursive filter objective analysis of meteorological fields: Applications to NESDIS operational processing. *J. Appl. Meteor.*, 34, 3–15.

Herman, L., 1989. Validation of cloud motion vectors from AVHRR images. Twelfth Conference on Weather Analysis and Forecasting, Monterey, CA.

Herman, L., 1993. High frequency satellite cloud motion at high latitudes. Eighth Symposium on Meteorological Observations and Instrumentation. Anaheim, CA.

Herman, L. and F. Nagle, 1994. A comparison of POES satellite derived winds techniques in the arctic at CIMSS. Seventh Conference on Satellite Meteorology and Oceanography, Boston, MA.

Hinzman L.D., N. Bettez, W. Bolton, F. Chapin, M. Dyrgerov, C. Fastie, B. Griffith, R. Hollister, A. Hope, H. Huntington, A. Jensen, G. Jia, T. Jorgenson, D. Kane, D. Klein, G. Kofinas, A. Lynch, A. Lloyd, A. McGuire, F. Nelson, W. Oechel, T. Osterkamp, C. Racine, V. Romanovsky, R. Stone, D. Stow, M. Sturm, C. Tweedie, G. Vourlitis, M. Walker, D. Walker, P. Webber, J. Welker, K. Winker, K. Yoshikawa, 2005. Evidence and implications of recent climate change in northern Alaska and other Arctic regions. *Climatic Change*, 72, 251–298.

Holmlund, K., 1998. The utilization of statistical properties of satellite-derived atmospheric motion vectors to derive quality indicators. *Weather and Forecasting*, 12, 1093–1103.

Holmlund, K., Velden, C. and Röhn., M. 2001. Enhanced automatic quality control applied to high-density satellite derived winds. *Mon. Wea. Rev.* 129, 517 – 529.

Holton, J. R., 1992. *An introduction to dynamic meteorology*. Academic Press, San Diego.

Jedlovec, G.J. and R.J. Atkinson, 1998. The Marshall Automated Wind algorithm: Error analysis, quality control and climate applications. Proceedings of the Fourth International Winds Workshop, EUMETSAT, Saanenmoser, 247-254.

Jung, James A., T. Zapotocny, R. Treadon, and J. LeMarshall, 2007. A two season impact study of satellite and in-situ data in the NCEP Global Data Assimilation System. Weather and Forecasting, Accepted.

Kazumori, M. and Y. Nakamura, 2004. MODIS polar winds assimilation experiments at JMA, Proc. of the Seventh Int. Winds Workshop, Helsinki, Finland, WMO (Available online at www.eumetsat.int/).

Kazumori, M., 2007. Impact study of DMSP F-16 SSMIS radiances in NCEP global data assimilation system. Retrieved 27 April 2007 from http://www.emc.ncep.noaa.gov/seminars/presentations/2007/kazumori_070327.pdf

Key, J. R., D. Santek, C. S. Velden, N. Bormann, J.-N. I Thépaut, L. P. Riishojgaard, Y. Zhu, and W. P. Menzel, 2003. Cloud-Drift and Water Vapor Winds in the Polar Regions from MODIS. IEEE Trans. Geosci. Remote Sens., 41, 482-492.

Key, J R., D. A. Santek, C. S. Velden, M. J. Daniels, W. Bresky, and W. P. Menzel, 2005. Polar winds from satellite imagers for numerical weather prediction and climate applications. Conference on Polar Meteorology and Oceanography, 8th, San Diego, CA, 8-13 January 2005 (preprints). American Meteorological Society, Boston, MA.

Krishnamurti, T. N., K. Rajendran, T.S.V. V. Kumar, S. Lord, Z. Thoth, X. Zou, S. Cocke, J. Ahlquist, I.M. Navon, 2003. Improved skill for the anomaly correlation of geopotential heights at 500 hPa. Mon. Wea. Rev., 131, 1082-1102.

Lazzara M.A., J. Benson, R. Fox, D. Laitsch, J. Rueden, D. Santek, D. Wade, T. Whittaker, and J. T. Young, 1999. The Man computer Interactive Data Access System: 25 years of interactive processing. Bull. Amer. Meteor. Soc., 80, 271–284.

LeMarshall, J., R. Seecamp, A. Rea, M. Dunn, J. Jung, J. Daniels and C. Velden, 2004. Error characterization and application of atmospheric motion vectors over Australia and high latitudes, Proc. Of the Seventh Int. Winds Workshop, Helsinki, Finland, WMO (Available online at www.eumetsat.int/).

Martin, J.E., 2006. *Mid-latitude atmospheric dynamics: a first course*. Wiley, Hoboken.

Menzel, W. P., 2001. Cloud Tracking with Satellite Imagery: From the Pioneering Work of Ted Fujita to the Present. Bull. Amer. Meteor. Soc., 82, 33-47.

Menzel, W. P., S. Seemann, J. Li, and L. Gumley, 2002. MODIS atmospheric profile retrieval ATBD. University of Wisconsin-Madison, Madison, WI.

Merrill, R.T., 1989. Advances in the automated production of wind estimates from geostationary satellite imagery. Preprints, Fourth Conf. on Satellite Meteorology and Oceanography, San Diego, CA, Amer. Meteor. Soc., 246–249.

Merrill, R.T., W.P. Menzel, W. Baker, J. Lynch, and E. Legg, 1991. A report on the recent demonstration of NOAA's upgraded capability to derive cloud motion satellite winds. *Bull. Amer. Meteor. Soc.*, 72, 372–376.

Nieman, S., J. Schmetz, and P. Menzel, 1993. A comparison of several techniques to assign heights to cloud tracers. *J. Appl. Meteor.*, 32, 1559-1568.

Nieman, S., W. L. Smith, C. M. Hayden, D. Gray, S. T. Wanzong, C. S. Velden, and J. Daniels, 1997. Fully automated cloud-drift winds in NESDIS operations. *Bull. Amer. Meteor. Soc.*, 78, 1121-1133.

Olander, T.L., C.S. Velden, and C. Spinoso, 2000. Creation of a platform-independent version of the UW-CIMSS geostationary, high-density wind derivation algorithm. Preprints, Fifth International Winds Workshop, Lorne, Australia, EUMETSAT, 195–199.

Olander, T., 2001. UW-CIMSS satellite-derived wind algorithm: User's Guide. Version 1.0, 87 pp.

Palmén, E, and C. Newton, 1969. *Atmospheric Circulation Systems: Their structure and physical interpretation*, Academic Press, New York.

Parrish, D. and J. Derber, 1992. The National Meteorological Center's spectral statistical interpolation analysis system. *Mon. Wea. Rev.*, 120, 1747-1763.

Pauley, P. and R. Pauley, 2004. MODIS winds in NAVDAS. Sixteenth Conference on Numerical Weather Prediction, AMS, Seattle, WA.

Pauley, P. and R. Pauley, 2005. Operational testing of MODIS winds in NAVDAS. Ninth Symposium on Integrated Observing and Assimilation Systems for the Atmosphere, Oceans, and Land Surface, AMS, San Diego, CA.

Petty, G.W., 2004. *A First Course in Atmospheric Radiation*, pp. 110-145, Sundog Publishing, Madison.

Pyle, M., D. Keyser, L. Bosart, 2004. A diagnostic study of jet streaks: kinematic signatures and relationship to coherent tropopause disturbances. *Mon. Wea. Rev.*, 132, 297-319.

Rao, P., C. Velden, and S. Braun, 2002. The vertical error characteristics of GOES-derived winds: Description and experiments with numerical weather prediction. *J. of Appl. Meteor.*, 41, 253-271.

Riishojgaard, L. P. and Y. Zhu, 2004. Impact experiments on GMAO data assimilation and forecast systems with MODIS winds during MOWSAP, Proc. of the Seventh Int. Winds Workshop, Helsinki, Finland, WMO (Available online at www.eumetsat.int/).

Riishojgaard, L. P., M. Sienkiewicz, and G. P. Lou, 2006. The impact on forecast skill of water vapor and window channel winds from MODIS, Proc. of the Eighth Int. Winds Workshop, Beijing, China, WMO (Available online at www.eumetsat.int/).

Rohn, M., G. Kelly, and R. Saunders, 2001. Impact of a new cloud motion wind product from Meteosat on NWP analyses and forecasts. *Mon. Wea. Rev.*, 129, 2392-2403.

Santek, D., J. Key, W. P. Menzel, C. Velden, and J. Heinzelman, 2002. Deriving winds from MODIS in the polar regions. Proc. of the Sixth Symposium on Integrated Observing Systems. Orlando, FL. American Meteorological Society, Boston, MA.

Santek, D., C. Velden, J. Key, J. Daniels, and W. Bresky, 2004. Polar winds from MODIS: Algorithm and processing improvements. Proc. of Thirteenth Conference on Satellite Meteorology and Oceanography, Norfolk, VA. American Meteorological Society, Boston, MA.

Santek, D. and A. Winguth, 2007. A satellite view of internal waves induced by the Indian Ocean tsunami. *International Journal of Remote Sensing*. In press.

Sarrazin, R. and Y. Zaitseva, 2004. MODIS polar winds assimilation impact study with CMC operational NWP system, Proc. Of the Seventh Int. Winds Workshop, Helsinki, Finland, WMO (Available online at www.eumetsat.int/).

Shapiro, M. and P. Kennedy, 1981. Research aircraft measurements of jet stream geostrophic and ageostrophic winds. *J. Atmos. Sci.*, 38, 2642-2652.

Soden, B., C. Velden, and R. Tuleya, 2001. The impact of satellite winds on experimental GFDL hurricane model forecasts. *Mon. Wea. Rev.*, 129, 835-852.

Stewart, S. R., 2004. Tropical Cyclone Report: Hurricane Ivan. Retrieved 27 April 2007 from <http://www.nhc.noaa.gov/2004ivan.shtml>.

Su, X., J. Derber, J. Jung, Y. Tahara, D. Keyser, R. Treadon, Y. Zhu, 2001. Assimilation of GOES clear sky imager WV channel at NCEP'S global aviation forecast model. Eleventh Conference on Satellite Meteorology and Oceanography, AMS, Madison, WI.

Suomi, V., R. Fox, S. S. Limaye, and W. L. Smith, 1983. McIDAS III: A modern interactive data access and analysis system. *J. Climate Appl. Meteor.*, 22, 766-778.

Turner, J. and D. E. Warren, 1989. Cloud track winds in the polar regions from sequences of AVHRR images. *Int. J. Remote Sensing*, 10, 695-703.

Velden, C., C. M. Hayden, M. S. J. Nieman, W. P. Menzel, S. Wanzong, and J. S. Goers, 1997. Upper-Tropospheric winds derived from geostationary satellite water vapor observations. *Bull. Amer. Meteor. Soc.*, 78, 173-195.

Velden, C., C.M. Hayden, W.P. Menzel, J.L. Franklin, and J. Lynch, 1992. The impact of satellite-derived winds on numerical hurricane track forecasting. *Wea. Forecasting*, 7, 107-118.

Velden, C., T. Olander, and S. Wanzong, 1998. The impact of multispectral GOES-8 wind information on Atlantic tropical cyclone track forecasts in 1995. Part I: Dataset methodology, description, and case analysis. *Mon. Wea. Rev.*, 126, 1202-1218.

Velden, C., D. Stettner, J. Daniels, 2000. Wind vector fields derived from GEOS rapid-scan imagery. Tenth Conference on Satellite Meteorology, AMS, Long Beach, CA.

Velden, C., J. Daniels, D. Stettner, D. Santek, J. Key, J. Dunion, K. Holmlund, G. Dengel, W. Bresky and W.P. Menzel, 2005. Recent innovations in deriving tropospheric winds from meteorological satellites. *Bull. Amer. Meteor. Soc.*, 86, 205–223.

von Bremen, L., J-N. Thépaut, and G. Kelly, 2004. Assimilation of polar winds and recent satellite winds impact studies at ECMWF, Proc. Of the Seventh Int. Winds Workshop, Helsinki, Finland, WMO (Available online at www.eumetsat.int/).

Zapotocny, T., J. Jung, and J. LeMarshall, 2006. Recent MODIS Data Assimilation Experiments in the NCEP GFS. Fourteenth Conference on Satellite Meteorology and Oceanography, Atlanta, GA.

Zapotocny, T., J. Jung, R. Treadon, and J. LeMarshall, 2007. Recent MODIS Data Assimilation Experiments in the NCEP GFS. Eleventh Symposium on Integrated Observing and Assimilation Systems for the Atmosphere, Oceans, and Land Surface, AMS, San Antonio, TX.

Zou, C.-Z. and M. Van Woert, 2002. Atmospheric wind retrievals from satellite soundings over the middle- and high-latitude oceans. *Mon. Wea. Rev.*, 130, 1771-1791.

9. Appendix A: Parallax Correction

The following equations are used to compute the arc distance along the earth from the point directly below the cloud to the apparent position as viewed from the satellite. The known quantities are: the height of the satellite, height of the cloud, radius of the earth, and the scan angle from the satellite to the cloud. The quantity *dist* is the error in kilometers due to parallax, and is measured from the apparent position as seen from the satellite to the point beneath the cloud at the earth's surface (arc distance a_2) (Figure 48).

Using the Law of Sines, the zenith angle of the satellite from the cloud is:

$$\phi_s = \sin^{-1}\left(\frac{rhs * \sin \theta_s}{rhc}\right)$$

The angle opposite this zenith angle is the angle from cloud nadir to the satellite viewing ground position:

$$\theta_c = \phi_s$$

The Law of Sines is then used to compute the zenith angle of the cloud from the ground position:

$$\phi_c = \sin^{-1}\left(\frac{rhc * \sin \theta_c}{R}\right)$$

It follows that the remaining angles are:

$$a_1 = \pi - \phi_c$$

$$a_2 = \pi - (\theta_c + a_1)$$

And the resulting parallax shift is:

$$dist = a_2 * R$$

where

r_h : satellite distance from earth's center

r_c : cloud distance from earth's center

R : earth's radius

θ_s : sensor viewing angle from satellite nadir

θ_c : ground position viewing angle from cloud nadir

φ_s : satellite zenith angle from cloud

φ_c : cloud zenith angle from ground

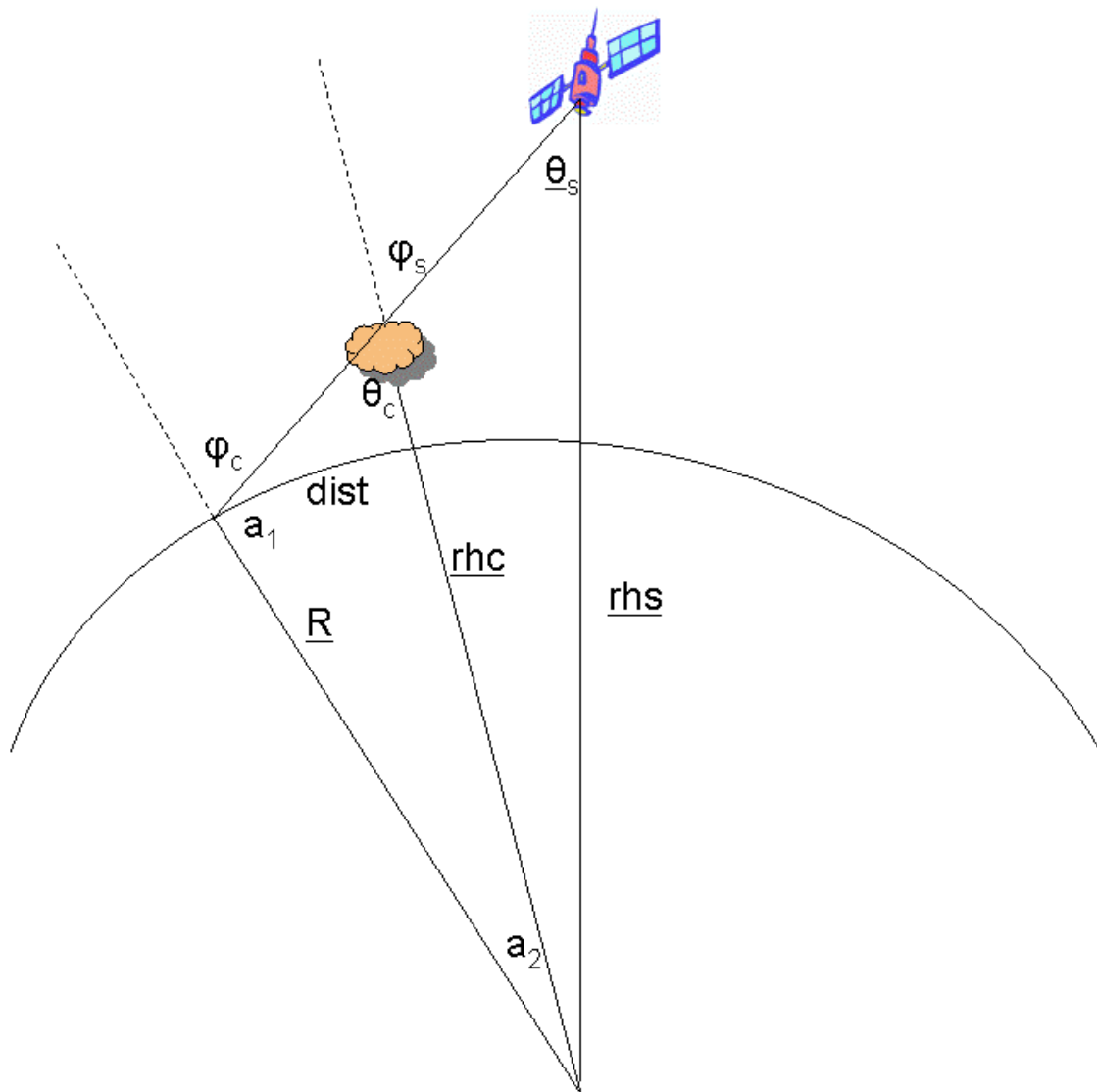
a_1 : supplementary angle of φ_c

a_2 : arc length of parallax distance

dist: error (km) of cloud ground position

The current implementation of the parallax correction algorithm assumes a spherical earth, constant altitude satellite, and a linear variation of the parallax shift with altitude for three reasons: computational efficiency for real-time processing, the inaccuracy of the target height, and the use of an Arctic standard atmosphere to convert the target height in pressure coordinates to altitude in kilometers. The standard atmosphere is used because the winds algorithm does not have the height fields on pressure surfaces as input. This may be modified in the future.

The final output of the algorithm is a parallax shift in terms of a distance and meteorological compass direction for each pixel in the original swath data for a cloud 10 km in altitude. Only one altitude is needed since the parallax shift varies near-linearly with altitude (Figure 6). These files are remapped and composited along with the swath data (see section 2.2.4 *Processing the MODIS passes*), so they can be efficiently accessed during the winds generation.



rhs : satellite distance from earth's center
 rhc : cloud distance from earth's center
 R : earth's radius
 θ_s : sensor viewing angle from satellite nadir
 θ_c : ground position viewing angle from cloud nadir
 ϕ_s : satellite zenith angle from cloud
 ϕ_c : cloud zenith angle from ground
 $dist$: error (km) of cloud ground position

Figure 48: Geometry used in parallax correction. The underlined variables are known quantities. The error due to parallax is $dist$, the arc length of angle a_2 .

The target locations that are stored in the output file are not parallax adjusted so that comparisons with uncorrected vectors can be easily performed. This uncorrected location is in error by no more than 20 km, and is usually much less than this, which is below the resolution of the global models (55 km for the GFS). The parallax correction is applied to both the location for the search boxes (which are positioned based on the forecast wind field) and the computation of the vector displacement for the image pairs.

A comparison between parallax corrected and uncorrected winds was conducted over a period of twenty-one days beginning on 23 July 2004 using data from Terra over the Arctic. Co-location was determined by matching vector distances within 10 km and heights within ± 25 hPa.

Table 18: Comparison between parallax corrected and uncorrected co-located vectors for a three-week period beginning on 23 July 2004. These are Terra-only over the Arctic.

	Number	Speed bias	Speed RMS	Vector RMS
IR Winds	200,000	-0.10	0.69	0.97
WV Winds	470,000	-0.15	0.97	1.36

Table 18 summarizes this comparison and as expected, the vector RMS for the WV winds is larger since the features are generally in the middle- and upper-troposphere, where the IR features can also be found in lower levels. An impact study has not been done on how this slight adjustment of about 1 m s^{-1} may impact model forecasts. Note that a 1 m s^{-1} difference in the wind speed corresponds to a 3 pixel difference in the images (2 km pixels with a 100-minute time step).

The speed bias is very close to zero over the 21 days, although it is slightly negative indicating that the parallax corrected speeds are slightly slower. This is reasonable because,

in many cases, correcting for parallax brings the location of the feature closer to nadir in the 2 images at an acute angle, thereby shortening the distance (and reducing the speed).

10. Appendix B: Polar Winds Impact Reported at IWW

The following are quotes from speakers and excerpts from their presentations at the 7th IWW in Helsinki, Finland in June 2004. These are in reference to the MODIS polar winds impact on global numerical model forecasts.

Joint Center for Satellite Data Assimilation (JCSDA): “Overall positive impact” “...the addition of the MODIS polar winds have a significant impact in improving the anomaly correlation, especially in many forecasts busts.” (LeMarshall et al. 2004)

ECMWF: “AMVs are a valuable part in ECMWF’s assimilation system (strong forecasts impact over Tropics and Southern Hemisphere)” (von Bremen et al. 2004)

Canadian Meteorological Centre (CMC): “The impact of all satellite winds...provides, on average, a clear positive impact on the quality of forecasts” (Sarrazin and Zaitseva 2004)

GMAO: “Positive overall contribution to forecast skill” (Riishojgaard and Zhu 2004)

Japan Meteorological Agency (JMA): “Large positive impacts on forecasts...” in the Northern Hemisphere (Kazumori and Nakamura 2004)

UK Met Office: “Neutral to positive impact in all latitude bands” (Forsythe and Berger 2004)

DWD: “Positive impact on forecast quality” (Cress 2004)

11. Appendix C: Derive Ageostrophic Wind Relation to Vorticity Advection

This derivation begins with the definition of the ageostrophic wind and shows how the divergence of the ageostrophic wind is related to relative vorticity advection.

The ageostrophic wind equation (Holton 1992) is composed of two terms:

$$\vec{V}_a = \frac{1}{f_0} \hat{k} \times \frac{D_g \vec{V}_g}{Dt} = \frac{1}{f_0} \left[\hat{k} \times \frac{\partial \vec{V}_g}{\partial t} + \hat{k} \times (\vec{V}_g \cdot \nabla) \vec{V}_g \right]$$

The first term is the isallobaric wind; the second term is the inertial advective wind. In the mid-troposphere the isallobaric wind is much smaller than the advective term (because of the higher wind speeds aloft) by about an order of magnitude, so it will be ignored in the derivation. Therefore:

$$\vec{V}_a \approx \vec{V}_{adv} = \frac{1}{f_0} \left[\hat{k} \times (\vec{V}_g \cdot \nabla) \vec{V}_g \right]$$

By applying $\nabla \cdot$ to both sides of the equation, it can be shown that (Martin 2006):

$$\nabla \cdot \vec{V}_a = -\frac{1}{f_0} \vec{V}_g \cdot \nabla \zeta_g$$

which states that the divergence of the advective component of the ageostrophic wind is related to the geostrophic wind advection of the geostrophic relative vorticity.

The derivation is as follows:

$$\vec{V}_a = \frac{1}{f_0} \left[\hat{k} \times (\vec{V}_g \cdot \nabla) \vec{V}_g \right]$$

Taking $\nabla \cdot$ on both sides of the equation:

$$\nabla \cdot \vec{V}_a = \frac{1}{f_0} \nabla \cdot \left[\hat{k} \times (\vec{V}_g \cdot \nabla) \vec{V}_g \right]$$

Expanding the inner term on the far right:

$$\begin{aligned}\nabla \cdot \vec{V}_a &= \frac{1}{f_0} \nabla \cdot \left[\hat{k} \times \left(u_g \frac{\partial \vec{V}_g}{\partial x} + v_g \frac{\partial \vec{V}_g}{\partial y} \right) \right] \\ \nabla \cdot \vec{V}_a &= \frac{1}{f_0} \nabla \cdot \left\{ \hat{k} \times \left[u_g \left(\frac{\partial u_g}{\partial x} \hat{i} + \frac{\partial v_g}{\partial x} \hat{j} \right) + v_g \left(\frac{\partial u_g}{\partial y} \hat{i} + \frac{\partial v_g}{\partial y} \hat{j} \right) \right] \right\} \\ \nabla \cdot \vec{V}_a &= \frac{1}{f_0} \nabla \cdot \left\{ \hat{k} \times \left[u_g \frac{\partial u_g}{\partial x} \hat{i} + u_g \frac{\partial v_g}{\partial x} \hat{j} + v_g \frac{\partial u_g}{\partial y} \hat{i} + v_g \frac{\partial v_g}{\partial y} \hat{j} \right] \right\}\end{aligned}$$

Rearrange and group by vector direction:

$$\nabla \cdot \vec{V}_a = \frac{1}{f_0} \nabla \cdot \left\{ \hat{k} \times \left[\left(u_g \frac{\partial u_g}{\partial x} + v_g \frac{\partial u_g}{\partial y} \right) \hat{i} + \left(u_g \frac{\partial v_g}{\partial x} + v_g \frac{\partial v_g}{\partial y} \right) \hat{j} \right] \right\}$$

Perform $\hat{k} \times$:

$$\nabla \cdot \vec{V}_a = \frac{1}{f_0} \nabla \cdot \left[- \left(u_g \frac{\partial v_g}{\partial x} + v_g \frac{\partial v_g}{\partial y} \right) \hat{i} + \left(u_g \frac{\partial u_g}{\partial x} + v_g \frac{\partial u_g}{\partial y} \right) \hat{j} \right]$$

Perform $\nabla \cdot$:

$$\nabla \cdot \vec{V}_a = \frac{1}{f_0} \left[- \frac{\partial}{\partial x} \left(u_g \frac{\partial v_g}{\partial x} + v_g \frac{\partial v_g}{\partial y} \right) + \frac{\partial}{\partial y} \left(u_g \frac{\partial u_g}{\partial x} + v_g \frac{\partial u_g}{\partial y} \right) \right]$$

Expand using the product rule:

$$\nabla \cdot \vec{V}_a = \frac{1}{f_0} \left[- \frac{\partial u_g}{\partial x} \frac{\partial v_g}{\partial x} - u_g \frac{\partial^2 v_g}{\partial x^2} - \frac{\partial v_g}{\partial x} \frac{\partial v_g}{\partial y} - v_g \frac{\partial^2 v_g}{\partial y^2} + \frac{\partial u_g}{\partial x} \frac{\partial u_g}{\partial y} + u_g \frac{\partial^2 u_g}{\partial x^2} + \frac{\partial v_g}{\partial y} \frac{\partial u_g}{\partial y} + v_g \frac{\partial^2 u_g}{\partial y^2} \right]$$

Negate and rearrange:

$$\nabla \cdot \vec{V}_a = - \frac{1}{f_0} \left[\frac{\partial u_g}{\partial x} \frac{\partial v_g}{\partial x} + u_g \frac{\partial^2 v_g}{\partial x^2} - \frac{\partial u_g}{\partial x} \frac{\partial u_g}{\partial y} - u_g \frac{\partial^2 u_g}{\partial x^2} + \frac{\partial v_g}{\partial x} \frac{\partial v_g}{\partial y} + v_g \frac{\partial^2 v_g}{\partial y^2} - \frac{\partial v_g}{\partial y} \frac{\partial u_g}{\partial y} - v_g \frac{\partial^2 u_g}{\partial y^2} \right]$$

Factor, by reverse product rule, each group of four terms within the brackets:

$$\nabla \cdot \vec{V}_a = -\frac{1}{f_0} \left[\frac{\partial}{\partial x} \left(u_g \frac{\partial v_g}{\partial x} - u_g \frac{\partial u_g}{\partial y} \right) + \frac{\partial}{\partial y} \left(v_g \frac{\partial v_g}{\partial x} - v_g \frac{\partial u_g}{\partial y} \right) \right]$$

Put in vector notation and factor out wind components in each term:

$$\nabla \cdot \vec{V}_a = -\frac{1}{f_0} \nabla \cdot \left[u_g \left(\frac{\partial v_g}{\partial x} - \frac{\partial u_g}{\partial y} \right) \hat{i} + v_g \left(\frac{\partial v_g}{\partial x} - \frac{\partial u_g}{\partial y} \right) \hat{j} \right]$$

Recognize that term with parentheses is horizontal vorticity, and factor:

$$\nabla \cdot \vec{V}_a = -\frac{1}{f_0} \nabla \cdot \zeta_g (u_g \hat{i} + v_g \hat{j})$$

Replace far right term with vector notation:

$$\nabla \cdot \vec{V}_a = -\frac{1}{f_0} \nabla \cdot \zeta_g \vec{V}_g$$

Using the vector identity for the divergence of a vector (A) multiplied by a scalar (s):

$$\nabla \cdot (s\vec{A}) = s\nabla \cdot \vec{A} + \vec{A} \cdot \nabla s$$

and the fact that the geostrophic wind is non-divergent (the first term on right-hand side is zero), the final equation can be rewritten as:

$$\nabla \cdot \vec{V}_a = -\frac{1}{f_0} \vec{V}_g \cdot \nabla \zeta_g$$

The divergence of the advective component of the ageostrophic wind is related to the geostrophic wind advection of the geostrophic relative vorticity.

12. Appendix D: Impact of MODIS winds in the NOGAPS

As part of the determination on how the MODIS winds impact the analysis and subsequent forecasts, the output from a second model, NOGAPS, is chosen to compare and contrast what is observed in the GFS output. The NOGAPS is run at resolution T239 with 30 levels (compared to T254 and 64 levels for the GFS) The criteria used to assimilate the MODIS winds are (Pauley and Pauley 2004):

1. Winds are superobbed in 2° prisms. Prisms are nearly square regions of 2° latitude by 2° longitude at the equator. The width is adjusted to keep the area nearly constant for regions away from the equator.
2. Superobbing of winds is subject to these constraints:
 - a. There are at least two consistent observations in the prism
 - b. One or two outliers may be rejected
 - c. Wind speeds are within 7 m s⁻¹
 - d. U and V components are within 5 m s⁻¹ or directions within 20°
3. The observation error is the same as the geostationary AMVs.

Two days were analyzed from the NOGAPS model forecast runs with and without assimilating the MODIS winds: 17 August 2005 (Figure 49 and Figure 50) and 19 August 2005 (Figure 51 and Figure 52). This is a different year than the GFS experiment, but it is a similar season. The goal is not to directly compare the NOGAPS output with the GFS, but rather to determine if the difference signatures from the addition of the MODIS winds are similar. The thickness difference features in the NOGAPS analyses and forecasts are similar to what is observed in Figure 22 and Figure 24: the largest impact is within and poleward of

the jet streams, especially in later forecasts. But, there are some differences in the patterns of the difference features:

1. The NOGAPS thickness difference features are smoother; without the small-scale details as seen in the GFS, even though the spatial resolution is approximately the same. The GDAS (GFS) assimilates the MODIS winds as individual observations while the NAVDAS (NOGAPS) creates 'super observations', by combining many winds into a single observation. This 'superobbing' may smooth out smaller scale details.
2. The difference features over the polar regions in the NOGAPS analyses are larger than in the GFS. This may be due to the NAVDAS assigning a medium weight to the MODIS winds, while the GDAS uses a low weight.
3. The difference features in the jet stream region of the NOGAPS analyses are much less than in the GFS. Unlike the NAVDAS, the GDAS uses a global dynamic bias correction and a spectral interpolation technique which tends to propagate the influence of observations well-away for the observation location. The impact, in terms of the magnitude and distribution of difference features, into the tropics is less in the NOGAPS than in the GFS. The differences in the assimilation systems may explain the larger differences in tropics in the GFS runs.

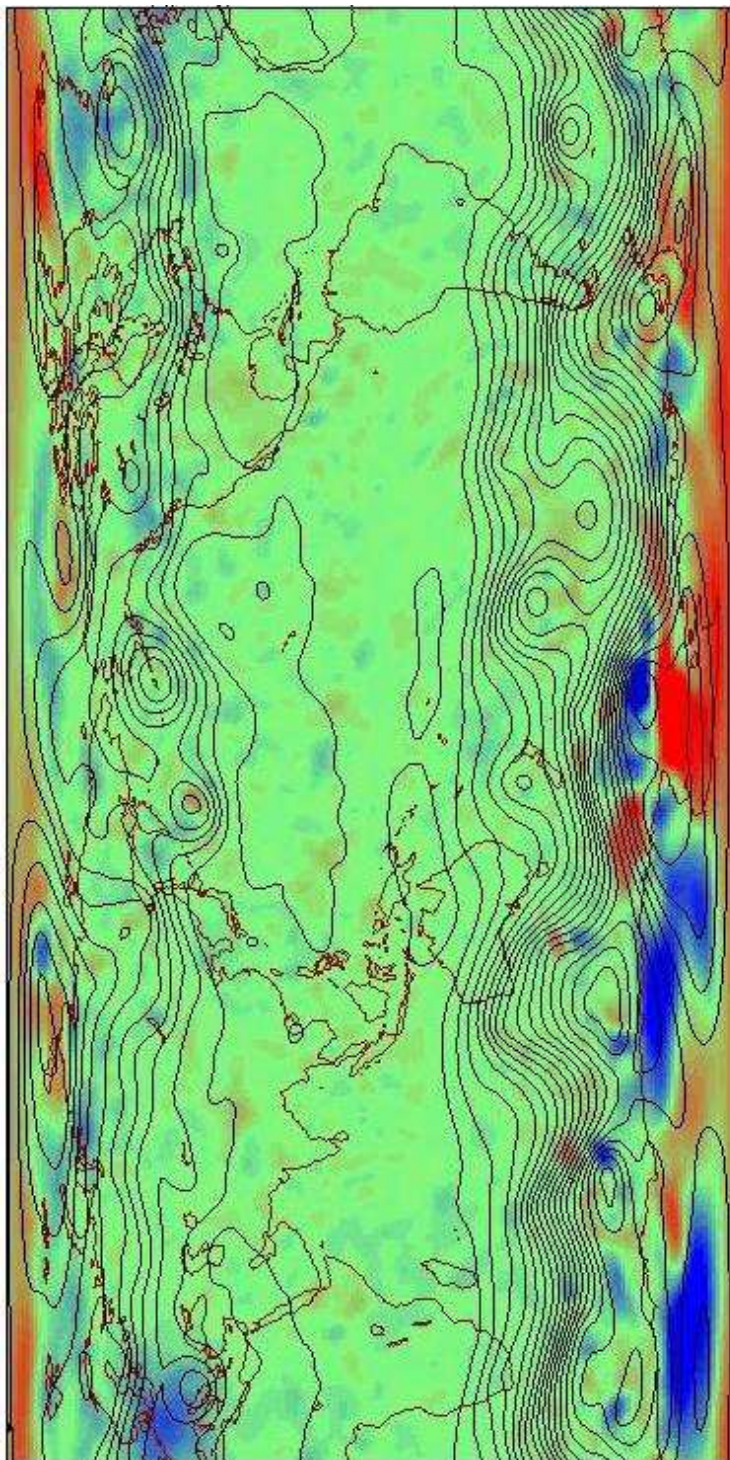


Figure 49: NOGAPS analysis from 17 August 2005 1200 GMT. Same color scheme as Figure 22, although the jet streams are not depicted.

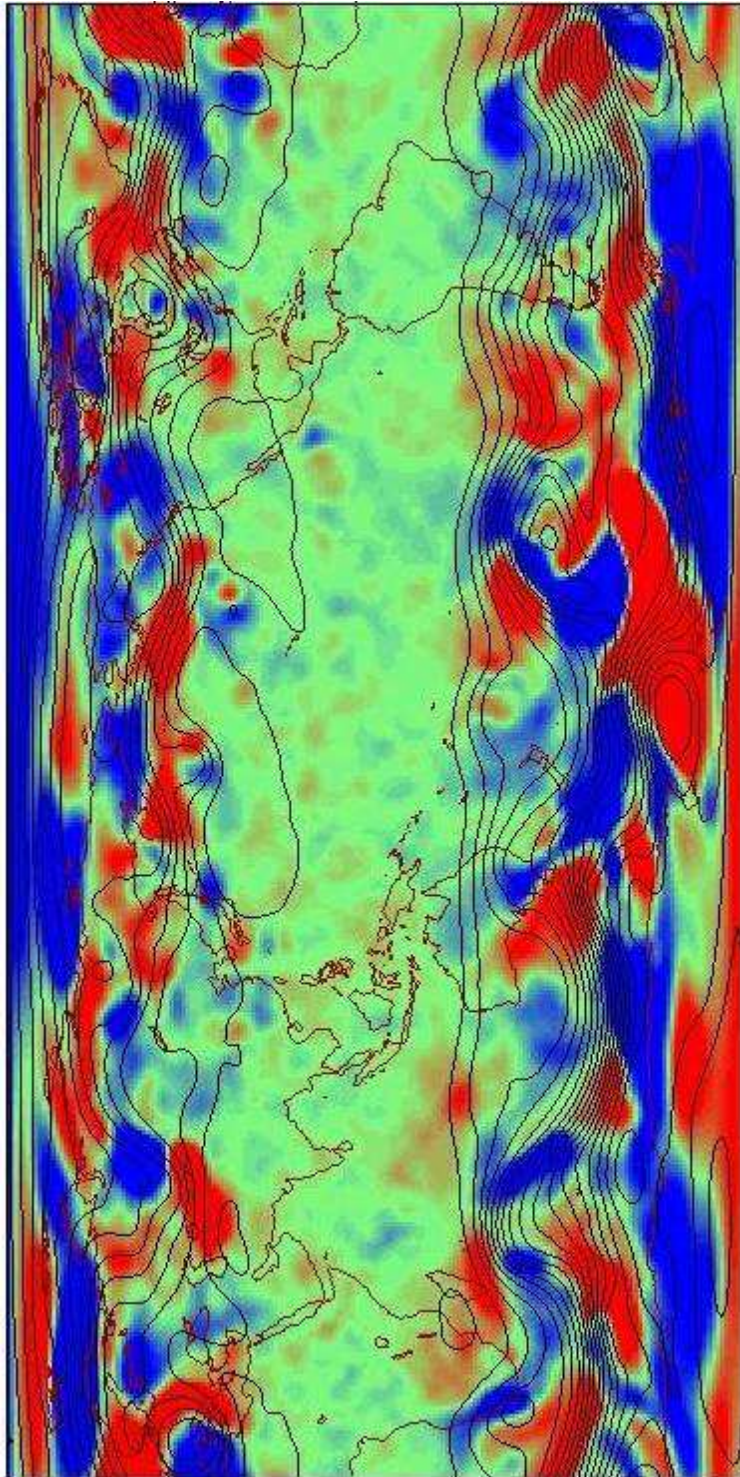


Figure 50: NOGAPS 120-hour forecast from 17 August 2005 1200 GMT. Same color scheme as Figure 22, although the jet streams are not depicted.

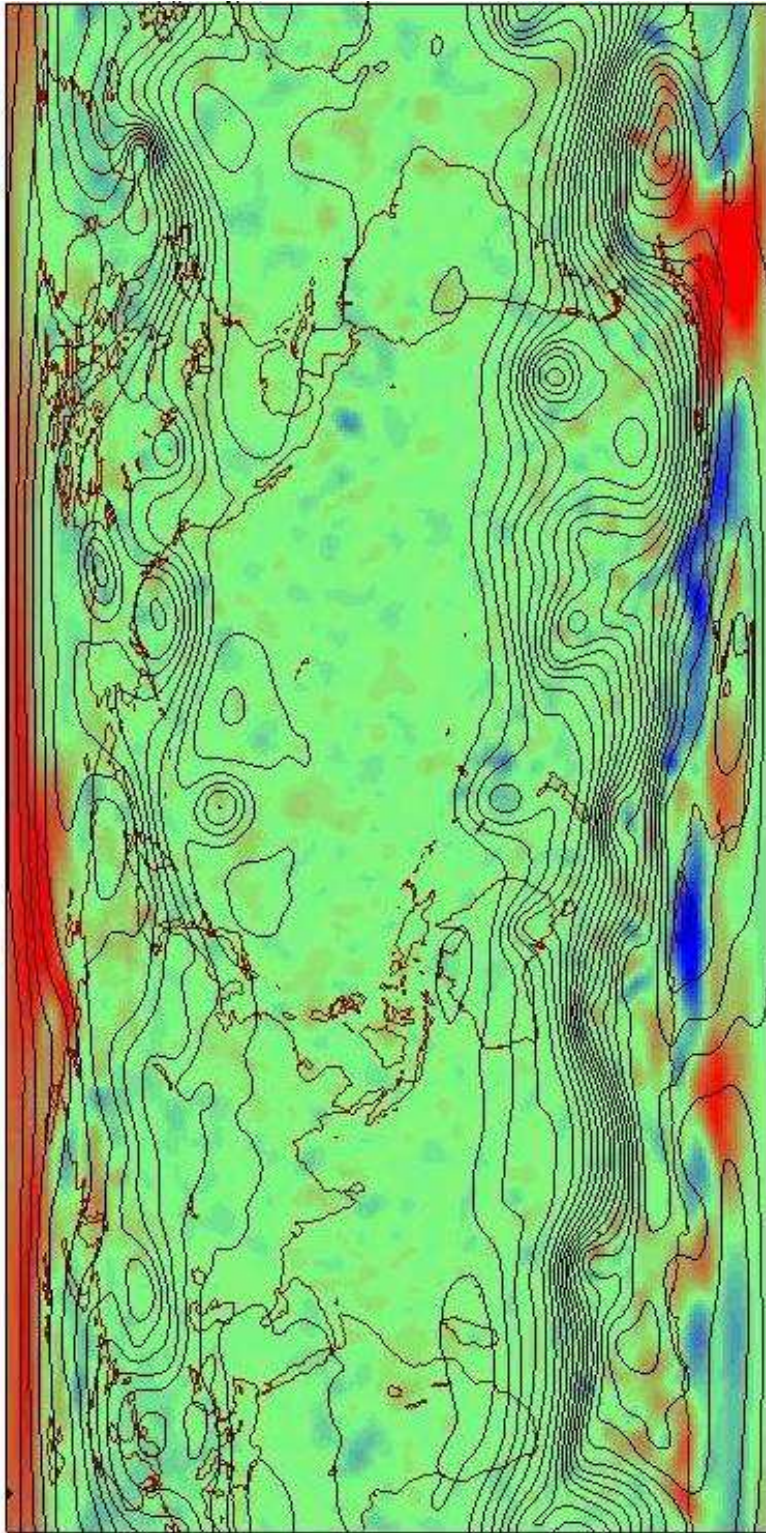


Figure 51: NOGAPS analysis from 19 August 2005 1200 GMT. Same color scheme as Figure 22, although the jet streams are not depicted.

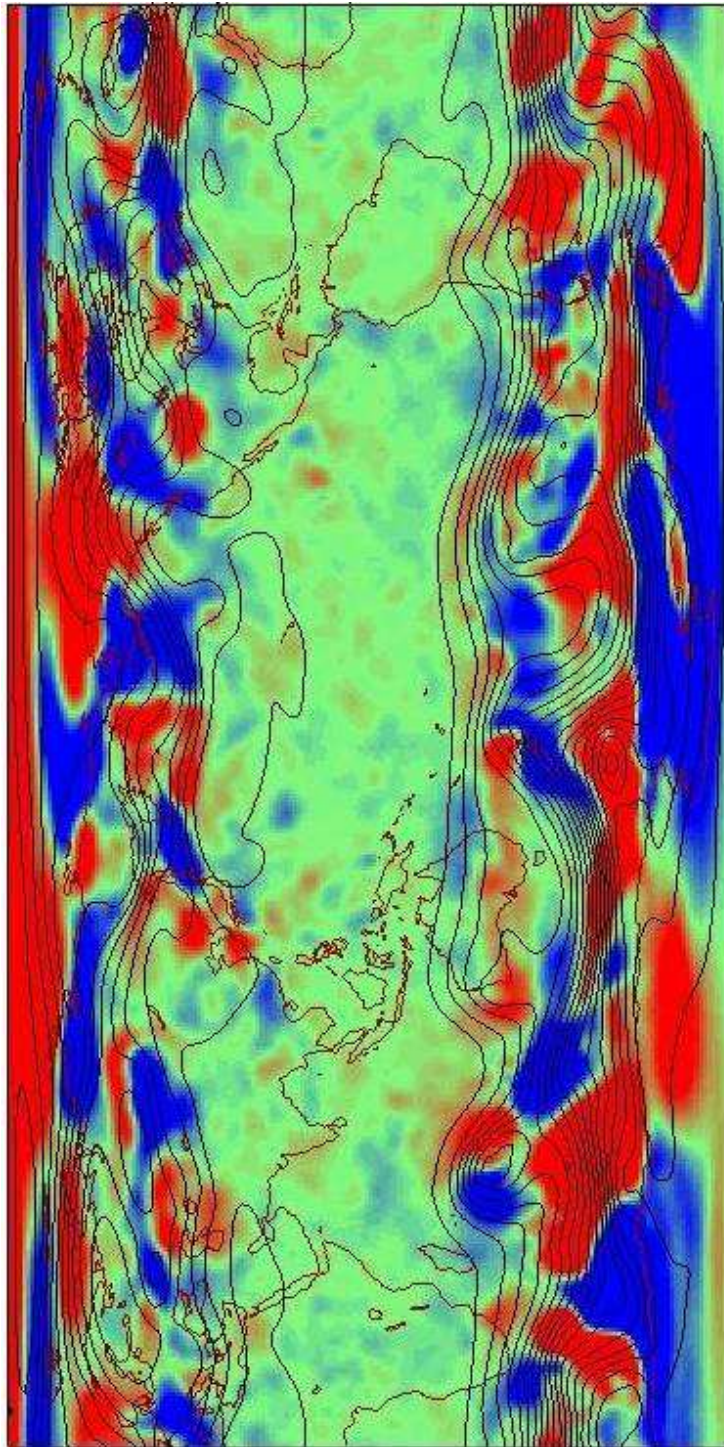


Figure 52: NOGAPS 120-hour forecast from 19 August 2005 1200 GMT. Same color scheme as Figure 22, although the jet streams are not depicted.

13. Appendix E: Impact of AMSU Radiances in the GFS

The affect of AMSU radiance assimilation is investigated to make a qualitative assessment of the impact the MODIS winds have on the analysis compared to another satellite-based data source. This assessment is based on the visualization of the thickness difference, as was done for the NOGAPS experiment (*Appendix D: Impact of MODIS winds in the NOGAPS*).

Important characteristics of the AMSU radiance experiment include:

1. This dataset is from yet another year, but the same season: August 2003.
2. The AMSU data are global measurements from the NOAA Polar Orbiting Environmental Satellites (POES), which provide complete global coverage twice daily from each satellite. Unlike the MODIS winds which provide data only over the poles.
3. Only the analyses are used; forecast output was not available.
4. This is a 'denial' experiment, unlike the MODIS winds which were added. After about a week both models will have adjusted, so this difference is not a factor for interpreting the impact of the data.
5. An error occurred during the experiment: the AMSU radiances were inadvertently added back to the model run where they were denied. This provided an opportunity to observe how quickly the two model runs become similar.

Changes in the 1000-500 hPa thickness fields provide a way to compare the assimilation of winds and radiances:

- The winds affect the geopotential height field through the mass balance in the model.
- The radiances modify the temperature structure which impacts the geopotential thickness field (Eq. 14), to maintain a thermal balance (Eq. 15).

Two weeks of analyses from this experiment showed a consistent impact from the AMSU radiances. Two representative cases a week apart, Figure 53 and Figure 54, depict thickness differences between the two model runs: the control (which include AMSU radiances) and one where AMSU radiances are denied. These differences are larger than what was observed in the analyses from the MODIS winds in both the GFS (Figure 22) and NOGAPS (Figure 50) models. This is expected as the AMSU radiances are weighted higher than satellite winds in the GDAS and they have been found to have the largest impact in the GDAS of any satellite-based data (Zapotocny et al. 2007). Also, since the AMSU radiances are a global dataset, there are thickness differences at all latitudes, much more so than from the MODIS winds.

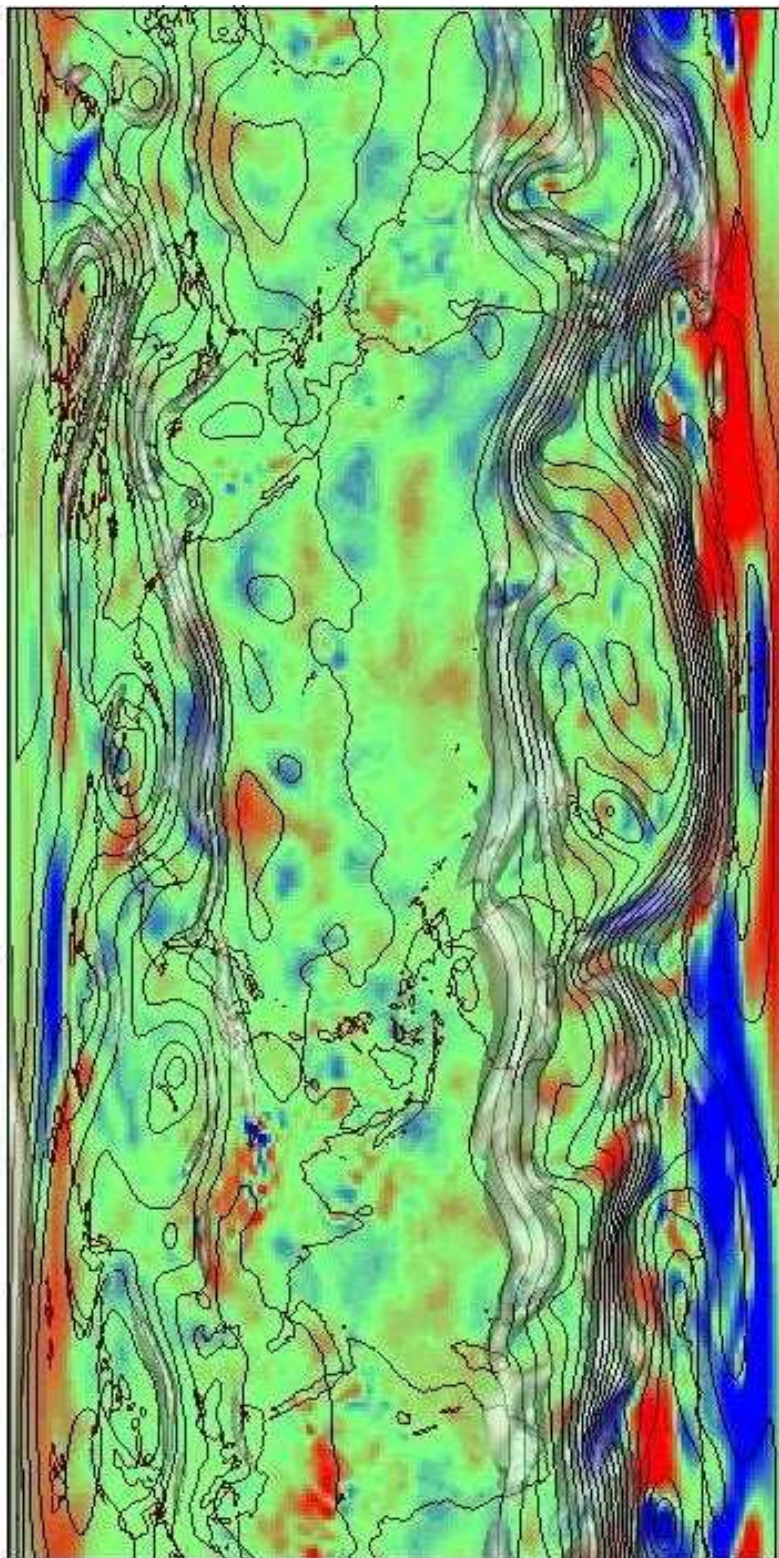


Figure 53: 17 Aug 2003 at 0000 GMT analysis from GFS, AMSU assimilated. Same color scheme as Figure 22.

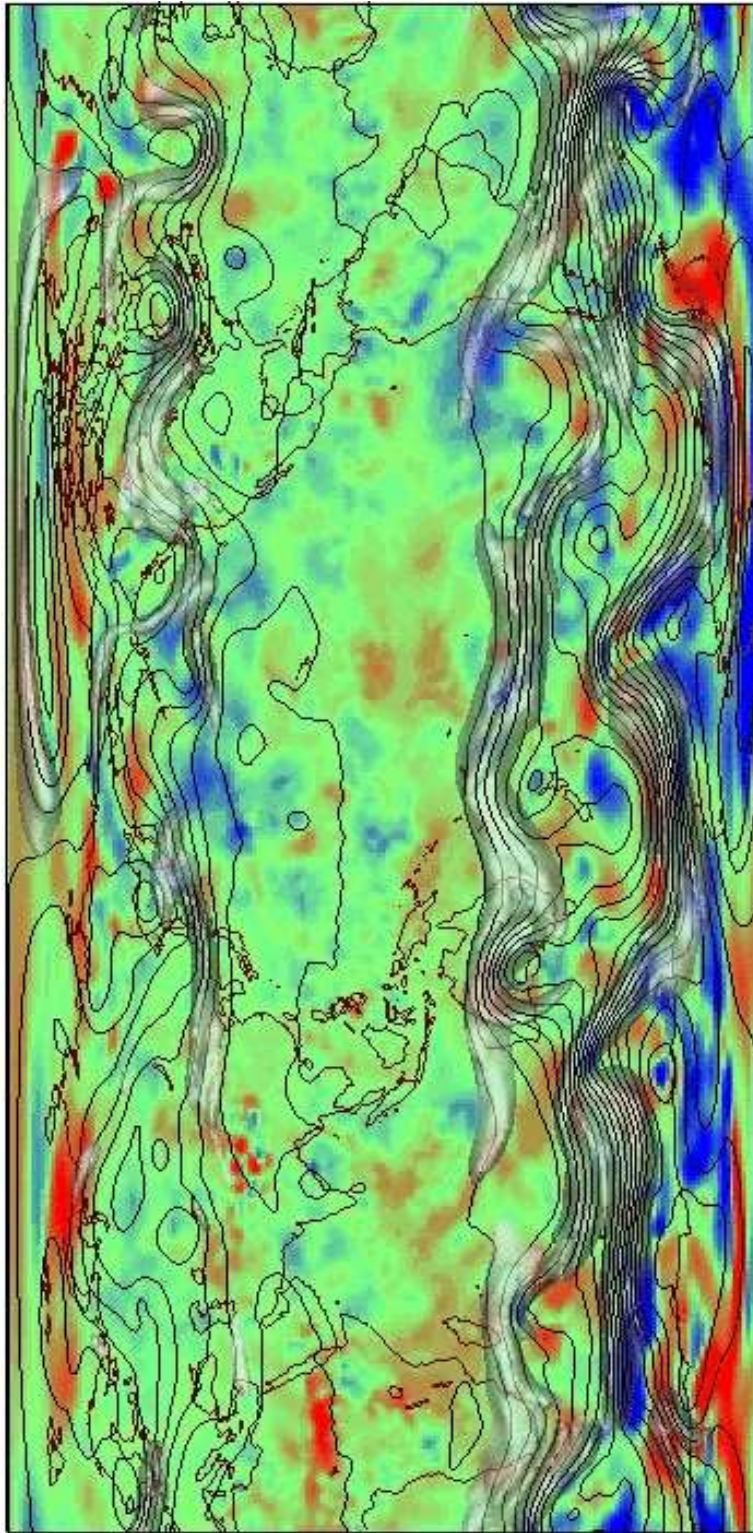


Figure 54: 23 Aug 2003 at 0000 GMT analysis from GFS, AMSU assimilated. Same color scheme as Figure 22.